

HYBRID MODELLING OF ELASTIC WAVE INTERACTION
WITH INHOMOGENEITIES IN AN ELASTIC MEDIUM

BY

RATNAM PASKARAMOORTHY

A Thesis
Submitted to the Faculty of Graduate Studies
in Partial Fulfillment of the Requirements
for the Degree of

DOCTOR OF PHILOSOPHY

Department of Civil Engineering
University of Manitoba
Winnipeg, Manitoba

© August, 1990



National Library
of Canada

Bibliothèque nationale
du Canada

Canadian Theses Service

Service des thèses canadiennes

Ottawa, Canada
K1A 0N4

The author has granted an irrevocable non-exclusive licence allowing the National Library of Canada to reproduce, loan, distribute or sell copies of his/her thesis by any means and in any form or format, making this thesis available to interested persons.

The author retains ownership of the copyright in his/her thesis. Neither the thesis nor substantial extracts from it may be printed or otherwise reproduced without his/her permission.

L'auteur a accordé une licence irrévocable et non exclusive permettant à la Bibliothèque nationale du Canada de reproduire, prêter, distribuer ou vendre des copies de sa thèse de quelque manière et sous quelque forme que ce soit pour mettre des exemplaires de cette thèse à la disposition des personnes intéressées.

L'auteur conserve la propriété du droit d'auteur qui protège sa thèse. Ni la thèse ni des extraits substantiels de celle-ci ne doivent être imprimés ou autrement reproduits sans son autorisation.

ISBN 0-315-63241-0

Canada

HYBRID MODELLING OF ELASTIC WAVE INTERACTION WITH
INHOMOGENEITIES IN AN ELASTIC MEDIUM

BY

RATNAM PASKARAMOORTHY

A thesis submitted to the Faculty of Graduate Studies of
the University of Manitoba in partial fulfillment of the requirements
of the degree of

DOCTOR OF PHILOSOPHY

© 1990

Permission has been granted to the LIBRARY OF THE UNIVERSITY OF MANITOBA to lend or sell copies of this thesis, to the NATIONAL LIBRARY OF CANADA to microfilm this thesis and to lend or sell copies of the film, and UNIVERSITY MICROFILMS to publish an abstract of this thesis.

The author reserves other publication rights, and neither the thesis nor extensive extracts from it may be printed or otherwise reproduced without the author's written permission.

Hybrid Modelling of Elastic Wave Interaction With Inhomogeneities In An Elastic Medium

Abstract

Two hybrid modelling schemes are presented to study the interaction of steady state elastic waves with inhomogeneities embedded in an infinite/semi-infinite elastic medium. The modelling is achieved by partitioning the domain into an interior region and an exterior region. The interior region is bounded and contains all inhomogeneities. It is modelled by conventional finite elements. Wave function expansions are used in the first scheme while a boundary integral representation is employed in the second one, to model the exterior region.

The first scheme is used to investigate the scattering of elastic waves by spheroidal inclusions embedded in an infinite medium. The results may be used to ultrasonically characterize different inclusion shapes. Also studied by using this scheme is the interaction of flexural waves with a cavity/crack in an infinite plate. It is found that the stress concentration factors are lower in the dynamic case than in the static case.

The second scheme is intended for *half-space* problems. The emphasis here is on field representation and on evaluation of the model. The results obtained from this model are found to be in excellent agreement with those obtained by other schemes. Finally the application of the model to study the scattering of seismic waves by canyons on the surface of a half-space is demonstrated.

ACKNOWLEDGEMENTS

The author deeply appreciates the supervision of his advisor, Prof. Arvind Shah throughout the course of this research. A couple of sentences cannot adequately express the measure of gratitude which is due to him for his encouragement and support during graduate work at the University of Manitoba.

Thanks are extended to Yogesh, Udeni and Karu, author's colleagues and friends, for their help. Timely completion of the manuscript would have been impossible if not for the untiring help of Yogesh Desai and he deserves special thanks.

Financial support in the form of a research assistantship from NSERC research grant of Prof. Shah, teaching assistantships from the Departments of Civil and Mechanical Engineering and a graduate fellowship from the University of Manitoba enabled the author to pursue his graduate studies. They are kindly acknowledged.

The author wishes to thank his parents, wife and children for their understanding and support. In particular, his son, Arun, missed his playtimes to 'let daddy do his work'.

The thesis is dedicated with great respect to Uncle Chelliah, author's mentor from a young age.

TABLE OF CONTENTS

ABSTRACT	i
ACKNOWLEDGEMENTS	ii
LIST OF TABLES	vi
LIST OF FIGURES	vii
1. INTRODUCTION	1
1.1 General	1
1.2 Methods available : An overview	2
1.3 Literature review	4
1.3.1 Scattering by three dimensional inhomogeneities in an infinite medium ..	4
1.3.2 Scattering of flexural waves by a cavity/crack in an infinite plate	5
1.3.3 Scattering of seismic waves by axisymmetric canyons on the surface of an elastic half space	6
1.4 Organization of the thesis	8
2. HYBRID MODELLING WITH WAVE FUNCTIONS FOR FULL SPACE	
PROBLEMS	9
2.1 Description of the problem	9
2.2 Hybrid model : Finite element – Wave function expansion	10
2.3 Finite element formulation of the interior region	10
2.4 Spherical wave functions for exterior region	14
2.5 Global solution	17
2.6 Incident wave	18
2.7 Numerical results and discussions	21
2.8 Concluding remarks	23
Appendix A : Wave functions for full space	25
Appendix B : Scattering cross sections for full space	26

Appendix C : Material properties	27
Tables	28
Figures	33
3. HYBRID MODELLING WITH WAVE FUNCTIONS FOR PLATE PROBLEMS	41
3.1 Introduction	41
3.2 Mindlin's theory	41
3.3 Hybrid model : Finite element – Wave function expansion	43
3.4 Finite element formulation of the interior region	44
3.5 Flexural wave functions for exterior region	46
3.6 Global solution	48
3.7 Stress intensity factors	49
3.8 Numerical results and discussions	51
3.8.1 Validation of the model	51
3.8.2 Scattering by arbitrary shaped cavities	53
3.8.3 Performance of plate bending elements	54
3.8.4 Scattering by a crack	58
3.9 Concluding remarks	60
Appendix D : Flexural wave functions for plate	62
Figures	64
4. HYBRID MODELLING WITH BOUNDARY INTEGRAL EQUATIONS FOR HALF SPACE PROBLEMS	89
4.1 Description of the problem	89
4.2 Hybrid model : Finite element – Boundary integral equation technique	90
4.3 Finite element formulation of the region R_I	91
4.4 Boundary integral representation of the region R_E	92
4.5 Green's function for axisymmetric analysis	96
4.5.1 Green's function for full space	96

4.5.2 Green's function for half space	101
4.6 Evaluation of Green's function	104
4.7 Validation of the model	106
4.8 Scattering by a canyon in a half space	107
4.9 Concluding remarks	108
Appendix E : Green's functions for axisymmetric analysis	110
Table	113
Figures	114
5. SUMMARY AND CONCLUSIONS	126
REFERENCES	127

LIST OF TABLES

Table 2.1 : Comparison of analytical and numerical results for real and imaginary parts of $4\pi/k_p^2 A_p(0)$ and $4\pi/k_s^2 A_s(0)$ for scattering by spherical SiC particles in Al matrix	28
Table 2.2 : Comparison of analytical and numerical results for $4\pi/k_p^2 A_p(0)$ and $4\pi/k_s^2 A_s(0)$ for scattering by a SiC particle with one interface layer in Al matrix	29
Table 2.3 : Comparison of analytical and numerical results for $4\pi/k_p^2 A_p(0)$ and $4\pi/k_s^2 A_s(0)$ for scattering by a SiC particle with two interface layers in Al matrix	30
Table 2.4 : Comparison of analytical and numerical results for $4\pi/k_p^2 A_p(0)$ and $4\pi/k_s^2 A_s(0)$ for scattering by a SiC particle in Al matrix when the angle of incidence is 45° ...	31
Table 2.5 : Comparison of analytical and numerical results for $4\pi/k_p^2 A_p(0)$ and $4\pi/k_s^2 A_s(0)$ for scattering by a SiC particle in Al matrix when the angle of incidence is 90°	32
Table 4.1 : Evaluation of infinite integrals appearing in equation (4.44) ...	113

LIST OF FIGURES

Figure 2.1 : Geometry of the problem	33
Figure 2.2 : Coordinate systems	34
Figure 2.3 : Displacement on the surface of the cavity	35
Figure 2.4 : Displacement on the surface of the cavity	36
Figure 2.5 : Geometry of the spherical scatterer	37
Figure 2.6 : Geometry of the spheroidal scatterer	38
Figure 2.7 : Scattering cross section of spheroidal inclusion for incident P waves	39
Figure 2.8 : Scattering cross section of spheroidal inclusion for incident SV waves	40
Figure 3.1 : Geometry of the problem	64
Figure 3.2 : Plan view showing mesh boundary B	64
Figure 3.3 : A typical finite element model (inhomogeneity is a circular cavity)	65
Figure 3.4 : Geometry of the crack and the hybrid model	66
Figure 3.5 : Finite element grid for crack in the plate	67
Figure 3.6 : Crack – tip element	68
Figure 3.7 : Displacement along the circumference of the circular cavity ($\bar{w} = 0.9$, $\bar{a} = 0.5$, $\gamma = 0^\circ$)	69
Figure 3.8 : Variation of tangential moment ($\bar{w} = 0.9$, $\bar{a} = 0.5$, $\gamma = 0^\circ$) ...	70

Figure 3.9 : Effect of \bar{a} on the tangential moment around cavities $(\bar{w} = 2.0, \gamma = 0^\circ)$	72
Figure 3.10 : Effect of frequencies on the tangential moment around the ($\bar{a} = 2.0, \gamma = 0^\circ$)	74
Figure 3.11 : Effect of incidence angles on the tangential moment around the cavities ($\bar{w} = 0.5, \bar{a} = 2.0$)	76
Figure 3.12 : Displacement at the circumference of the cavity for $\bar{a} = 2, \bar{w} = 0.5$	77
Figure 3.13 : Displacement at the circumference of the cavity for $\bar{a} = 10, \bar{w} = 0.5$	78
Figure 3.14 : Displacement at the circumference of the cavity for $\bar{a} = 40, \bar{w} = 0.5$ (analytical)	79
Figure 3.15 : Displacement at the circumference of the cavity for $\bar{a} = 40, \bar{w} = 0.1$	80
Figure 3.16 : Effect of mass schemes on the displacement for $\bar{a} = 2, \bar{w} = 0.5$ (heterosis element)	81
Figure 3.17 : Effect of mass schemes on the displacement for $\bar{a} = 10, \bar{w} = 0.5$ (heterosis element)	82
Figure 3.18 : Effect of mass schemes on the displacement for $\bar{a} = 40, \bar{w} = 0.1$ (DKT element)	83
Figure 3.19 : Comparison of stress intensity factor \bar{K}_1	84
Figure 3.20 : Effect of \bar{a} on stress intensity factor \bar{K}_1	85
Figure 3.21 : Effect of \bar{a} on stress intensity factor \bar{K}_2	86
Figure 3.22 : Effect of angle of incidence on stress intensity factor \bar{K}_1 ...	87
Figure 3.23 : Effect of angle of incidence on stress intensity factor \bar{K}_2 ...	88

Figure 4.1 :	Description of the problem	114
Figure 4.2 :	Hybrid model	115
Figure 4.3 :	Finite element mesh between contours C and B	116
Figure 4.4 :	System used in the derivation of full space Green functions ...	117
Figure 4.5 :	Integration paths	118
Figure 4.6 :	Concentrated ring forces of unit magnitude	119
Figure 4.7 :	Finite element mesh of Region R_I for a cavity in an entire space	120
Figure 4.8 :	Displacements on the surface of a spherical cavity $(\bar{\omega} = 0.25, N_B = 35)$	121
Figure 4.9 :	Displacements on the surface of a spherical cavity $(\bar{\omega} = 0.75, N_B = 49)$	122
Figure 4.10 :	Displacements on the surface of a spherical cavity $(\bar{\omega} = 1.50, N_B = 49)$	123
Figure 4.11 :	Displacements on the surface of a hemispherical canyon $(\bar{\omega} = 0.25)$	124
Figure 4.12 :	Displacements on the surface of a hemispherical canyon $(\bar{\omega} = 0.50)$	125

1. INTRODUCTION

1.1 General

The catastrophic nature of earthquakes is well known. It is estimated that as many as 50,000 people perished in the December, 1988 earthquake in Armenia, USSR (ASCE, 1990). The recent Loma Prieta earthquake of October 17, 1989 measured 7.1 on the Richter scale. It had a mere five seconds of strong ground motion but caused over U\$ 5 billion in damage (ENR, 1990). Most of the property damage and loss of life occurred on soft soils comprising less than 1% of the total ground area affected, and many miles from the epicenter. This indicates that there is a need to understand how seismic waves interact with obstacles and how the local topography and geological characteristics influence the ground motion during earthquakes. The subject has been treated in the literature as a problem of elastic wave scattering. In this thesis, *scattering* means a combined effect of reflection, refraction and diffraction.

Elastic wave scattering is the result of interaction of elastic waves with obstacles or inhomogeneities embedded in an elastic medium. It has been a subject of interest to many researchers not only in earthquake engineering but also in nondestructive testing.

In the field of nondestructive testing, the interest is in detecting defects in solids. In this, an ultrasonic (elastic) pulse is sent into the solid containing the defect. When the pulse passes through a defect such as a flaw, a crack or an inhomogeneity, it is scattered. The scattered field carries a substantial amount of information about the size, shape, location and nature of the defect. Detection of existence and nature of the defect from the measured scattered field constitutes an *inverse* problem. A solution of the direct problem is, however, a necessary prerequisite for solving the inverse problem.

This study is concerned with the numerical modelling of steady state scattering of elastic waves by inhomogeneities embedded in an isotropic elastic medium. In particular, the investigation first considers the scattering of elastic waves by a spheroidal inclusion. The results may be used to ultrasonically characterize different inclusion shapes. Secondly the interaction of flexural elastic waves with a cavity/crack in an infinite plate is considered. The effect of a dynamic loading on a plate is to generate waves. When these waves pass through a geometric discontinuity such as a cavity or a crack, they are scattered causing a sharp increase of stress over a nominal value in a localized region of the discontinuity. Knowledge of this dynamic stress concentration is useful in the design of pressure vessels, nuclear power plant components, etc. Finally, the scattering of seismic waves by canyons having axisymmetric geometry on the surface of an elastic half space is considered. The resulting ground motion amplification effects can be an important factor in the assessment of seismic risk, in urban planning and in seismic design of critical facilities. The aforementioned three problems are referred to as full-space, plate and half-space problems, respectively. The basic nature of all these seemingly different problems is the same, viz, to determine the scattered field for a given scatterer and incident field.

1.2 Methods available : An overview

The solution of a steady state elastic wave scattering problem may be approached by either analytical or numerical methods. Both approaches have certain limitations depending on the nature of the problem.

Analytical techniques dominated the literature during the first half of the century. Two analytical solution techniques have been mostly used and they met with minimal success (Pao and Mow,1973). One is separation of variables (also called *wave function expansion technique*) in which the partial differential equations describing the scattering

phenomenon are solved in terms of wave functions for fields inside and outside the inhomogeneity. The inner and outer solutions are then matched across the surface of the inhomogeneity to ensure continuity of displacements and stresses. The matching is intractable, however, for inhomogeneities having surfaces that do not correspond to level surfaces of the coordinate system being used. The other technique is the integral equation method. Although this method is conceptually valid for scatterers of arbitrary geometry, again solutions do not appear possible except for very simple geometries.

Most scatterers encountered in practice have complicated geometries. Closed form solutions for these scatterers are not feasible and, therefore, it is necessary to resort to numerical methods. The most versatile numerical tool is the finite element method. In this approach, both the scatterer and the host medium are modelled through an assemblage of finite elements. An obvious shortcoming of such an approach is that the domain, which is usually infinite in the direction of at least one coordinate axis for the class of problems under consideration, has to be modelled by a finite sized model. Attempts have been made to reduce the error stemming from the use of finite sized model by prescribing appropriate boundary conditions to be used along the boundary of the finite computational domain (Lysmer and Kuhlemeyer, 1969; Smith, 1974; Kausel et al, 1975; Chow and Smith, 1981; Medina and Taylor, 1983; Lee and Dasgupta, 1984). By and large, they are either approximate in nature or work best at certain angles of incidence. Recently a scheme has been proposed (Ting and Miksis, 1986) to generate exact boundary data but a numerical implementation and comparison of accuracy of this scheme is yet to be reported.

In recent years, boundary integral equation methods have gained increasing popularity. Unlike finite element methods, no fictitious boundaries are introduced in a boundary integral formulation. Thus these methods are well suited to deal with wave propagation problems. In these methods, an integral representation involving boundary values and possibly interior sources is constructed and solved (Cruse, 1968; Cole et al, 1978). The

solution at any interior point is then determined through the original integral representation. The infinite nature of the domain encountered in wave propagation problems does not cause any difficulty. The main advantage of the boundary integral method is that it reduces by one the dimensionality of the problem which yields numerical advantages. Furthermore, the boundary integral equation methods can be combined with finite element methods. This combination offers a powerful tool to solve a wide class of problems (Zienkiewicz, 1977; Shah et al, 1982). Two approaches are possible in the formulation of boundary integral equation methods. One is known as the *indirect method* and the other is the *direct method*. In the indirect formulation, boundary solutions are obtained by using sources or dipoles which, sometimes, lack physical interpretation. The direct formulation is the one usually associated with *boundary elements*. This is mathematically sophisticated and lends itself to refinements more easily than the indirect method. Moreover the indirect method can be interpreted as a particular case of the direct one (Brebbia, 1978).

1.3 Literature review:

In this section, the literature pertaining to the three problems at hand is presented.

1.3.1. Scattering by three dimensional inhomogeneities in an infinite medium:

Two-dimensional scattering problems have been well studied by many authors. Sezawa (1927) is credited with initiating a general treatment of the scattering of waves by a circular cylinder. After Sezawa's work there appears to have been very little done until the late 1950's, when interest in the subject revived. This led to numerous publications. Of particular significance are the works of Miles (1960) on scattering of P and SV waves by cylindrical rigid inclusions, of Thau and Pao (1966,1967) on scattering by parabolic cylindrical obstacles and of Baron and Matthews (1961) and Miklowitz (1964) on transient response. We note here that Pao and Mow (1973) have presented an excellent monograph

on this subject.

Solutions for three dimensional scattering are rather scant. This is due to the increased difficulties which arise with the additional dimension. Owing to the geometry, spherical inclusion problems are perhaps the easiest three dimensional problem to solve. Sezawa (1927) is the first to formulate the scattering of elastic waves by spherical inclusions. Ying and Truell (1956) investigated the scattering of pressure waves by spherical obstacles. Knopoff (1959a,1959b) also investigated this problem and that of shear wave scattering. The problem of transient wave scattering by spherical obstacles has also been solved by Mow (1965,1966), by Norwood and Miklowitz (1967), and recently by Wijeyewickrema and Keer (1989).

The references cited so far have dealt with spherical geometries. Varadan and Varadan (1976) and Tsao et al (1982) have obtained solutions for nonspherical geometry by employing the so-called *T-matrix* formulation. Recently, a numerical technique combining the finite element method with the wave function expansion procedure has been proposed to study the diffraction of elastic waves in two dimensions by cracks and cavities located in infinite or semi-infinite media (Shah et al 1982, 1983, 1985, 1987, Datta et al 1982, Datta and Shah, 1982; Abduljabbar et al 1983). The above numerical technique is extended in this thesis to study the scattering of elastic waves by spheroidal inclusions in an infinite medium.

1.3.2. Scattering of flexural waves by a cavity/crack in an infinite plate:

When a plate is subjected to external forces applied perpendicular to the plate, flexural waves are generated. These waves are of entirely different nature from the pressure and shear waves found in an elastic continuum. The scattering of flexural waves by a cavity/crack in a plate has not been given much attention in the literature. This may be

due to the lack of a simple theory for plates that takes into account the shear effects and the inherent complexities associated with the crack problems in general. Pao and Chao (1964) studied the scattering of flexural waves by circular cavities in an isotropic and infinite elastic plate by using the wave function technique. McCoy (1968) studied the effects of non-propagating flexural waves on dynamical stress concentrations. Sih and Loeber (1968) and Sih and Chen (1977) considered the scattering by a through-crack in an infinite plate. In their analysis, the excitation was such that a state of symmetric bending existed. They used the integral equation formulation, the solution of which is impossible for general unsymmetric excitation. In this thesis, the author extends the hybrid technique which combines the finite element method with flexural wave functions to study the scattering of flexural waves by a crack and a cavity.

1.3.3. Scattering of seismic waves by axisymmetric canyons on the surface of an elastic half space:

Analysis of many earthquakes indicates that the area of intense damage is highly localized. This has led many researchers to study the effect of topography and geological characteristics on the ground motion amplification during earthquakes. Kagami et al (1982,1986), and King and Tucker (1984) have studied this problem experimentally. Theoretical studies have also been made. The case of SH wave scattering has been investigated extensively due to its mathematical simplicity. The works of Trifunac (1971), Wong and Trifunac (1974), Sanchez-Sesma and Rosenbluth (1979), Dravinski (1982) and Shah et al (1982), among others, are noteworthy.

The two dimensional scattering of P and SV waves is much more complex than the SH wave case. The increased complexity is due to the mode conversion that takes place in the scattered field. Bouchon (1973) studied the effect of topography on surface motion

for incident P and SV waves. Dravinski and Mossessian (1987) studied the scattering by dipping layers of P, SV and Rayleigh waves by using the indirect boundary integral formulation. Solutions in time domain have been given by Eshraghi and Dravinski (1989a, 1989b).

Wong and Luco (1976) used an integral equation formulation to solve the scattering by three dimensional irregularities. Lee (1984) presented a solution scheme for diffraction of P, SV and SH waves by a hemispherical canyon. The method consists of expressing the wave fields in series expansions and a laborious matching of coefficients at the boundary of the scatterer. Sanchez-Sesma (1983) considered the scattering of vertically incident P wave by a hemispherical canyon. Khair et al (1989) considered the three dimensional scattering of P and SV waves by cylindrical valleys. In this thesis, A hybrid approach recently developed for two-dimensional problems (Shah et al, 1982; Khair et al, 1989; Boudon et al, 1989) is extended by the author to study the scattering of seismic waves by axisymmetric canyons on the surface of a half space. It is noted here that while this study was in progress, two papers appeared in the literature. In one (Eshraghi and Dravinski, 1989c), scattering by non-axisymmetric canyons is considered by using the wave function expansion technique. The stress-free boundary conditions on the surface of the half space are imposed locally in a least-square sense. In the other (Mossessian and Dravinski, 1989), an indirect boundary integral approach was used where the need to impose stress-free boundary conditions on the surface of the half space does not arise due to the use of three dimensional half space Green's functions. The present author has considered axisymmetric canyons by using a direct boundary element approach coupled with a finite element method. The advantages of this approach over the indirect one is explained in chapter 4.

1.4 Organization of the thesis

This thesis is concerned with the development and application of two hybrid models to study steady state elastic wave scattering problems. In Chapter 2, the formulation of the hybrid model to study the scattering of elastic waves by spheroidal inclusions in entire space is presented. The validation of this model and other numerical results are also discussed in the same chapter. Then scattering of flexural waves by a cavity as well as a crack in an infinite plate is considered. Formulation of the hybrid model and its applications are presented in Chapter 3. The hybrid model presented in the aforementioned chapters relies on wave functions for capturing the far field behaviour. A boundary integral representation of the far field results in an alternative yet powerful hybrid model. The formulation of this model employs axisymmetric Green's functions for an elastic half space. In Chapter 4, the formulation of the hybrid model and a systematic derivation of Green's functions are presented. Also discussed in the same chapter is the numerical aspects of both the Green's functions and the hybrid model. Finally, summary and significant conclusions of this research are presented in Chapter 5.

2. HYBRID MODELLING WITH WAVE FUNCTIONS FOR FULL SPACE PROBLEMS

2.1 Description of the problem

This chapter is concerned with the development of a hybrid model to study the scattering of elastic waves by an axisymmetric scatterer embedded in an isotropic elastic medium. The geometry of the problem is depicted in Fig. 2.1 where a spheroidal inclusion having diameters $2a$ and $2b$ along the x and z axes, respectively, is shown; z axis is the symmetry axis. The spheroid is prolate for $b > a$ and oblate for $b < a$. It is excited by a time harmonic plane P or SV wave that is incident obliquely to the axis of symmetry. Without loss of generality, the plane of propagation may be taken as the xz-plane. It is noted here that the use of a spheroidal inclusion is only for the purpose of illustration and the model developed below is valid for any axisymmetric cavity or inclusion.

When the incident wave strikes an inhomogeneity, it is partly scattered back and partly transmitted into the inclusion. The resulting motion is three dimensional and governed by the equation

$$(\lambda + \mu) \nabla(\nabla \cdot \mathbf{U}) - \mu \nabla \times \nabla \times \mathbf{U} = \rho \ddot{\mathbf{U}} \quad (2.1)$$

where \mathbf{U} is the displacement vector at a point, λ and μ are Lamé constants, ρ the density of the medium, ∇ is the three dimensional harmonic operator and a dot denotes differentiation with respect to time. A solution of (2.1) satisfying the radiation conditions at infinity and the continuity conditions of displacements and stresses across the boundary of the inhomogeneity is sought.

2.2 Hybrid Model: Finite element - Wave function expansion

An approximate solution of equation (2.1) satisfying the radiation and continuity conditions is obtained through the hybrid modelling. The strategy here is to draw a fictitious spherical boundary B enclosing the scatterer. The region interior to this boundary, referred to as *interior region* in the sequel, consists of the scatterer and a small region of the host medium adjacent to it. It is modelled through an assemblage of conventional finite elements. The exterior region is represented by spherical wave functions. Continuity of displacements and tractions between the interior and the exterior region is imposed on the boundary B . The model then yields displacements at the nodes on the boundary which may be used to evaluate the field at any point in the domain. It is noted here that the mesh boundary B need not be spherical; however, this choice is natural in anticipation of using spherical wave functions. Moreover, the method is conceptually applicable to all frequencies, but a proper finite element model and a sufficient number of wave functions are required.

2.3 Finite Element Formulation of the Interior Region

Consider a cylindrical coordinate system (r, ϕ, z) as shown in figure 2.2a. It is located at the center of the spheroid and shares the z -axis with the Cartesian coordinate system. The excitation due to the incident wave field is generally non-axisymmetric. In the analysis of axisymmetric bodies subjected to non-axisymmetric loadings, both the loads and displacements are expanded in Fourier series in the circumferential direction. For instance, the displacement components may be written, in cylindrical coordinate system (Fig. 2.2a), as

$$U_r(r, \phi, z, t) = \sum_{m=0}^{\infty} [\bar{U}_{rm}(r, z) \cos m\phi + \hat{U}_{rm}(r, z) \sin m\phi] e^{-i\omega t} \quad (2.2a)$$

$$U_z(r, \phi, z, t) = \sum_{m=0}^{\infty} [\bar{U}_{zm}(r, z) \cos m\phi + \hat{U}_{zm}(r, z) \sin m\phi] e^{-i\omega t} \quad (2.2b)$$

$$U_{\phi}(r, \phi, z, t) = \sum_{m=0}^{\infty} [-\bar{U}_{\phi m}(r, z) \sin m\phi + \hat{U}_{\phi m}(r, z) \cos m\phi] e^{-i\omega t} \quad (2.2c)$$

where $i = \sqrt{-1}$, the overbar denotes amplitudes of the displacement components symmetric about the $\phi = 0$ axis, the hat denotes the antisymmetric parts and m represents the circumferential harmonic number. The negative sign before $\bar{U}_{\phi m}$ has the effect of giving identical stiffness matrix for both symmetric and antisymmetric components. In the finite element analysis the amplitudes of displacement components, which are the primary unknowns, are functions of r and z only and do not depend upon ϕ . Thus, what was originally a three dimensional problem is reduced to a two dimensional problem. In writing eq. (2.2) a harmonic time variation with circular frequency ω has been assumed. This occurs throughout and may be omitted in the following for notational convenience.

The axisymmetric scatterer is acted upon by an incident P or SV wave which propagates in the xz-plane making an angle γ with the z -axis as shown in figure 2.1. Owing to the nature of excitation of these waves, only the symmetric part of the displacement components need be considered. Moreover the isotropy of the medium and the orthogonality of the trigonometric functions in eq. (2.2) render any two harmonics uncoupled. This and the linearity of the problem enable us to consider each harmonic as a separate problem and to use superposition to get the final solution. Thus the need for a division into finite elements in the ϕ -direction is replaced by the need to superpose separate solutions. In what follows, the formulation is given for a single m .

The amplitude of displacements within an element e for a harmonic m is interpolated from the nodal displacement amplitudes as

$$\{\bar{U}_m^e\} = [N^e]\{\bar{q}_m^e\} \quad (2.3)$$

where $[N^e]$ contains interpolation functions (Zienkiewicz, 1977), $\{\bar{q}_m^e\}$ is the vector of

element nodal displacement amplitudes, and

$$\{\bar{U}_m^e\} = \begin{pmatrix} \bar{U}_{rm}^e & \bar{U}_{zm}^e & \bar{U}_{\phi m}^e \end{pmatrix}^T$$

in which superscript T denotes transpose. The strains at a point are related to the displacement field through

$$\{\bar{\varepsilon}_m\} = [L]\{\bar{U}_m\} \quad (2.4)$$

where $[L]$ is an operator matrix containing first order partial derivatives, and

$$\{\bar{\varepsilon}_m\} = \begin{pmatrix} \bar{\varepsilon}_{rr_m} & \bar{\varepsilon}_{zz_m} & \bar{\varepsilon}_{\phi\phi_m} & \bar{\varepsilon}_{rz_m} & \bar{\varepsilon}_{r\phi_m} & \bar{\varepsilon}_{z\phi_m} \end{pmatrix}^T.$$

In view of equation (2.3), the strain - nodal displacement relationship for the element e may be written in the form

$$\{\bar{\varepsilon}_m^e\} = [B^e]\{\bar{q}_m^e\} \quad (2.5)$$

where

$$[B^e] = [L][N^e].$$

The stress - nodal displacement relationship is obtained from the constitutive law

$$\{\bar{\sigma}_m^e\} = [D^e]\{\bar{\varepsilon}_m^e\} \quad (2.6)$$

by substituting it into equation (2.5). Thus, we obtain

$$\{\bar{\sigma}_m^e\} = [D^e][B^e]\{\bar{q}_m^e\} \quad (2.7)$$

in which $[D^e]$ is the elasticity matrix and

$$\{\bar{\sigma}_m\} = \begin{pmatrix} \bar{\sigma}_{rr_m} & \bar{\sigma}_{zz_m} & \bar{\sigma}_{\phi\phi_m} & \bar{\sigma}_{rz_m} & \bar{\sigma}_{r\phi_m} & \bar{\sigma}_{z\phi_m} \end{pmatrix}^T.$$

The element stiffness and mass matrices can be obtained from the energy functional

$$\begin{aligned} F = & \frac{\delta_m}{2} \int_{A^e} [\{\bar{\sigma}_m^e\}^T \{\bar{\varepsilon}_m^{*e}\} - \rho^e \omega^2 \{\bar{U}_m^e\}^T \{\bar{U}_m^{*e}\}] r dr dz \\ & - \frac{\delta_m}{2} \int_{S^e} [\{\bar{R}_m^e\}^T \{\bar{U}_m^{*e}\} + \{\bar{U}_m^e\}^T \{\bar{R}_m^{*e}\}] r ds \end{aligned} \quad (2.8)$$

where $(*)$ indicates complex conjugate, \bar{R}_m^e is the traction vector on the boundary of the element, and

$$\delta_m = \begin{cases} 2\pi & , \quad m = 0 \\ \pi & , \quad m \geq 1 \end{cases} .$$

The first integral in equation (2.8) is over the area of the element while the second one is over the boundary of the element. Upon substituting equations (2.3), (2.5) and (2.7) into equation (2.8) and minimizing it, one gets for the element e

$$[[K_m^e] - \omega^2[M_m^e]]\{\bar{q}_m^e\} = \{\bar{P}_m^e\} \quad (2.9)$$

where

$$\begin{aligned} [K_m^e] &= \delta_m \int_{A^e} [B^{*e}]^T [D^e] [B^e] r dr dz \\ [M_m^e] &= \delta_m \int_{A^e} \rho^e [N^e]^T [N^e] r dr dz \end{aligned}$$

are the stiffness and consistent mass matrices respectively. In the above, $\{\bar{P}_m^e\}$ is the consistent nodal load vector. At this stage, the subscript m is dropped from expressions with the understanding that the problem is solved for each m and superposition is used to obtain the final solution.

Equation (2.9) governs the motion of the element e . The governing equation of motion of the whole interior region may be obtained through a systematic assembly procedure leading to

$$[S]\{\bar{q}\} = \{\bar{P}\} \quad (2.10)$$

where $[S]$ is the modified system stiffness matrix defined by

$$[S] = [K] - \omega^2[M]$$

in which $[K]$ and $[M]$ are, respectively, the global stiffness and mass matrices of the interior region; $\{\bar{q}\}$ is the vector of nodal displacement amplitudes and $\{\bar{P}\}$ is the vector of load amplitudes which has non-zero components corresponding to the interface degrees-of-freedom only. If the vector $\{\bar{q}\}$ of nodal displacements is separated into two parts: $\{\bar{q}_B\}$

corresponding to nodal displacements at the boundary B and $\{\bar{q}_I\}$ corresponding to nodal displacements elsewhere in the interior region, equation (2.10) becomes

$$\begin{bmatrix} S_{II} & S_{IB} \\ S_{BI} & S_{BB} \end{bmatrix} \begin{Bmatrix} \bar{q}_I \\ \bar{q}_B \end{Bmatrix} = \begin{Bmatrix} 0 \\ \bar{P}_B \end{Bmatrix} \quad (2.11)$$

in which $\{\bar{P}_B\}$ represents the amplitude of interaction forces between the interior and exterior regions.

2.4 Spherical Wave Functions for Exterior Region

The wave field in the exterior region comprises the incident and scattered waves. While the former is known, the latter is unknown.

Using Helmholtz decomposition the displacement field due to scattered waves may be written, in spherical coordinate system (Figure 2.2), as

$$\vec{U}^s = \nabla\varphi^s + \nabla \times (\vec{e}_R R \eta^s) + \frac{1}{k_s} \nabla \times \nabla \times (\vec{e}_R R \chi^s) \quad (2.12)$$

where the three potentials φ^s , η^s and χ^s satisfy

$$(\nabla^2 + k_p^2)\varphi^s = 0 \quad (2.13a)$$

$$(\nabla^2 + k_s^2)\eta^s = 0 \quad (2.13b)$$

$$(\nabla^2 + k_s^2)\chi^s = 0. \quad (2.13c)$$

In the foregoing equations, superscript s indicates scattered field, \vec{e}_R is the unit vector along the R-direction and k_p and k_s are respectively, P and SV wave numbers, and are given by

$$k_p = \omega \sqrt{\frac{\rho}{\lambda + 2\mu}} \quad (2.14a)$$

$$k_s = \omega \sqrt{\frac{\rho}{\mu}} . \quad (2.14b)$$

It may be noted that \vec{U}^s as given by equation (2.12) satisfies equation (2.1), and therefore is admissible. The solution of equation (2.13) can be expressed as a linear combination of spherical wave functions:

$$\varphi^s = \sum_{m=0}^{\infty} \sum_{n=m}^{\infty} a_{1nm} h_n(k_p R) P_n^m(\cos \theta) \cos m\phi \quad (2.15a)$$

$$\chi^s = \sum_{m=0}^{\infty} \sum_{n=m}^{\infty} a_{2nm} h_n(k_s R) P_n^m(\cos \theta) \cos m\phi \quad (2.15b)$$

$$\eta^s = \sum_{m=0}^{\infty} \sum_{n=m}^{\infty} b_{3nm} h_n(k_s R) P_n^m(\cos \theta) \sin m\phi \quad (2.15c)$$

in which a_{1nm} , a_{2nm} and b_{3nm} are unknown coefficients, $h_n()$ is spherical Hankel function of the first kind and order n , and $P_n^m(\cos \theta)$ the associated Legendre function. The wave field defined by equation (2.15) consists of outgoing waves only. Therefore the radiation conditions at infinity are satisfied.

Substituting equations (2.15a-c) into equation (2.12), one obtains

$$U_R^s = \sum_{m=0}^{\infty} \bar{U}_{Rm}^s \cos m\phi \quad (2.16a)$$

$$U_\theta^s = \sum_{m=0}^{\infty} \bar{U}_{\theta m}^s \cos m\phi \quad (2.16b)$$

$$U_\phi^s = \sum_{m=0}^{\infty} -\bar{U}_{\phi m}^s \sin m\phi \quad (2.16c)$$

where the amplitudes \bar{U}_{Rm}^s , $\bar{U}_{\theta m}^s$ and $\bar{U}_{\phi m}^s$ are expressed as

$$\bar{U}_{Rm}^s = \sum_{n=m}^{\infty} [a_{1nm} g_{R1}^n + a_{2nm} g_{R2}^n] P_n^m \quad (2.17a)$$

$$\bar{U}_{\theta m}^s = \sum_{n=m}^{\infty} [(a_{1nm} g_{\theta 1}^n + a_{2nm} g_{\theta 2}^n) \frac{dP_n^m}{d\theta} + b_{3nm} g_{\theta 3}^n \frac{P_n^m}{\sin \theta}] \quad (2.17b)$$

$$\bar{U}_{\phi m}^s = \sum_{n=m}^{\infty} [(a_{1nm} g_{\phi 1}^n + a_{2nm} g_{\phi 2}^n) \frac{P_n^m}{\sin \theta} + b_{3nm} g_{\phi 3}^n \frac{dP_n^m}{d\theta}] \quad (2.17c)$$

in which $g_{R1}^n, \dots, g_{\phi 3}^n$ are known functions and their complete expressions are given in Appendix A.

Evaluating equation (2.17) at each node lying on the boundary B , a relationship between the displacements and the unknown coefficients may be established in the form

$$\{\bar{q}_B^s\}_{sph} = [G]\{a\} \quad (2.18)$$

where $\{\bar{q}_B^s\}_{sph}$ is the vector of nodal displacement amplitudes in the spherical coordinate system due to the scattered field and $\{a\}$ contains the unknown coefficients a_{1nm}, a_{2nm} and b_{3nm} ; ($n = m, m + 1, \dots$). In writing equation (2.18), the summations in equation (2.17) are taken from $n = m$ to $n = m + N_B - 1$ where N_B is the number of nodes on the boundary B . This results in matrix $[G]$ being square. Note that the number of nodes on the boundary plays an important role on the number of wave functions included in the analysis.

The stress field due to the scattered waves may be expressed as

$$\sigma_{RR}^s = \sum_{m=0}^{\infty} \bar{\sigma}_{RR_m}^s \cos m\phi \quad (2.19a)$$

$$\sigma_{R\theta}^s = \sum_{m=0}^{\infty} \bar{\sigma}_{R\theta_m}^s \cos m\phi \quad (2.19b)$$

$$\sigma_{R\phi}^s = \sum_{m=0}^{\infty} -\bar{\sigma}_{R\phi_m}^s \sin m\phi \quad (2.19c)$$

where the amplitudes $\bar{\sigma}_{RR_m}^s, \bar{\sigma}_{R\theta_m}^s$ and $\bar{\sigma}_{R\phi_m}^s$ are given by

$$\bar{\sigma}_{RR_m}^s = \sum_{n=m}^{\infty} [a_{1nm} f_{R1}^n + a_{2nm} f_{R2}^n] P_n^m \quad (2.20a)$$

$$\bar{\sigma}_{R\theta_m}^s = \sum_{n=m}^{\infty} [(a_{1nm} f_{\theta 1}^n + a_{2nm} f_{\theta 2}^n) \frac{dP_n^m}{d\theta} + b_{3nm} f_{\theta 3}^n \frac{P_n^m}{\sin \theta}] \quad (2.20b)$$

$$\bar{\sigma}_{R\phi_m}^s = \sum_{n=m}^{\infty} [(a_{1nm} f_{\phi 1}^n + a_{2nm} f_{\phi 2}^n) \frac{P_n^m}{\sin \theta} + b_{3nm} f_{\phi 3}^n \frac{dP_n^m}{d\theta}]. \quad (2.20c)$$

Expressions for $f_{R1}^n, \dots, f_{\phi 3}^n$ are given in Appendix A.

A relationship may now be established, as was done in equation (2.18), between the interaction force vector and the unknown coefficients by evaluating the expressions for

stresses at the boundary nodes:

$$\{\bar{P}_B^s\}_{sph} = [F]\{a\} \quad (2.21)$$

where $\{\bar{P}_B^s\}_{sph}$ is the interaction force vector at the boundary B. The matrix $[F]$, which contains spherical Hankel functions, associated Legendre polynomials and their derivatives, is square since the same number of n 's, as in equation (2.18), are considered.

It is now possible to relate the boundary traction vector to boundary displacement vector by eliminating $\{a\}$ from equations (2.18) and (2.21):

$$\{\bar{P}_B^s\}_{sph} = [F][G]^{-1} \{\bar{q}_B^s\}_{sph} \quad (2.22)$$

The vectors $\{\bar{P}_B^s\}_{sph}$ and $\{\bar{q}_B^s\}_{sph}$ in the above equations are in the spherical coordinate system. They may be transformed to the cylindrical coordinate system to become

$$\{\bar{P}_B^s\} = [S_f] \{\bar{q}_B^s\} \quad (2.23)$$

where

$$[S_f] = [T]^T [F][G]^{-1}[T]$$

in which $[T]$ is the transformation matrix. The matrix $[S_f]$ is fully populated, complex valued and unsymmetric.

2.5 Global Solution

Recapitulating at this point, the load-displacement relationships for the interior region (equation 2.11) and the exterior region (equation 2.23) are available. Only the continuity of displacements and tractions at the boundary B remains to be satisfied.

The continuity conditions at the mesh boundary B may be written as

$$\{\bar{q}_B\} = \{\bar{q}_B^i\} + \{\bar{q}_B^s\} \quad (2.24a)$$

$$\{\bar{P}_B\} = \{\bar{P}_B^i\} + \{\bar{P}_B^s\} \quad (2.24b)$$

where those on the left hand side of the equation are from the interior region while those on the right hand side of the equation represent the exterior region. The superscript i denotes incident field. Substitution of equations (2.23) and (2.24) into equation (2.11) leads to

$$\begin{bmatrix} S_{II} & S_{IB} \\ S_{BI} & S_{BB} - S_f \end{bmatrix} \begin{Bmatrix} \bar{q}_I \\ \bar{q}_B \end{Bmatrix} = \begin{Bmatrix} 0 \\ \bar{P}_B^i - S_f \bar{q}_B^i \end{Bmatrix} \quad (2.25)$$

which may be solved for the unknown displacements in the interior region through conventional methods. The unknown coefficients a_{1nm} , a_{2nm} and b_{3nm} , which indicate the strength of the scattered waves in the exterior region, may now be obtained by using equations (2.24a) and (2.18).

2.6 Incident wave

The formulation presented in the previous sections requires that a quantity of interest be calculated for each harmonic m and superposition be used to obtain the final solution. However, when the angle of incidence is zero, only one harmonic number, namely $m=0$ for incident P wave and $m=1$ for incident SV wave, need to be considered. The degenerate and general cases of incidence are discussed below.

Zero angle of incidence:

Let us first consider the case of a P wave travelling along the z -axis. The incident field is defined by the potential

$$\varphi^i = \frac{1}{ik_p} e^{ik_p z}. \quad (2.26)$$

This qualifies as a *purely* axisymmetric problem since both geometry and loading are axisymmetric. In such problems, the displacement component in the circumferential direction, U_ϕ , vanishes. In addition, the radial displacement component, U_r , on the symmetry axis also vanishes,i.e.,

$$U_r(0, z) = 0 \quad (2.27)$$

and this should be imposed in the finite element code for nodes lying on the z -axis.

In the case of an SV wave travelling along the z -axis, it is convenient to define the incident field in terms of its displacement field:

$$U_r^i = e^{ik_s z} \cos \phi \quad (2.28a)$$

$$U_\phi^i = -e^{ik_s z} \sin \phi \quad (2.28b)$$

$$U_z^i = 0 \quad (2.28c)$$

A comparison of equation (2.28) with equation (2.2) reveals that the above displacement field is characterized by just one harmonic number, $m = 1$. It gives rise to the following conditions on the z -axis:

$$\bar{U}_z(0, z) = 0 \quad (2.29a)$$

$$\bar{U}_r(0, z) = \bar{U}_\phi(0, z) \quad (2.29b)$$

It is a routine matter to impose the condition given in equation (2.29a) on a finite element algorithm. The condition given by equation (2.29b) cannot be implemented, however, in the present form. We introduce two fictitious displacement components \bar{V}_r and \bar{V}_ϕ to replace \bar{U}_r and \bar{U}_ϕ through an orthogonal transformation of the form

$$\begin{Bmatrix} \bar{V}_r \\ \bar{V}_\phi \end{Bmatrix} = \begin{bmatrix} 1/\sqrt{2} & 1/\sqrt{2} \\ -1/\sqrt{2} & 1/\sqrt{2} \end{bmatrix} \begin{Bmatrix} \bar{U}_r \\ \bar{U}_\phi \end{Bmatrix} \quad (2.30)$$

which transform equation (2.29b) into

$$\bar{V}_\phi(0, z) = 0. \quad (2.31)$$

Imposition of this condition in a finite element code is straightforward.

Oblique angle of incidence:

A plane P wave incident obliquely to the axis of symmetry may be expressed mathematically in terms of its potential as

$$\phi^i = \frac{1}{ik_p} e^{ik_p(z \cos \gamma + x \sin \gamma)} \quad (2.32a)$$

or, in Fourier-Bessel series form

$$\phi^i = \frac{1}{ik_p} e^{ik_p z \cos \gamma} \sum_{m=0}^{\infty} \epsilon_m i^m J_m(k_p r \sin \gamma) \cos m\phi \quad (2.32b)$$

where γ is the angle of incidence, J_m is the Bessel function of the first kind and order m and

$$\epsilon_m = \begin{cases} 1 & , \quad m = 0 \\ 2 & , \quad m \geq 1 \end{cases} \quad (2.33)$$

For an SV wave incident obliquely to the symmetry axis, its potential may be given by

$$\chi^i = -\frac{1}{k_s \sin \gamma} e^{ik_s(z \cos \gamma + x \sin \gamma)} \quad (2.34a)$$

or, in series form

$$\chi^i = -\frac{1}{k_s \sin \gamma} e^{ik_s z \cos \gamma} \sum_{m=0}^{\infty} \epsilon_m i^m J_m(k_s r \sin \gamma) \cos m\phi \quad (2.34b)$$

It is the series form that we need for harmonic analysis. It may be noted that one can obtain equation (2.26) by substituting $m = 0$ and $\gamma = 0$ in equation (2.32b). Similarly equation (2.28) may be obtained from the substitution $m = 1$ and $\gamma = 0$ in equation (2.34b), but note that the value $\gamma = 0$ should be substituted in a limiting fashion.

The case of oblique incidence requires all the harmonics from zero to infinity. The conditions for $m = 0$ and $m = 1$ are the same as given by equations (2.27) and (2.29), respectively, and for $m \geq 2$

$$\bar{U}_r(0, z) = \bar{U}_z(0, z) = \bar{U}_\phi(0, z) = 0. \quad (2.35)$$

They don't pose any difficulty for implementation in a finite element program.

2.7 Numerical results and discussions

In designing the finite element mesh, two factors need be considered. First, there must be a sufficient number of wave functions to capture the far-field behaviour. At the outset, this might seem to have nothing to do with the finite element mesh, but we recall that the number of wave functions that could be accommodated in the model is related to N_B —the number of nodes on the boundary B (cf. eq. 2.18). A value for N_B could be arrived at in a test problem by first solving it analytically and observing the convergence of the series solution (i.e., eq. 2.15). Second, the size of each finite element should be kept within a certain limit in order to ensure that the finite element model transmit the waves effectively. The size of linear quadrilateral elements is limited to 1/8 of the minimum wave length of the types of wave being considered. The corresponding *size-factor* for the quadratic elements is 1/4. It is found that the mesh dictated by these guidelines is usually adequate; occasionally, especially at a high frequency, a finer mesh had to be used.

The validity of the proposed model is first assessed by considering the scattering of an incident P wave by a spherical cavity. The incident wave is propagating along the z -axis and is given by equation (2.26). The displacements along the circumference of the cavity are computed for discrete values of the dimensionless frequency $k_s a$ in the range 0.1–3.4 where a is the radius of the cavity. The results are found to be in close agreement with the analytical solution. The figure 2.3 illustrates the accuracy of the proposed method for the dimensionless frequency $k_s a = 1.732$. Figure 2.4 shows the results for an incident SV wave defined by equation (2.28). Although this establishes the accuracy of nodal displacements, the accuracy of the unknown coefficients in the scattered field must be evaluated. To do so, we calculate the scattering cross-section for a spherical solid inclusion surrounded by layers as shown in figure 2.5. The scattering cross-section represents the ratio of time average of

the scattered energy to the time average of the incoming energy. Expressions for scattering cross-section are given in Appendix B. Note that the evaluation of scattering cross-section requires the undetermined coefficients of the scattered field. In this and other subsequent problems, the inclusion is SiC and the host medium is Al, material properties of which are given in Appendix C. The incident wave is a *P* or an *SV* wave travelling in the direction of *z*-axis. In Tables 2.1–2.3 real and imaginary parts of the scattering cross section obtained from this study are shown along with the analytical solutions. It is seen that there is good agreement between them. Some discrepancies in solutions for low frequencies arise because the wave function expansions for the exterior region are undefined at zero frequency. A very fine mesh is to be used for higher frequencies.

The above test problems are completely defined by a single harmonic number. A wave incident obliquely demands consideration of all the harmonics. It appears that the error might build up during the superposition stage. In order to investigate this, we consider an oblique incident wave which is scattered by a solid spherical inclusion. It is found that the results for angles of incidence of 45° and 90° , given in Tables 2.4 and 2.5, agree well with the analytical solution.

A more complicated case occurs when the scatterer is a spheroid surrounded by layers (figure 2.6). This problem arise when there is an interaction zone between the reinforcing particles and the matrix and when the particles are coated. Results are presented for both prolate and oblate spheroids. The cross-section of a spheroid in the *xz*-plane is an ellipse, the geometry of which is completely defined by the lengths of the diameters along the *x* and *z* axes. For the prolate spheroidal inclusion, the diameters along the *z*-axis are $4a$ for the core solid, $4.2a$ for the first layer and $4.4a$ for the second layer. The corresponding values along the *x*-axis are $2a$, $2.2a$, and $2.4a$. In the case of oblate spheroidal inclusion, the diameters along the *z*-axis are $2b$ for the core solid, $2.2b$ for the first layer and $2.4b$ for the second layer, and the corresponding values along the *x*-axis are $4b$, $4.2b$, and $4.4b$.

The problem is easily solved by the proposed method due to the great flexibility of the finite element technique. It should be mentioned here that there is no analytical solution available for this problem. Since the number of wave functions needed to capture the behaviour of the exterior region is not known *a priori*, successively finer meshes have to be used until no significant changes occur in the computed results. Results for the prolate and oblate spheroidal inclusions are presented in figure 2.7 for various angles of incidence of P wave. It is seen that the scattering cross-section increases with the addition of layers. This is to be expected since the addition of layers of properties stiffer than the matrix increases the effective cross-section of the inclusion. The increase will of course depend on the material properties of the layers chosen. Moreover, the scattering cross-section of prolate spheroidal inclusion decreases with increasing angle of incidence. For oblate spheroidal inclusion, on the other hand, it increases with increasing angle of incidence. This is an interesting result and quite different from the result for the SV wave as shown in figure 2.8. There it is found that the maximum cross-section for a prolate spheroid occurs at increasing angles of incidence as frequency increases. For oblate spheroid, on the other hand, it occurs at decreasing angles of incidence.

For both *P* and *SV* waves it is found that the scattering cross-sections of oblate spheroids are larger than those of prolate spheroids, and both of these are larger than those of inscribed spheres. This behaviour can be used to ultrasonically characterize different inclusion shapes.

2.8 Concluding remarks

A hybrid finite element and wave function expansion technique is used here to study scattering of *P* and *SV* waves by prolate and oblate spheroids with and without interface layers between the inclusions and the matrix. It is found that the scattering cross-section increases with increasing thickness of interface layer when the mechanical properties of

the layers are intermediate between those of the inclusions and the matrix. Although this behaviour is to be expected, the actual increase depends on the material properties and the thickness of the interphase zone.

Interphase or interface zones in these problems play an important role in determining the mechanical behaviour of composite materials. The present study shows that changes in the scattering cross-sections may be used to parametrically characterize the interphase properties and thickness. However, to do so would require further investigation. In a recent paper, Datta et al (1988) have presented results of a parametric study in which a simplified model of the interface layer was used. It was assumed to be very thin across which stresses were allowed to suffer jumps. This simplified model indicates that the inertial effect of the layer plays the dominant role in determining the scattering cross-section. Further studies are needed in order to fully understand the complicated effect of the interfacial layer.

Appendix A : Wave Functions for Full Space

The terms g_{R1}^n , g_{R2}^n , $g_{\theta 1}^n$, $g_{\theta 2}^n$, $g_{\theta 3}^n$, $g_{\phi 1}^n g_{\phi 2}^n$ and $g_{\phi 3}^n$ appearing in Eqns. 2.17a–c are as follows:

$$g_{R1}^n = \frac{n}{R} h_n(k_p R) - k_p h_{n+1}(k_p R) \quad (A.1)$$

$$g_{R2}^n = n(n+1) \frac{h_n(k_s R)}{k_s R} \quad (A.2)$$

$$g_{\theta 1}^n = \frac{h_n(k_p R)}{R} \quad (A.3)$$

$$g_{\theta 2}^n = (n+1) \frac{h_n(k_s R)}{k_s R} - h_{n+1}(k_s R) \quad (A.4)$$

$$g_{\theta 3}^n = m h_n(k_s R) \quad (A.5)$$

$$g_{\phi 1}^n = m \frac{h_n(k_p R)}{R} \quad (A.6)$$

$$g_{\phi 2}^n = m \left\{ (n+1) \frac{h_n(k_s R)}{k_s R} - h_{n+1}(k_s R) \right\} \quad (A.7)$$

$$g_{\phi 3}^n = h_n(k_s R) \quad (A.8)$$

The terms f_{R1}^n , f_{R2}^n , $f_{\theta 1}^n$, $f_{\theta 2}^n$, $f_{\theta 3}^n$, $f_{\phi 1}^n f_{\phi 2}^n$ and $f_{\phi 3}^n$ appearing in Eqns. 2.20a–c are as follows:

$$f_{R1}^n = \frac{2\mu}{R^2} \left[(n^2 - n - \frac{1}{2} k_s^2 R^2) h_n(k_p R) + 2k_p R h_{n+1}(k_p R) \right] \quad (A.9)$$

$$f_{R2}^n = \frac{2\mu}{R^2} \frac{n(n+1)}{k_s} \left[(n-1) h_n(k_s R) - k_s R h_{n+1}(k_s R) \right] \quad (A.10)$$

$$f_{\theta 1}^n = \frac{2\mu}{R^2} \left[(n-1) h_n(k_p R) - k_p R h_{n+1}(k_p R) \right] \quad (A.11)$$

$$f_{\theta 2}^n = \frac{2\mu}{k_s R^2} \left[(n^2 - 1 - \frac{1}{2} k_s^2 R^2) h_n(k_s R) + k_s R h_{n+1}(k_s R) \right] \quad (A.12)$$

$$f_{\theta 3}^n = -m \frac{\mu}{R} \left[k_s R h_{n+1}(k_s R) - (n-1) h_n(k_s R) \right] \quad (A.13)$$

$$f_{\phi 1}^n = m f_{\theta 1}^n \quad (A.14)$$

$$f_{\phi 2}^n = m f_{\theta 2}^n \quad (A.15)$$

$$f_{\phi 3}^n = \frac{1}{m} f_{\theta 3}^n \quad (A.16)$$

Appendix B : Scattering Cross Sections for Full Space

The expressions for scattering cross-sections for the various incident fields are given below:

a. P wave, angle of incidence $\gamma = 0$.

$$\begin{aligned}\Sigma_p &= \frac{4\pi}{k_1} \text{Im} \left\{ \sum_{n=0}^{\infty} (-i)^n a_{1mn} P_n^m(\cos \theta) \right\}_{\theta=0, m=0} \\ &= \text{Im} \left[\frac{4\pi}{k_1^2} A_p(0) \right] \quad (B.1)\end{aligned}$$

b. SV wave, angle of incidence $\gamma = 0$.

$$\begin{aligned}\Sigma_s &= \frac{4\pi}{k_2^2} \text{Im} \sum_{n=0}^{\infty} (-i)^n \left\{ a_{2mn} \frac{dP_n^m}{d\theta} - i b_{3mn} m \frac{P_n^m}{\sin \theta} \right\}_{\theta=0, m=1} \\ &= \text{Im} \left[\frac{4\pi}{k_2^2} A_s(0) \right] \quad (B.2)\end{aligned}$$

c. P wave, angle of incidence $\gamma \neq 0$.

$$\begin{aligned}\Sigma_p &= \frac{4\pi}{k_1} \text{Im} \left\{ \sum_{m=0}^{\infty} \sum_{n=m}^{\infty} (-i)^n a_{1mn} P_n^m(\cos \theta) \right\}_{\theta=\gamma} \\ &= \text{Im} \left[\frac{4\pi}{k_1^2} A_p(\gamma) \right] \quad (B.3)\end{aligned}$$

d. SV wave, angle of incidence $\gamma \neq 0$.

$$\begin{aligned}\Sigma_s &= \frac{4\pi}{k_2^2} \text{Im} \left\{ \sum_{m=0}^{\infty} \sum_{n=m}^{\infty} (-i)^n \left[a_{2mn} \frac{dP_n^m}{d\theta} - i b_{3mn} m \frac{P_n^m}{\sin \theta} \right] \right\}_{\theta=\gamma} \\ &= \text{Im} \left[\frac{4\pi}{k_2^2} A_s(\gamma) \right] \quad (B.4)\end{aligned}$$

Appendix C : Material Properties

In this study we considered a SiC inclusion in Al matrix.

$$\text{SiC: } (\lambda + 2\mu, \mu) = (4.742, 1.881) \times 10^{11} \text{ N/M}^2, \rho = 3.181 \text{ gm/cm}^3$$

$$\text{Al: } (\lambda + 2\mu, \mu) = (1.105, 0.267) \times 10^{11} \text{ N/M}^2, \rho = 2.706 \text{ gm/cm}^3$$

The layers smooth out the abrupt transition of material properties between the inclusion and the host medium. The material properties of the layers given below are calculated at the mid-point of each layer assuming a linear variation from the boundary of the inclusion to the matrix medium.

Case 1: One layer (Fig. 2.5b, 2.6b).

$$\text{Layer: } (\lambda + 2\mu, \mu) = (2.9235, 1.074) \times 10^{11} \text{ N/M}^2, \rho = 2.9435 \text{ gm/cm}^3$$

Case 2: Two layers (Fig. 2.5b, 2.6c).

$$\text{Layer 1: } (\lambda + 2\mu, \mu) = (3.833, 1.478) \times 10^{11} \text{ N/M}^2, \rho = 3.062 \text{ gm/cm}^3$$

$$\text{Layer 2: } (\lambda + 2\mu, \mu) = (2.014, 0.671) \times 10^{11} \text{ N/M}^2, \rho = 2.825 \text{ gm/cm}^3$$

Table 2.1

Comparison of analytical and numerical results for real and imaginary parts of $4\pi/k_p^2 A_p(0)$ and $4\pi/k_s^2 A_s(0)$ for scattering by spherical SiC particles in Al matrix

$$(a) \text{ P - wave , } \gamma = 0^\circ, \frac{4\pi}{k_p^2} A_p(0)$$

$k_s a$	$k_p a$ $= 0.4916 k_s a$	Analytical		Hybrid Model	
		Re	Im	Re	Im
0.1	0.0491	-0.1869	0.2671×10^{-4}	-0.1878	0.2109×10^{-4}
0.5	0.2458	-0.8951	0.0143	-0.9050	0.0114
1.0	0.4916	-1.6530	0.1585	-1.6653	0.1440
1.5	0.7373	-2.2930	0.5296	-2.2865	0.4885
2.0	0.9831	-2.2853	1.1100	-2.7950	1.0637

$$(b) \text{ SV - wave , } \gamma = 0^\circ, \frac{4\pi}{k_s^2} A_s(0)$$

$k_s a$	$k_p a$ $= 0.4916 k_s a$	Analytical		Hybrid Model	
		Re	Im	Re	Im
0.1	0.0431	-0.5899	0.1452×10^{-4}	-0.6101	0.1324×10^{-3}
0.5	0.2458	-2.7890	0.7366×10^{-1}	-2.8475	0.7098×10^{-1}
1.0	0.4916	-5.0530	0.7031	-5.1378	0.6837
1.5	0.7373	-6.9370	1.9600	-6.9702	1.9272
2.0	0.9831	-8.3360	3.5660	-8.2169	3.5430

Table 2.2

Comparison of analytical and numerical results for $4\pi/k_p^2 A_p(0)$ and $4\pi/k_s^2 A_s(0)$ for scattering by a SiC particle with one interface layer in Al matrix

$$(a) \text{ P - wave , } \gamma = 0^\circ, \frac{4\pi}{k_p^2} A_p(0)$$

$k_s a$	$k_p a$ $= 0.4916 k_s a$	Analytical		Hybrid Model	
		Re	Im	Re	Im
0.1	0.0491	-0.2373	0.4232×10^{-4}	-0.2397	0.3549×10^{-4}
0.5	0.2458	-1.1340	0.2212×10^{-1}	-1.1490	0.1865×10^{-1}
1.0	0.4916	-2.0740	0.2339	-2.0920	0.2175
1.5	0.7373	-2.8640	0.7504	-2.8620	0.7095
2.0	0.9831	-3.5440	1.5570	-3.4860	1.5044

$$(b) \text{ SV - wave , } \gamma = 0^\circ, \frac{4\pi}{k_s^2} A_s(0)$$

$k_s a$	$k_p a$ $= 0.4916 k_s a$	Analytical		Hybrid Model	
		Re	Im	Re	Im
0.1	0.0491	-0.7551	0.2322×10^{-3}	-0.7782	0.2192×10^{-3}
0.5	0.2458	-3.5440	0.1140	-3.6080	0.1110
1.0	0.4916	-6.3730	1.0220	-6.4600	1.0020
1.5	0.7373	-8.6610	2.7280	-8.6810	2.6920
2.0	0.9831	-10.210	4.8420	-10.050	4.8020

Table 2.3

Comparison of analytical and numerical results for $4\pi/k_p^2 A_p(0)$ and $4\pi/k_s^2 A_s(0)$ for scattering by a SiC particle with two interface layers in Al matrix

$$(a) \text{ P - wave , } \gamma = 0^\circ, \frac{4\pi}{k_p^2} A_p(0)$$

$k_s a$	$k_p a$ $= 0.4916 k_s a$	Analytical		Hybrid Model	
		Re	Im	Re	Im
0.1	0.0491	-0.2883	0.6212×10^{-4}	-0.2924	0.5423×10^{-4}
0.5	0.2458	-1.3710	0.3172×10^{-1}	-1.3940	0.2778×10^{-1}
1.0	0.4916	-2.4340	0.3223	-2.5210	0.3053
1.5	0.7373	-3.4320	1.0070	-3.4394	0.9660
2.0	0.9831	-4.2300	2.0620	-4.1804	2.0100

$$(b) \text{ SV - wave , } \gamma = 0^\circ, \frac{4\pi}{k_s^2} A_s(0)$$

$k_s a$	$k_p a$ $= 0.4916 k_s a$	Analytical		Hybrid Model	
		Re	Im	Re	Im
0.1	0.0491	-0.9238	0.3428×10^{-3}	-0.9494	0.3252×10^{-3}
0.5	0.2458	-4.3070	0.1632	-4.3820	0.1602
1.0	0.4916	-7.7000	1.3840	-7.8010	1.3650
1.5	0.7373	-10.370	3.5670	-10.390	3.5350
2.0	0.9831	-12.020	6.2050	-11.860	6.1610

Table 2.4

Comparison of analytical and numerical results for $4\pi/k_p^2 A_p(\frac{\pi}{4})$ and $4\pi/k_s^2 A_s(\frac{\pi}{4})$ for scattering by a SiC particle in Al matrix when the angle of incidence is 45°

$$(a) \text{ P - wave , } \gamma = 45^\circ, \quad \frac{4\pi}{k_p^2} A_p(\frac{\pi}{4})$$

$k_s a$	$k_p a$ $= 0.4916 k_s a$	Total		Analytical	
		Re	Im	Re	Im
0.1	0.0491	-0.1906	0.2330×10^{-4}	-0.1869	0.2671×10^{-4}
0.5	0.2458	-0.9180	0.0125	-0.8951	0.0143
1.0	0.4916	-1.6768	0.1495	-1.6530	0.1585
1.5	0.7373	-2.3098	0.5025	-2.2930	0.5296
2.0	0.9831	-2.8397	1.0833	-2.8530	1.1100

$$(b) \text{ SV - wave , } \gamma = 45^\circ, \quad \frac{4\pi}{k_s^2} A_s(\frac{\pi}{4})$$

$k_s a$	$k_p a$ $= 0.4916 k_s a$	Total		Analytical	
		Re	Im	Re	Im
0.1	0.0491	-0.7330	0.1287×10^{-3}	-0.5899	0.1452×10^{-3}
0.5	0.2458	-2.9078	0.6721×10^{-1}	-2.7890	0.7366×10^{-1}
1.0	0.4916	-5.1471	0.6827	-5.0530	0.7031
1.5	0.7373	-6.9836	1.9287	-6.9370	1.9600
2.0	0.9831	-8.2709	3.5468	-8.3360	3.5660

Table 2.5

Comparison of analytical and numerical results for $4\pi/k_p^2 A_p(\frac{\pi}{2})$ and $4\pi/k_s^2 A_s(\frac{\pi}{2})$ for scattering by a SiC particle in Al matrix when the angle of incidence is 90°

$$(a) \text{ P - wave , } \gamma = 90^\circ, \quad \frac{4\pi}{k_p^2} A_p(\frac{\pi}{2})$$

$k_s a$	$k_p a$ $= 0.4916 k_s a$	Total		Analytical	
		Re	Im	Re	Im
0.1	0.0491	-0.1927	0.2478×10^{-4}	-0.1869	0.2671×10^{-4}
0.5	0.2458	-0.9276	0.0133	-0.8951	0.0143
1.0	0.4916	-1.6841	0.1535	-1.6530	0.1585
1.5	0.7373	-2.3251	0.5136	-2.2930	0.5296
2.0	0.9831	-2.8701	1.1004	-2.8530	1.1100

$$(b) \text{ SV - wave , } \gamma = 90^\circ, \quad \frac{4\pi}{k_s^2} A_s(\frac{\pi}{2})$$

$k_s a$	$k_p a$ $= 0.4916 k_s a$	Total		Analytical	
		Re	Im	Re	Im
0.1	0.0491	-0.6016	0.1401×10^{-3}	-0.5899	0.1452×10^{-3}
0.5	0.2458	-2.8455	0.7165×10^{-1}	-2.7890	0.7366×10^{-1}
1.0	0.4916	-5.1110	0.7031	-5.0530	0.7031
1.5	0.7373	-6.9980	1.9760	-6.9370	1.9600
2.0	0.9831	-8.3720	3.6120	-8.3360	3.5660

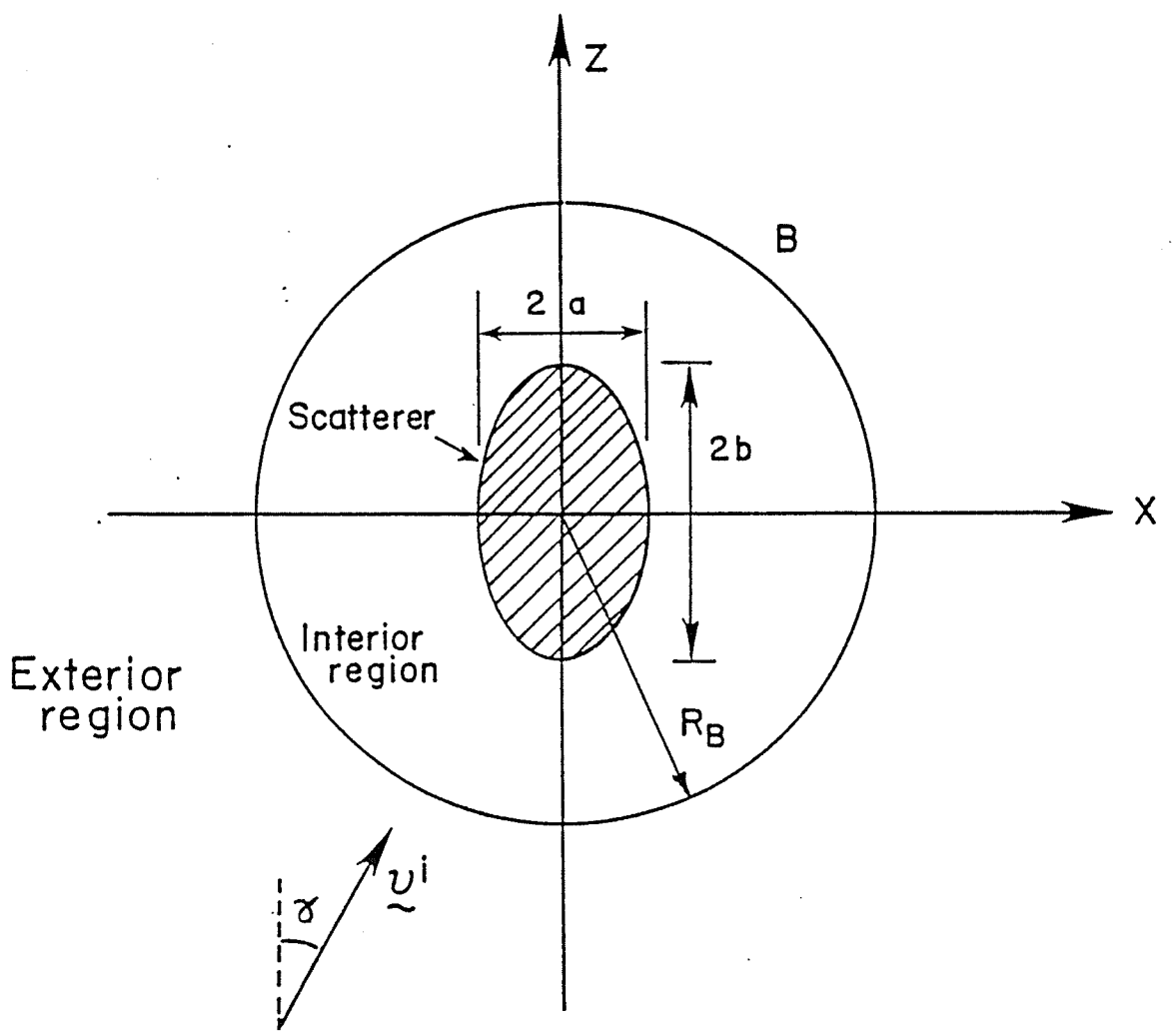
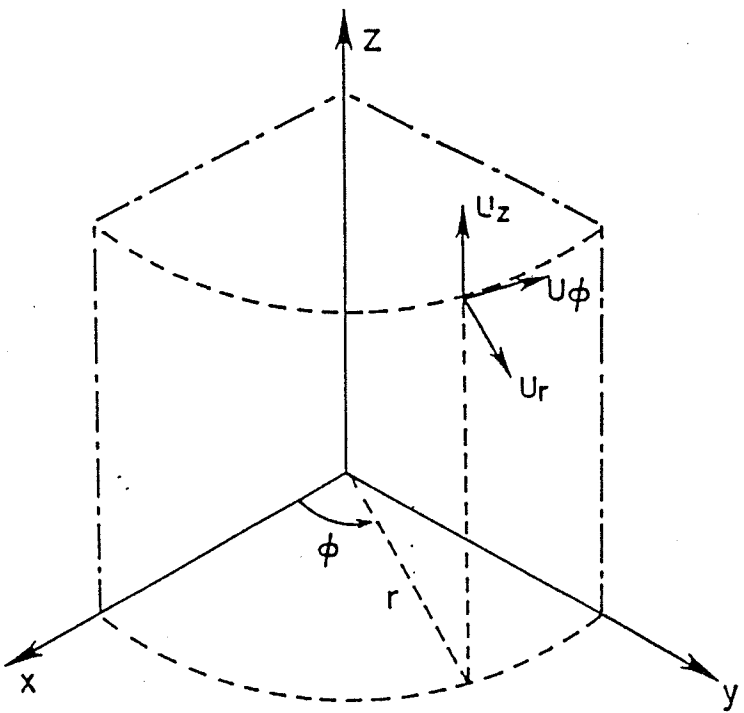
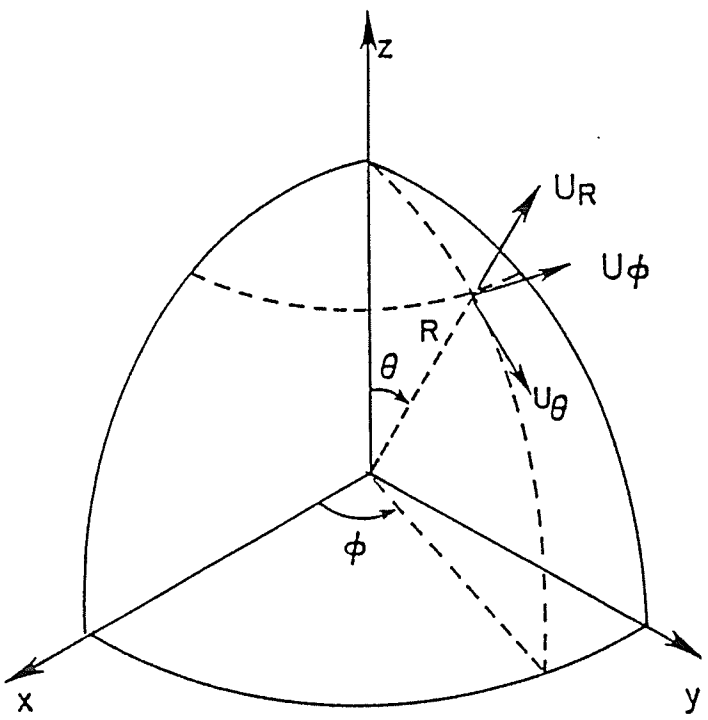


Figure 2.1 : Geometry of the problem



(a) Cylindrical Coordinate System



(b) Spherical Coordinate System

Figure 2.2 : Coordinate systems

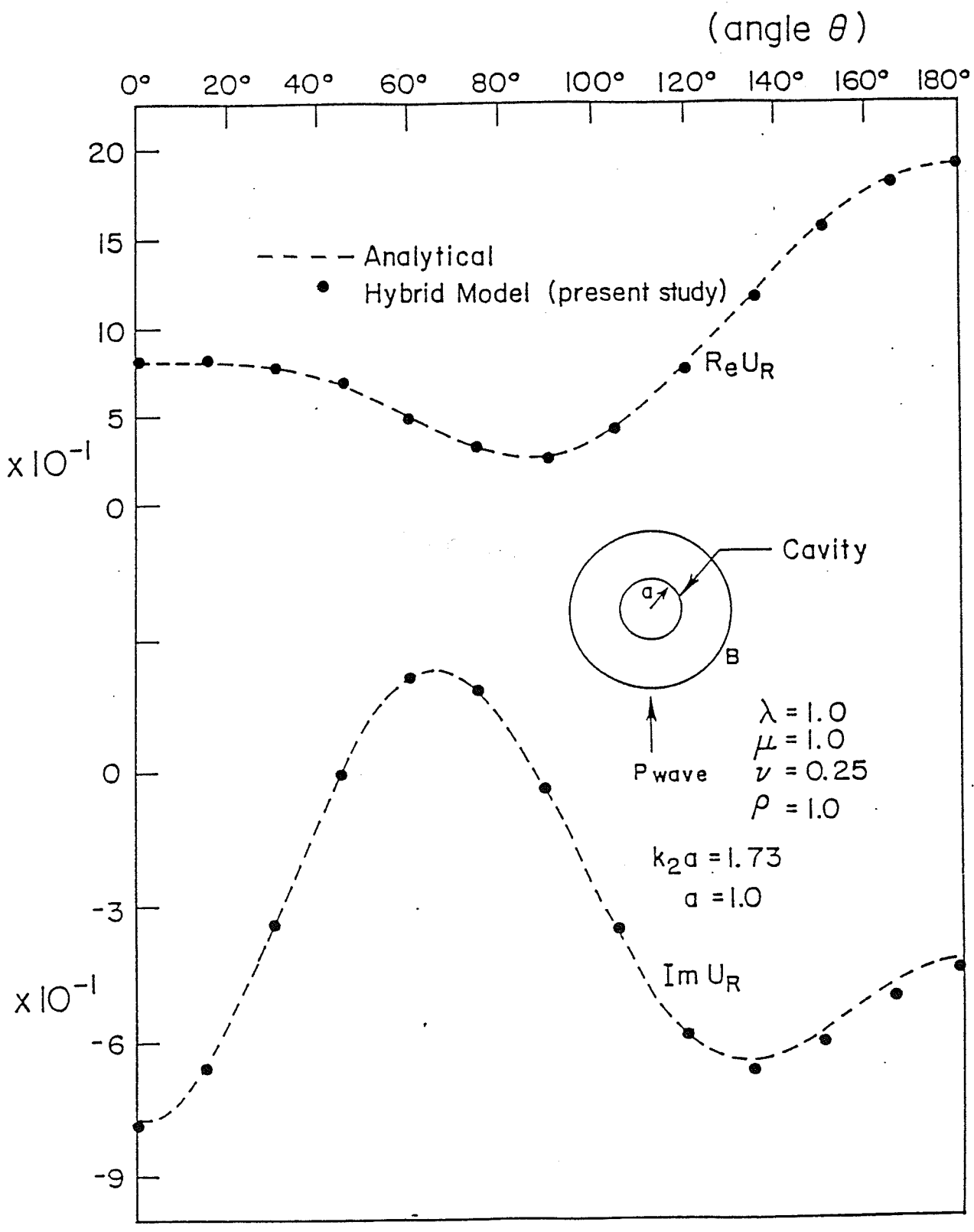


Figure 2.3 : Displacement on the surface of the cavity

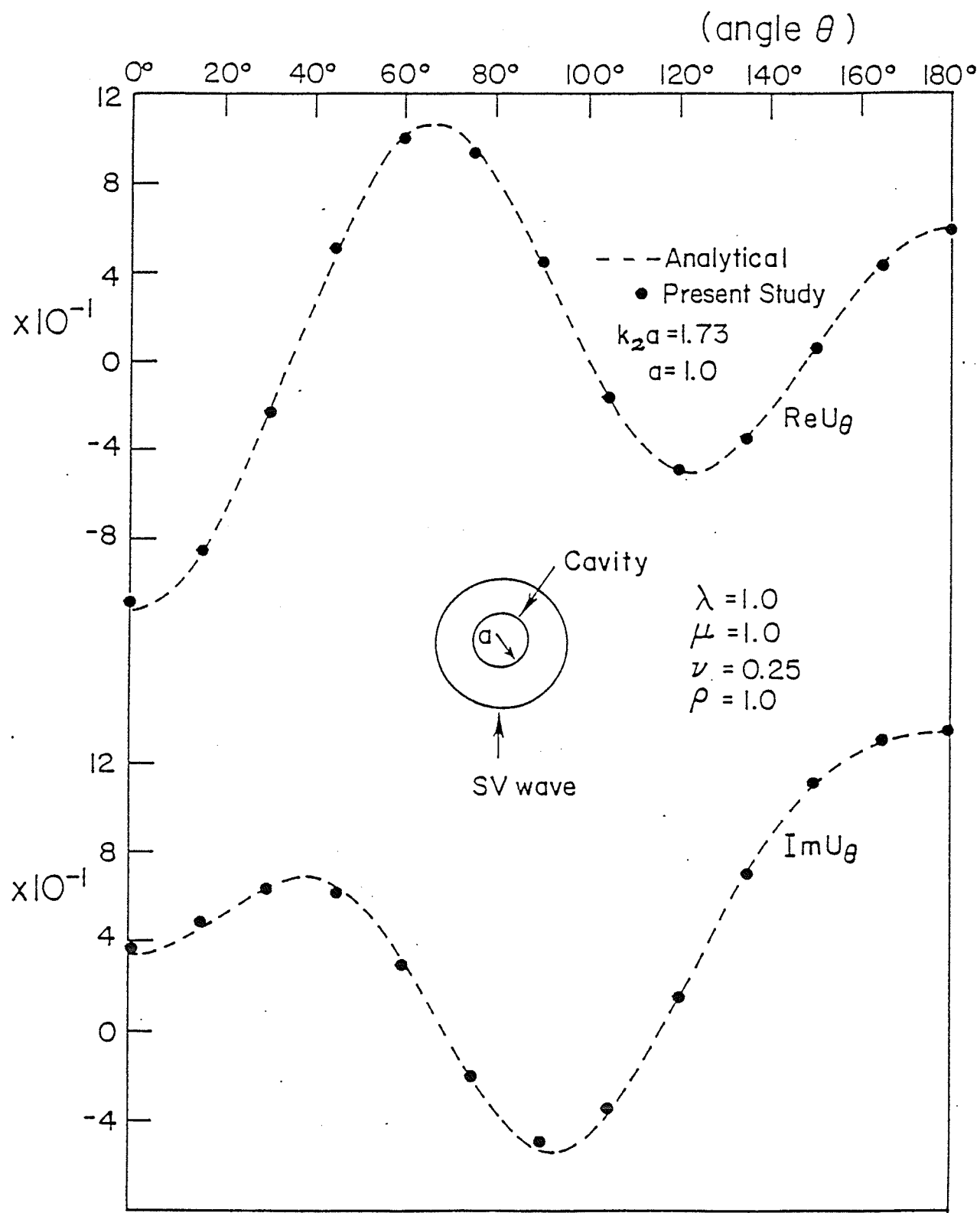
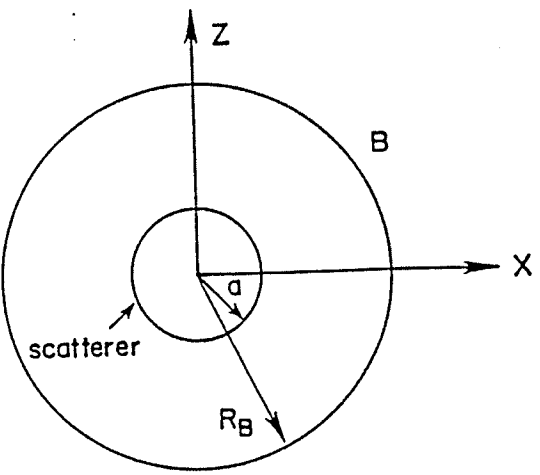
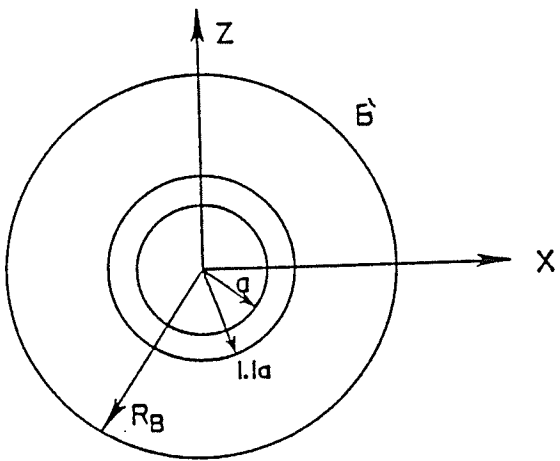


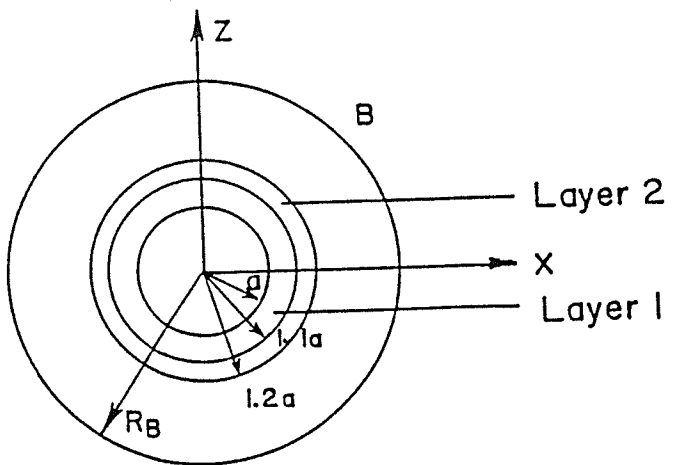
Figure 2.4 : Displacement on the surface of the cavity



(a) No Layer

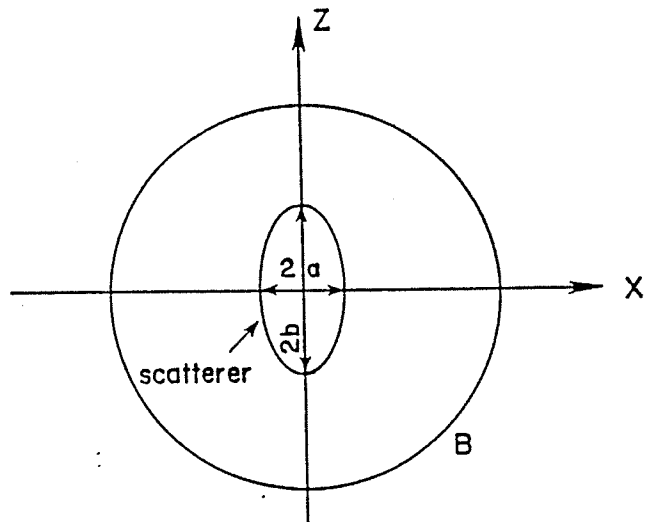


(b) One Layer

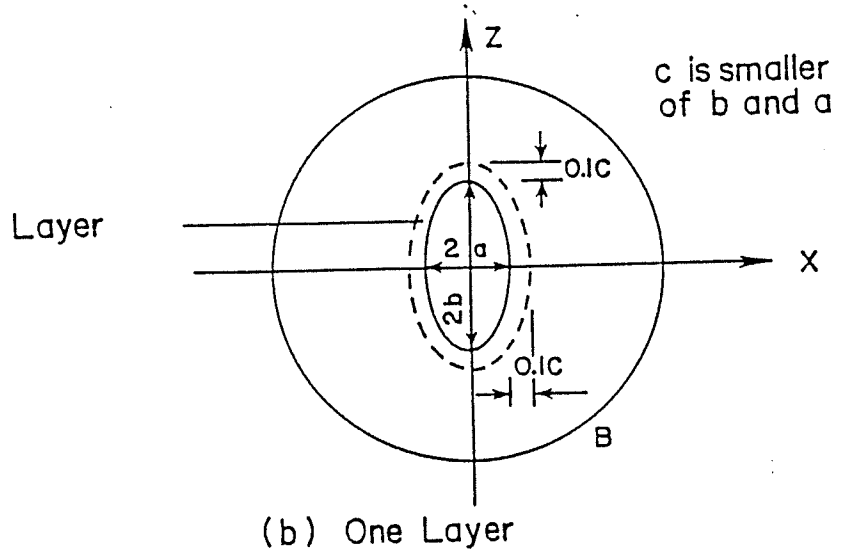


(c) Two Layers

Figure 2.5 : Geometry of the spherical scatterer



(a) No Layer



(b) One Layer

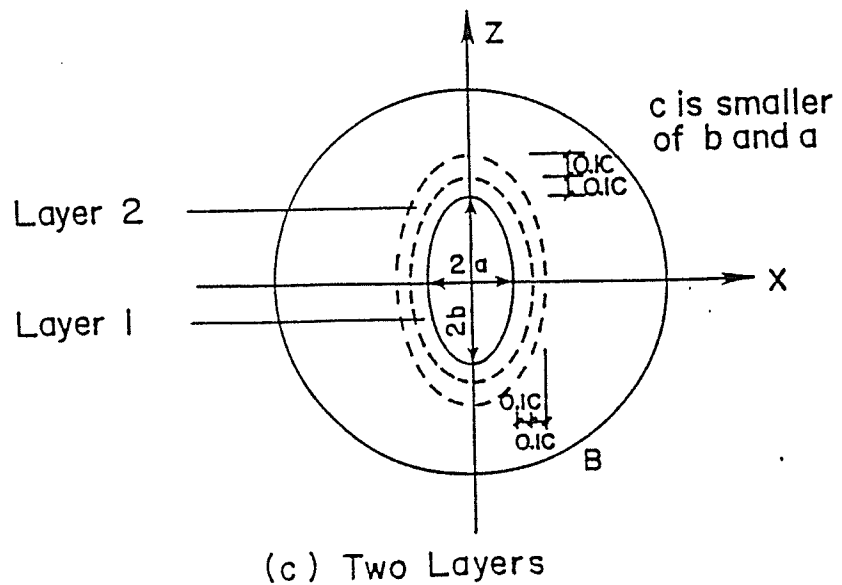


Figure 2.6 : Geometry of the spheroidal scatterer

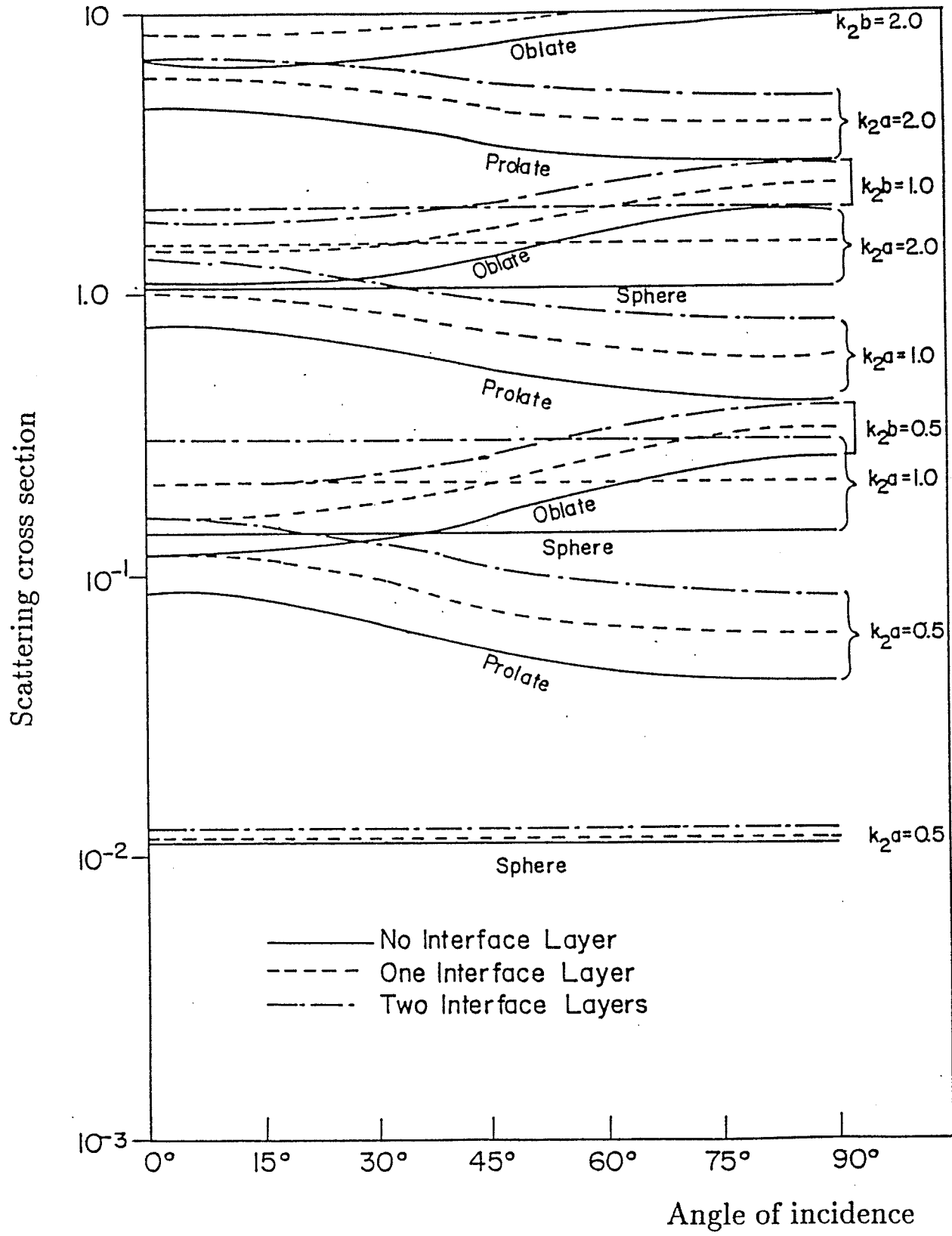


Figure 2.7 : Scattering cross section of spheroidal inclusion
for incident P waves

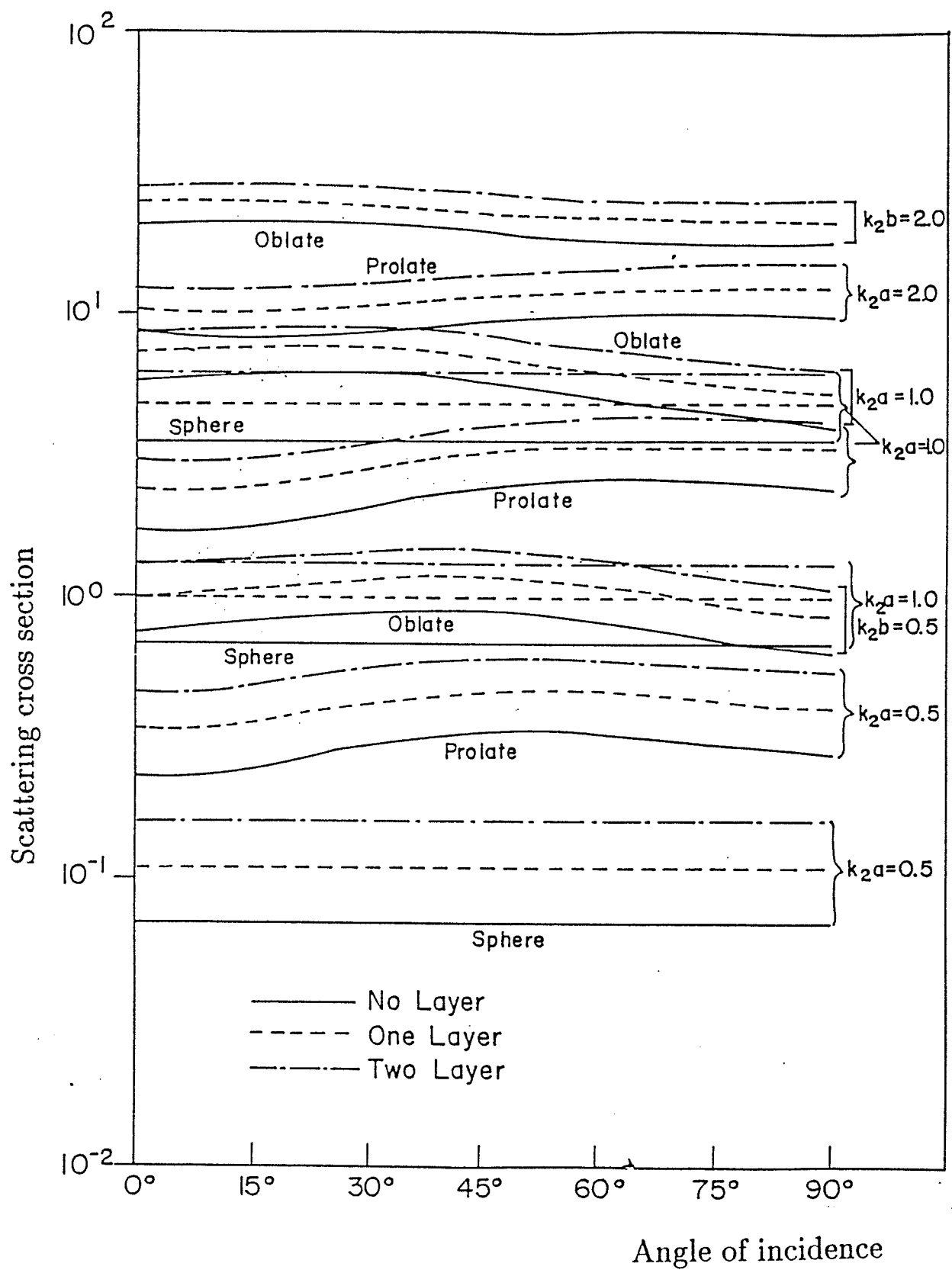


Figure 2.8 : Scattering cross section of spheroidal inclusion
for incident SV waves

3. HYBRID MODELLING WITH WAVE FUNCTIONS FOR PLATE PROBLEMS

3.1 Introduction

In this chapter, the scattering of flexural waves by an inhomogeneity in the form of a hole or a through-crack in an isotropically elastic infinite plate is considered. The geometry of the problem is depicted in figure 3.1. The plate is excited by a wave incident obliquely making an angle γ to the x -axis. The incident wave may be thought of as being emitted by a source which may be a force applied perpendicularly to the plate, varying harmonically in time and located at a distance sufficiently far away from the inhomogeneity. In essence, we are dealing with a *flexure* problem and the waves encountered may be referred to as flexural waves.

To investigate the scattering of flexural waves in a plate, either the classical thin plate theory or Mindlin's thick plate theory may be used. Whereas the thin plate theory is valid for low frequencies and long wave lengths, Mindlin's theory is valid even for moderately high frequencies. Based on Mindlin's theory, the waves in a plate in flexure may be divided into three types, namely, slow flexural, fast flexural and thickness shear waves. When any one of these waves passes through an inhomogeneity, part of it is scattered back into three waves. Thus the combination of the incident and the three scattered waves constitute the total wave field in a plate.

3.2 Mindlin's Theory

It is convenient to introduce Cartesian coordinates (x,y,z) with the xy -plane coinciding with the middle plane of the plate. Let h be thickness of the plate. Thus, $z = \pm h/2$ designate the faces of the plate. In Mindlin's theory for flexural vibration of plates (Mindlin,1951), the displacement components, when referred to a Cartesian coordinate

system, are assumed as

$$U_x(x, y, z, t) = z\psi_x(x, y, t) \quad (3.1a)$$

$$U_y(x, y, z, t) = z\psi_y(x, y, t) \quad (3.1b)$$

$$U_z(x, y, z, t) = w(x, y, t) \quad (3.1c)$$

where w is the lateral displacement, ψ_x and ψ_y are rotations in the xz and yz planes, respectively. Thus the displacement at any point is completely defined by the generalized displacement components w, ψ_x and ψ_y .

The equations of motion, in index notation, of a three dimensional elastic body

$$\sigma_{ij,j} = \rho \ddot{U}_i \quad (3.2)$$

may be converted to plate-displacement equations of motion by using equation (3.1) with the result

$$\frac{D}{2} [(1 - \nu) \nabla^2 \psi_x + (1 + \nu) \frac{\partial \Phi}{\partial x}] - \kappa^2 \mu h (\psi_x + \frac{\partial w}{\partial x}) = \frac{\rho h^3}{12} \frac{\partial^2 \psi_x}{\partial t^2} \quad (3.3a)$$

$$\frac{D}{2} [(1 - \nu) \nabla^2 \psi_y + (1 + \nu) \frac{\partial \Phi}{\partial y}] - \kappa^2 \mu h (\psi_y + \frac{\partial w}{\partial y}) = \frac{\rho h^3}{12} \frac{\partial^2 \psi_y}{\partial t^2} \quad (3.3b)$$

$$\kappa^2 \mu h (\nabla^2 w + \Phi) = \rho h \frac{\partial^2 w}{\partial t^2} \quad (3.3c)$$

where ∇^2 is Laplace's two-dimensional operator, ρ is mass density, h is plate thickness, ν is Poisson's ratio, D is flexural rigidity, μ is shear modulus, κ^2 is shear correction factor and

$$\Phi = \frac{\partial \psi_x}{\partial x} + \frac{\partial \psi_y}{\partial y}.$$

If a harmonic time variation is assumed, a solution of equation (3.3) may be written in terms of three potentials $\varphi_1(x, y)$, $\varphi_2(x, y)$, and $\varphi_3(x, y)$ as

$$\psi_x = (\sigma_1 - 1) \frac{\partial \varphi_1}{\partial x} + (\sigma_2 - 1) \frac{\partial \varphi_2}{\partial x} + \frac{\partial \varphi_3}{\partial y} \quad (3.4a)$$

$$\psi_y = (\sigma_1 - 1) \frac{\partial \varphi_1}{\partial y} + (\sigma_2 - 1) \frac{\partial \varphi_2}{\partial y} - \frac{\partial \varphi_3}{\partial x} \quad (3.4b)$$

$$w = \varphi_1 + \varphi_2 \quad (3.4c)$$

where each potential satisfies a Helmholtz equation

$$(\nabla^2 + \delta_i^2)\varphi_i = 0 \quad i = 1, 2, 3. \quad (3.5)$$

In the foregoing equations

$$\delta_1^2, \delta_2^2 = \frac{1}{2}\delta_0^4\{(R + S) \pm \sqrt{(R - S)^2 + 4\delta_0^{-4}}\} \quad (3.6a)$$

$$\sigma_1, \sigma_2 = (R\delta_0^4 - S^{-1})^{-1}(\delta_2^2, \delta_1^2) \quad (3.6b)$$

$$\delta_3^2 = 2(R\delta_0^4 - S^{-1})/(1 - \nu) \quad (3.6c)$$

$$R = \frac{h^2}{12}, \quad S = \frac{D}{\kappa^2 Gh}, \quad \delta_0^4 = \frac{\rho\omega^2 h}{D}. \quad (3.6d)$$

The potentials φ_i , $i = 1, 2, 3$ generate, respectively, the slow flexural, the fast flexural and the thickness shear waves. The three wave numbers δ_i , $i = 1, 2, 3$ are dependent on the frequency. Thus, all three flexural waves are dispersive. In addition, δ_1 is real for all frequencies, whereas δ_2 and δ_3 may be real or imaginary depending upon whether the frequency of excitation, ω , is greater or smaller than the cut-off frequency ω_0 where

$$\omega_0 = \frac{\pi}{h} \sqrt{\frac{\mu}{\rho}}. \quad (3.7)$$

The objective now is to determine a solution of equation (3.5) satisfying the boundary and radiation conditions.

3.3 Hybrid Model: Finite Element - Wave Function Expansion

A hybrid model that combines the finite element method with the wave function expansion procedure is used here to study this problem. The model consists of dividing the entire domain into an interior region and an exterior region by drawing a fictitious circular boundary B (figure 3.2). The interior region which encloses all the inhomogeneities is modelled by conventional finite elements. Flexural wave functions are adopted to represent the exterior region. The two apparently different representations are coupled by imposing the continuity of displacements and interaction forces along the common boundary B.

This results in a set of equations which enables determination of the field at any point of interest.

3.4 Finite element formulation of the interior region

A typical finite element discretization of the interior region is shown in figure 3.3 where the inhomogeneity is a circular cavity. The 9-noded isoparametric Mindlin type plate bending elements are made use of in the modelling process. The 4 noded isoparametric or the *heterosis* elements may also be used. The formulation of these elements is very similar to that of axisymmetric elements given in Chapter 2 (Hughes, 1987). Therefore, only the relevant details will be given here to underscore the discussion.

In Mindlin's theory for flexural vibration of plates, the displacement at any point is completely defined by the components of the generalized displacement vector $\{W\}$ through the relationship

$$\begin{Bmatrix} U_x \\ U_y \\ U_z \end{Bmatrix} = \begin{bmatrix} z & 0 & 0 \\ 0 & z & 0 \\ 0 & 0 & 1 \end{bmatrix} \{W\} \quad (3.8)$$

where

$$\{W\} = (\psi_x \ \psi_y \ w)^T. \quad (3.9)$$

In writing equation (3.8) a harmonic time variation of the form $\exp(-i\omega t)$ is assumed where ω is the circular frequency. It is omitted in the following when its existence is apparent.

The generalized displacement components at a point within an element e may be interpolated from the nodal values as

$$\{W^e\} = [N^e]\{q^e\} \quad (3.10)$$

where $[N^e]$ contains interpolation functions and $\{q^e\}$ is the vector of nodal displacements. A form of constitutive law relates the stress resultants, i.e., bending moments $\{M\}$ and shear forces $\{Q\}$, to the generalized strain components $\{\varepsilon_b\}$ and $\{\varepsilon_s\}$ via the expressions

$$\{M\} = [D_b]\{\varepsilon_b\} \quad (3.11a)$$

$$\{Q\} = [D_s]\{\varepsilon_s\} \quad (3.11b)$$

where

$$\{M\} = \langle M_x \ M_y \ M_{xy} \rangle^T \quad (3.12a)$$

$$\{Q\} = \langle Q_x \ Q_y \rangle^T \quad (3.12b)$$

$$\{\varepsilon_b\} = \langle \frac{\partial \psi_x}{\partial x}, \frac{\partial \psi_y}{\partial y}, \frac{\partial \psi_x}{\partial y} + \frac{\partial \psi_y}{\partial x} \rangle^T \quad (3.12c)$$

$$\{\varepsilon_s\} = \langle \frac{\partial w}{\partial x} + \psi_x, \frac{\partial w}{\partial y} + \psi_y \rangle^T \quad (3.12d)$$

$$[D_b] = \frac{Eh^3}{12(1-\nu)^2} \begin{bmatrix} 1 & \nu & 0 \\ \nu & 1 & 0 \\ 0 & 0 & \frac{1-\nu}{2} \end{bmatrix} \quad (3.12e)$$

$$[D_s] = \frac{Eh\nu^2}{2(1+\nu)} \begin{bmatrix} 1 & 0 \\ 0 & 1 \end{bmatrix}. \quad (3.12f)$$

In the above equations, E is the Young's modulus. It is noted here that the Mindlin's value of $\pi^2/12$ is assumed for the shear correction factor instead of the conventional Reissner's value of $5/6$. This permits direct comparison of our results with those already available in the literature.

The equation of motion of an element e may be obtained by minimizing the energy functional which is similar to equation (2.8) except that the stresses are replaced by the stress resultants. By assembling the equations of motion of all the elements, one obtains the equation of motion of the interior region which may be written as

$$[S]\{q\} = \{P\} \quad (3.13a)$$

where

$$[S] = [K] - \omega^2[M] \quad (3.13b)$$

in which $[K]$ and $[M]$ are, respectively, the global stiffness and mass matrices of the interior region; $\{q\}$ is the vector of nodal displacements and $\{P\}$ is the vector of generalized loads. It is convenient for our discussion if $\{q\}$ is partitioned into a set for the interior nodes $\{q_I\}$

and a set on the boundary $\{q_B\}$. The partitioned form of equation (3.12) can be written as

$$\begin{bmatrix} S_{II} & S_{IB} \\ S_{BI} & S_{BB} \end{bmatrix} \begin{Bmatrix} q_I \\ q_B \end{Bmatrix} = \begin{Bmatrix} 0 \\ P_B \end{Bmatrix} \quad (3.14)$$

where $\{P_B\}$ represents the interaction forces between the interior and exterior regions.

3.5 Flexural wave functions for exterior region

The system of waves that can occur in the exterior region consists of an incident wave and the three scattered waves.

Incident field:

The modelling procedure can accommodate any of the three waves that may be incident on the inhomogeneity. It is noted, however, that the fast flexural and the thickness shear waves have imaginary wave numbers (for the frequency range studied here) which correspond to attenuating modes with an exponentially decaying factor in space coordinates. Thus only the slow flexural incident wave is of interest. The expression for the incident wave is obtained from its potential which is defined as

$$\varphi_1^i = e^{i\delta_1(x \cos \gamma + y \sin \gamma)}. \quad (3.15)$$

Scattered waves:

The unknown scattered field is represented by flexural wave functions in the cylindrical coordinate system:

$$\varphi_1^s = \sum \{ A_{1n} H_n(\delta_1 r) \cos n\theta + A_{2n} H_n(\delta_1 r) \sin n\theta \} \quad (3.16a)$$

$$\varphi_2^s = \sum \{ B_{1n} K_n(\bar{\delta}_2 r) \cos n\theta + B_{2n} K_n(\bar{\delta}_2 r) \sin n\theta \} \quad (3.16b)$$

$$\varphi_3^s = \sum \{ C_{1n} K_n(\bar{\delta}_3 r) \sin n\theta + C_{2n} K_n(\bar{\delta}_3 r) \cos n\theta \} \quad (3.16c)$$

where H_n is the Hankel function of the first kind, K_n the modified Bessel function of the second kind, the unknown constants A_{1n}, B_{1n} and C_{1n} correspond to a symmetric problem,

A_{2n} , B_{2n} and C_{2n} correspond to an anti-symmetric problem and

$$\bar{\delta}_2^2 = -\delta_2^2 \quad \bar{\delta}_3^2 = -\delta_3^2.$$

All the summations in the foregoing equations and in the sequel are over integral values of n from zero to infinity. It may be noted that equation (3.16) satisfies equation (3.5) and the radiation conditions at infinity.

Expressions for generalized displacements may be obtained from equation (3.4) which, after a coordinate transformation, can be written as

$$w^s = \sum \{ [A_{1n}g_1 + B_{1n}g_2] \cos n\theta + [A_{2n}g_1 + B_{2n}g_2] \sin n\theta \} \quad (3.17a)$$

$$\begin{aligned} \psi_r^s &= \sum \{ [A_{1n}g_{r1} + B_{1n}g_{r2} + C_{1n}g_{r3}] \cos n\theta \\ &\quad + [A_{2n}g_{r1} + B_{2n}g_{r2} - C_{2n}g_{r3}] \sin n\theta \} \end{aligned} \quad (3.17b)$$

$$\begin{aligned} \psi_\theta^s &= \sum \{ [A_{1n}g_{\theta1} + B_{1n}g_{\theta2} + C_{1n}g_{\theta3}] \sin n\theta \\ &\quad - [A_{2n}g_{\theta1} + B_{2n}g_{\theta2} - C_{2n}g_{\theta3}] \cos n\theta \} \end{aligned} \quad (3.17c)$$

Expressions for $g_1, g_2, etc.$ are presented in Appendix D. Similar expressions for stress resultants required for the analysis may also be given:

$$\begin{aligned} Q_r^s &= \kappa^2 G h \sum \{ [A_{1n}Q_{r1} + B_{1n}Q_{r2} + C_{1n}Q_{r3}] \cos n\theta \\ &\quad + [A_{2n}Q_{r1} + B_{2n}Q_{r2} - C_{2n}Q_{r3}] \sin n\theta \} \end{aligned} \quad (3.18a)$$

$$\begin{aligned} M_{rr}^s &= D \sum \{ [A_{1n}M_{r1} + B_{1n}M_{r2} + C_{1n}M_{r3}] \cos n\theta \\ &\quad + [A_{2n}M_{r1} + B_{2n}M_{r2} - C_{2n}M_{r3}] \sin n\theta \} \end{aligned} \quad (3.18b)$$

$$\begin{aligned} M_{r\theta}^s &= \frac{D}{2}(1-\nu) \sum \{ [A_{1n}M_{r\theta1} + B_{1n}M_{r\theta2} + C_{1n}M_{r\theta3}] \sin n\theta \\ &\quad - [A_{2n}M_{r\theta1} + B_{2n}M_{r\theta2} - C_{2n}M_{r\theta3}] \cos n\theta \}. \end{aligned} \quad (3.18c)$$

Expressions for $Q_{r1}, Q_{r2}, etc.$, are given in Appendix D. By evaluating these expressions at each node on the mesh boundary B, the following relationships are established:

$$\{q_B^s\} = [G]\{a\} \quad (3.19a)$$

$$\{P_B^s\} = [F]\{a\} \quad (3.19b)$$

In the above, $\{a\}$ contains unknown coefficients A_{1n}, B_{1n} , etc. It is noted here that the summation of the terms containing coefficients A_{1n}, B_{1n} and C_{2n} is taken from zero to $(N_B/2) - 1$ and the summation of the terms containing coefficients A_{2n}, B_{2n} and C_{1n} is taken from zero to $N_B/2$ with N_B being the number of nodes on the mesh boundary B. This renders the matrices $[G]$ and $[F]$ square.

The far-field impedance matrix $[S_f]$ is now obtained by eliminating $\{a\}$ from equations (3.19a) and (3.19b):

$$\{P_B^s\} = [S_f]\{q_B^s\} \quad (3.20a)$$

where

$$[S_f] = [F][G]^{-1}. \quad (3.20b)$$

3.6 Global Solution

The continuity of displacements and stress resultants across the boundary B shall be addressed now. Setting the displacements and stress resultants on B from the interior region to be equal to those from the exterior region, one obtains

$$\{q_B\} = \{q_B^i\} + \{q_B^s\} \quad (3.21a)$$

$$\{P_B\} = \{P_B^i\} + \{P_B^s\}. \quad (3.21b)$$

By using equations (3.21) and (3.20a), equation (3.14) may be written as

$$\begin{bmatrix} S_{II} & S_{IB} \\ S_{BI} & S_{BB} - S_f \end{bmatrix} \begin{Bmatrix} q_I \\ q_B \end{Bmatrix} = \begin{Bmatrix} 0 \\ P_B^i - S_f q_B^i \end{Bmatrix} \quad (3.22)$$

Once the above equation is solved for nodal displacements, the unknown coefficients associated with the scattered field may be obtained from equations (3.21a) and (3.19a).

3.7 Stress intensity factors

Consider a through-the-thickness crack of length $2a$ in an infinite plate which is set into motion by an obliquely incident slow flexural wave as shown in figure 3.4. By using the hybrid model, we evaluate the stress intensity factors K_1 and K_2 in mode-1 and mode-2 respectively.

A typical finite element discretization of the interior region is shown in figure 3.5. Only one-half of the region is discretized for reasons to be explained in the next section. In designing the finite element mesh, Barsoum's degenerated crack tip elements (Barsoum, 1976) are used to incorporate the so-called inverse square root singularity at the crack tips. These crack tip elements are surrounded by a layer of transition elements (Lynn and Ingraffea, 1978). The rest are four node isoparametric elements.

The asymptotic behaviour of the moment distribution near the crack is found to be (Sih and Loeber, 1968),

$$M_x = \frac{K_1}{\sqrt{2r}} \cos \frac{\theta}{2} \left(1 - \sin \frac{\theta}{2} \sin \frac{3\theta}{2}\right) - \frac{K_2}{\sqrt{2r}} \sin \frac{\theta}{2} \left(2 + \cos \frac{\theta}{2} \cos \frac{3\theta}{2}\right) \quad (3.23a)$$

$$M_y = \frac{K_1}{\sqrt{2r}} \cos \frac{\theta}{2} \left(1 + \sin \frac{\theta}{2} \sin \frac{3\theta}{2}\right) + \frac{K_2}{\sqrt{2r}} \sin \frac{\theta}{2} \cos \frac{\theta}{2} \cos \frac{3\theta}{2} \quad (3.23b)$$

$$M_{xy} = \frac{K_1}{\sqrt{2r}} \cos \frac{\theta}{2} \sin \frac{\theta}{2} \cos \frac{3\theta}{2} + \frac{K_2}{\sqrt{2r}} \cos \frac{\theta}{2} \left(1 - \sin \frac{\theta}{2} \sin \frac{3\theta}{2}\right). \quad (3.23c)$$

The above expressions are with respect to the coordinate system located at the crack tip (figure 3.6). It is interesting to note that the moments M_x , M_y and M_{xy} possess the familiar inverse square root singularity at the crack tip. The displacement field in the neighbourhood of the crack tip that gives rise to the singularity has the form

$$\begin{aligned} U_x &= \sqrt{2r} \frac{z}{D(1-\nu)} \left\{ K_1 \cos \frac{\theta}{2} \left(1 - \frac{2\nu}{1+\nu} + \sin^2 \frac{\theta}{2}\right) \right. \\ &\quad \left. + K_2 \sin \frac{\theta}{2} \left(\frac{2}{1+\nu} + \cos^2 \frac{\theta}{2}\right) \right\} + O(r) \end{aligned} \quad (3.24a)$$

$$U_y = \sqrt{2r} \frac{z}{D(1-\nu)} \left\{ K_1 \sin \frac{\theta}{2} \left(\frac{2}{1+\nu} - \cos^2 \frac{\theta}{2}\right) \right. \\ \left. + K_2 \cos \frac{\theta}{2} \left(1 - \frac{2\nu}{1+\nu} - \sin^2 \frac{\theta}{2}\right) \right\} + O(r)$$

$$- K_2 \cos \frac{\theta}{2} \left(1 - \frac{2\nu}{1+\nu} - \sin^2 \frac{\theta}{2} \right) \} + O(r). \quad (3.24b)$$

Although the displacement and moment fields are unknown, the spacial distributions are given by equations (3.23) and (3.24) and only the amplitudes (i.e., stress intensity factors) are undetermined. The singularity in equation (3.23) entails a fine mesh around the crack tips. This leads to a system with a relatively large number of degrees of freedom causing severe penalty on computer storage and time. These problems may be somewhat mitigated by using the quarter-point crack tip elements. These elements contain terms in their displacement field proportional to the square root of the distance along lines originating from the crack tip. For instance, the displacements along the edge containing the nodes 1, 6 and 3 indicated in figure 3.6 are given by

$$U = U_1 + (-3U_1 - U_3 + 4U_6) \sqrt{\frac{r}{L}} + (2U_1 + 2U_3 - 4U_6) \frac{r}{L} \quad U = U_x, U_y \quad (3.25)$$

where U_1, U_3 and U_6 are the displacements at the nodes 1, 3 and 6 respectively, and L is the length of the singular element along the crack face. The stress intensity factors can now be obtained by equating the coefficients of the singular terms in equations (3.24) and (3.25):

$$K_1 = \frac{D(1-\nu^2)}{\sqrt{8L}} (-3\bar{\beta}_1 - \bar{\beta}_3 + 4\bar{\beta}_6) \quad (3.26a)$$

$$K_2 = \frac{D(1-\nu^2)}{\sqrt{8L}} (-3\bar{\alpha}_1 - \bar{\alpha}_3 + 4\bar{\alpha}_6) \quad (3.26b)$$

where $\bar{\alpha}_i$ and $\bar{\beta}_i$ denote, respectively, the rotations ψ_x and ψ_y of node i . The normalized form of the stress intensity factors are defined as

$$\bar{K}_j = \frac{|K_j|}{D\delta_1^2\sqrt{a}} \quad j = 1, 2$$

in which a is the semi crack length.

3.8 Numerical results and discussions

The method outlined in previous sections is applied to study the scattering of flexural waves by an inhomogeneity embedded in an infinite plate. Two types of inhomogeneities are considered, viz., a cavity and a crack. They are discussed below.

3.8.1 Validation of the model

The model is first validated by considering a slow flexural wave which propagates in the direction of the positive x -axis (i.e., zero angle of incidence) and incident on a circular cavity. This problem can be solved by analytical methods.

The following values of material properties are used: shear modulus $\mu=1.0$, Poisson's ratio $\nu=0.3$, and density $\rho=1.0$. The normalized form of the frequency and the radius of the cavity are defined as

$$\bar{\omega} = \frac{\omega}{\omega_0} ; \quad \bar{a} = \frac{a}{h} \quad (3.27)$$

where a is the radius of the cavity, h is the plate thickness, ω_0 is the normalization frequency as defined by equation (3.7). The factor \bar{a} may also be thought of as a reciprocal of the thickness for a fixed a . It may be noted that the frequency used for normalization is the lowest cut-off circular frequency of the simple thickness shear mode of a plate based on the three-dimensional theory.

Mindlin's theory for plate is in excellent agreement with the three-dimensional theory for normalized frequencies ranging from zero to a value slightly higher than 1.0. At the frequency $\bar{\omega}=1.0$, completely different sets of potentials and wave functions are required to represent the exterior region because of the vanishing wave numbers. Our attention is, therefore, limited to normalized frequencies below 1.0. Three types of plate bending elements are considered for discretization, viz., the four node element, the nine node Lagrange element and the heterosis element. A mesh, however, contains only one type of element. This affords an opportunity for comparison of the performance of different types

of plate bending elements. The element stiffness is evaluated by selectively integrating the bending and shear terms. Unless stated otherwise, the consistent form of the mass matrix is used. The order of integration used to evaluate the elements of this matrix is the same as that used to evaluate the bending terms. The results of extensive numerical experiments indicate that the nine node Lagrange element and the heterosis element exhibit a high level of accuracy and very often, these results hardly differed. Results of four node element are less accurate than those of other elements but the accuracy improved with mesh refinements. As an illustration, a displacement component computed along the circumference of the cavity is shown in figure 3.7. The results of the nine node Lagrange element are not shown as they are almost identical to those of the heterosis element.

A quantity of general interest in problems involving a cavity is the hoop stress along the circumference of the cavity which translates into tangential moment M_T in the present case. The moment concentration factor is now defined as

$$\bar{M}_T = \frac{M_T}{M_0}; \quad M_0 = -D\delta_1^2(\sigma_1 - 1).$$

The accuracy of a stress or a stress resultant evaluated by using the finite element technique at points other than certain Gauss points is less than optimum. The moments are, therefore, computed at the optimum Gauss points that correspond to the shear quadrature. Figure 3.8 shows the moment intensity factors so calculated along with the analytical results. These Gauss points lie on a circle of radius $1.108\bar{a}$. The results of the nine node Lagrange elements are not shown again as its plot symbols tended to overlap with those of heterosis element. It is seen from figures 3.7 and 3.8 that the accuracy of the model, when the nine node Lagrange and heterosis elements are used, is extremely good. When four node elements are used, the accuracy can be improved upon with a more refined finite element mesh. This completes the validation of the model.

3.8.2 Scattering by arbitrarily shaped cavities

Attention is next focussed on the scattering problem of cavities having square and triangular shapes. The radii of their circumscribing circles are all \bar{a} . The circular cavity considered previously represents a streamlined scatterer whereas the square and triangular cavities have a blunt nature. The case of multiple scattering by a pair of cavities is also considered where the radii of the cavities are \bar{a} and $\bar{a}/2$ and their centers are located at a distance $2\bar{a}$. It should be mentioned here that these problems pose no exceptional difficulties to the proposed method. On the other hand, they cannot be solved by analytical methods. In these problems the absolute values of the tangential moment M_T are evaluated at the Gauss points located close to the circumference of the cavities. For the square they are on a square with circumscribing circle of radius $1.07\bar{a}$, for the triangle these are on a similar triangle with circumscribing circle of radius $1.08\bar{a}$, and for the two circles the results are around the bigger circle at Gauss points on a concentric circle of radius $1.025\bar{a}$. The absolute values of M_T are then plotted against the polar angle measured at the origin from the positive x -axis in the counterclockwise direction. Only the heterosis element is used for triangular and square cavities. In the case of multiple scattering problem, the finite element model of the interior region tended to be so large that it placed a severe burden on the storage capacity of the computer. Since the band width of the four node element is about half of the nine node element, we could alleviate the storage problem by using the four node elements. Also the results are presented only for the larger circle in this case.

Figure 3.9 shows the effect of various values of \bar{a} on the tangential moment. With increasing \bar{a} more and more wave functions are needed to achieve convergence and the fineness of the mesh must be increased accordingly. In this and other subsequent figures we include the results of a circular cavity to facilitate comparison with the results of other cavities. It is seen from figure 3.9 that the maximum values occur for the least value of \bar{a} . The higher order wave functions that become active as \bar{a} increases seem to have the effect

of reducing the maximum value but, at the same time, producing more ripples. For the circular cavity, however, the ripples are confined to the first quadrant. This is a *shadow* region to the incoming wave, and the cause of ripples may be partly attributed to the wave that creeps along the boundary of the cavity and disperses in the shadow region. In figure 3.9b, some ripples are observed even in the second quadrant suggesting that the presence of another cavity nearby may extend the shadow region. The corner regions in square and triangular cavities suffer, as anticipated, abrupt increase in moments.

In figure 3.10, we present the results for various normalized frequencies. The value of \bar{a} and the angle of incidence γ are fixed at 2.0 and 0° , respectively. The maximum values of the moment seem to occur for the lowest frequency.

Lastly in figure 3.11, the results are presented for angles of incidence $0^\circ, 45^\circ, 90^\circ, 135^\circ$ and 180° . The angles of incidence 135° and 180° are omitted for the circular and the square cavities as they are similar to 45° and 0° , respectively. Furthermore, different angles of incidence in the case of the circular cavity merely cause a shifting of the curves in the plot. It is seen that the maximum values of the moment for different angles incidence are more or less the same.

3.8.3 Performance of plate bending elements

In the previous sections of this chapter, no mention was made of the behaviour of plate bending elements. They usually *behave*, but a careful look at the literature reveals that one should treat the plate bending elements with great suspicion in a situation where their performance has not been documented previously. Before any further elaboration, a brief review of some of the previous relevant contributions may prove to be useful.

A great deal of work has been done to develop an accurate and robust plate bending element. In the early stages, classical plate theory was widely used as the basis. This theory demands C^1 -continuous finite element displacement functions which is very difficult

to achieve in practice. Alternative approaches based on hybrid concepts (Tong, 1970) and the discrete Kirchhoff hypothesis (Dhatt, 1969) did not gain wide acceptance. A radically different types of elements emerged from the use of Mindlin's thick plate theory and selective-reduced integration concept. In this category, the four noded isoparametric element (Hughes et al, 1977) and the nine node Lagrange element (Pugh et al, 1978) are noteworthy. The salient feature of these elements is that they require only C^0 -continuity which is easy to achieve. This and the ease of implementation in a computer code of these elements have brought them wide acceptance. However, these elements possess at least one spurious zero-energy mode. In most applications, the zero-energy modes pose no problem as the prescription of certain boundary conditions tends to suppress the mechanisms formed by them, but they occasionally act-up especially when there are few boundary conditions. The performance of these elements in static as well as free vibration problems has been well documented in the aforementioned references. Hughes and Cohen (1978) proposed what they called heterosis element. This element is free from any shortcomings of other elements by having the correct rank, and thus possessing no zero energy mode. Its performance in dynamic problems has not been reported in the literature. Rajapakse and Selvadurai (1988) studied these elements in the context of a static situation modelling the flexural interaction between an elastic plate and an elastic half space. They found that the heterosis element performed well whereas those elements possessing zero-energy modes were deficient in modelling the interaction phenomenon. In a review article, Hrabok and Hrudey (1984) provided an extensive catalogue of plate bending finite elements. In view of the large number of elements catalogued in the above reference, one may conclude that many adequate elements exist for the analysis of specific plate problems but selecting the right one may be a difficult task, as no single element is clearly superior to the rest in all cases . Moreover, the plate bending elements have never been used in the setting of flexural wave propagation. These observations clearly indicate the need to study and evaluate the performance of some of the promising elements for flexural wave scattering phenomenon.

We consider four elements for evaluation of performance: the four node element, the heterosis element, the nine node Lagrange element and the DKT element (Dhatt, 1969). The last one, which has gained some attention in recent years, is triangular and based on the discrete Kirchhoff hypothesis. It has been found to be very accurate in static and free vibration problems under thin plate situations (Batoz et al, 1980). We consider normalized frequencies from zero to 0.9 and the following values of normalized radius: 2, 10 and 40. At this stage, it is not known if any of these values represent the *thin* plate situation, but it is interesting to note that the plate being considered has an infinite span, so that the ratio of span to thickness is infinity. Such a plate would always be regarded as thin for the purpose of static analysis. One additional comment can be made regarding the boundary conditions. Recall that insufficient boundary conditions may activate the zero-energy modes. For the problem at hand, there are no boundary conditions, except the symmetry conditions, available in the finite element region. We have studied, without any difficulty in the previous section, the problem of oblique wave incidence in which case even the symmetry conditions are unavailable. This indicates that the symmetry conditions are unlikely to suppress all rigid body modes, let alone the spurious zero-energy modes. Thus the stiffness matrix $[K]$ is singular. The far field impedance matrix $[S_f]$ is, however, nonsingular by construction. The addition of both this matrix and the mass matrix $[M]$ to the stiffness matrix renders it nonsingular.

In all numerical computations, a displacement component along the circumference of a circular cavity when it is illuminated by a slow flexural wave is computed by using the aforementioned plate bending elements. In figure 3.12, the results from the hybrid scheme are shown against the analytical one. It is seen that the quadrilateral elements yield results that are in excellent agreement with the analytical ones. The DKT element performs poorly. This is not surprising because this element completely ignores the shear energy. For this reason, it should not have been considered at all as a potential candidate, but it will be noticed as we proceed that this element performs well while others fail in

what appears to be a thin plate situation.

The results for $\bar{a}=10$ are presented in figure 3.13. The DKT element still yields poor results. Amongst the quadrilateral elements, the four node element is the least accurate. It loses accuracy as \bar{a} increases. Although the results are not presented here, we noted that the accuracy of this element could be improved by using a finer mesh. The nine node Lagrange element is seen to be as accurate as the heterosis element, but a closer examination, especially in the interval $0\text{--}30^\circ$ of polar angle, would reveal that the results of the former show strong oscillation with respect to the analytical curve, whereas those of the latter follow the analytical curve smoothly. The results presented in figure 3.14 are for $\bar{a}=40$ and $\bar{\omega}=0.5$. Only the analytical results are shown. It is seen that the displacement component exhibits violent spike-like oscillations. This is not conducive for comparing the results obtained from the hybrid scheme with the analytical one. We therefore consider a smaller normalized frequency $\bar{\omega}=0.1$ for $\bar{a}=40$. The results for this case are shown in figure 3.15. It can be seen that the DKT element yields accurate results whereas completely erroneous results are obtained for other elements. Since the shear energy may be ignored, which the DKT element does, for flexural vibration of thin plates, we may conclude that the case $\bar{a}=40$ and $\bar{\omega}=0.1$ represents the *thin* plate situation. By a negative argument, we may also conclude that the other cases we considered represent the *thick* plate situation. The results shown in this figure are interesting because even the heterosis element, which has no spurious zero-energy mode, failed. However, the trend shown by the heterosis element (and to some extent by the nine node Lagrange element) indicates that it might be possible to improve the results by using a finer mesh. However, we could not pursue this because of the limitation of computer storage. One might suspect shear locking as the cause of failure of the quadrilateral elements, but the mesh used had an element aspect ratio of the order one. This means that the shear terms are not dominant over the bending terms.

In all the results presented so far, the consistent mass matrix was used. Bazant et

al. (1976) carried out a finite element analysis to study the wave diffraction by a crack. They found that the lumped mass scheme gives greater accuracy than the consistent mass matrix. Hinton et al. (1976) proposed a diagonal form of mass matrix. This is derived from the consistent mass matrix, and is more rational than the lumped mass scheme. By studying the natural frequencies of simply supported plates, they found that the accuracy of this scheme is excellent, and far better than both consistent and lumped schemes. This scheme is referred to as *special lumping scheme*. In figures 3.16–18, the results obtained from the special lumping scheme and the consistent mass scheme are shown against those obtained by analytical means. Only the heterosis element is considered for $\bar{a}=2$ and $\bar{a}=10$ and the DKT element is considered for $\bar{a}=40$. It is seen that the consistent mass scheme is more accurate than the special lumping scheme. This is more pronounced in the case of heterosis element; this could be attributed to the omission of rotatory inertia in the special lumping scheme.

3.8.4 Scattering by a crack

The hybrid model is applied to obtain the stress intensity factors K_1 and K_2 when a slow flexural wave impinges on a through-crack. In all problems reported below, the results are for the crack tip on the right in figure 3.4 and the material properties used are $\mu=1.0$, $\rho=1.0$ and $\nu=0.25$. The normalized form of frequency and crack length are defined as in equation (3.27) with a denoting the semi crack length.

A number of singularity elements have been reported in the finite element literature for solving problems in linear elastic fracture mechanics. Among them, the collapsed quadrilateral quarter-point element has been very popular, the primary reason being the ease of implementation into a standard finite element program. Indeed, there have been many studies carried out on the efficacy of this element, all of them in a static environment. In general the accuracy of the stress intensity factors obtained by using the quarter-point element depends on many factors including the size of the elements, distribution of elements

around crack tips, grading of mesh and the method used to calculate the stress intensity factor. In general the quarter point element yields good results in single mode, but is less accurate in mixed modes (Fawkes et al,1979). The case of oblique wave incidence, indeed, gives rise to a mixed mode problem. The loss of accuracy is overcome by separating the forcing function, i.e., the incident field, into a symmetric and an anti-symmetric part in the following manner:

$$\varphi_1^i = \varphi_s^i + \varphi_a^i$$

where

$$\varphi_s^i = \frac{1}{2}(\phi_1 + \phi_2), \quad \varphi_a^i = \frac{1}{2}(\phi_1 - \phi_2)$$

in which

$$\phi_1 = e^{i\delta_1(x \cos \gamma + y \sin \gamma)}$$

$$\phi_2 = e^{i\delta_1(x \cos \gamma - y \sin \gamma)}$$

The incident wave fields given by φ_s^i and φ_a^i lead to symmetric and antisymmetric motions, respectively, with respect to the x -axis. That is to say, the loadings that result from the incident wave fields φ_s^i and φ_a^i are, respectively, mode-1 and mode-2 type. Note that this has an added advantage of substantially reducing the computational effort needed.

In order to establish the validity of the numerical procedure for the calculation of stress intensity factors, we first consider the scattering problem of a pair of slow flexural waves incident obliquely to the x -axis, the angles of incidence of the pair being 45° and -45° . The stress intensity factor K_1 was computed for discrete values of the normalized semi crack length \bar{a} , the values of \bar{a} being 0.5, 1.0, 2.0 and 5.0. For $\bar{a}=0.5$ and $\bar{a}=1.0$, a relatively coarse mesh having 16 nodes on the boundary B and 92 nodes within B (figure 3.5) was used. A finer mesh was used for $\bar{a}=2.0$ and $\bar{a}=5.0$. In figure 3.19, it can be seen that the numerical results compare extremely well with the analytical solution of Sih and Chen (1977). It is of interest to note that all the curves are below the static value of 1.25.

Having established the validity of the numerical procedure, we now report the results for K_1 and K_2 over a wide frequency range $0 < \bar{\omega} < 1.0$. The incident wave is a single train

of slow flexural wave. Figure 3.20 shows the variation of the normalized stress intensity factor K_1 with $\bar{\omega}$ for two values of incident angle γ . It is seen that the values of K_1 for $\gamma = 90^\circ$ are larger than those of $\gamma = 45^\circ$. It is also seen that K_1 decreases very rapidly with frequency in both cases. Moreover, K_1 decreases with increasing \bar{a} indicating a release in the intensification of stresses in thinner plates.

Figure 3.21 depicts the variations of the stress intensity factor K_2 with $\bar{\omega}$ for different \bar{a} . Two angles of incidence are again considered. This figure brings out the differences between K_1 and K_2 . Unlike K_1 , the stress intensity factor K_2 displays an erratic behaviour. It is seen that all three factors, namely frequency, normalized semi crack length and angle of incidence have a marked influence on the behaviour of K_2 . Moreover, the release in the intensification of stresses in thinner plates that was observed for K_1 is not necessarily seen for K_2 .

Finally, the effect of the angle of incidence on the stress intensity factors is displayed in figures 3.22–23 for two values of \bar{a} . It is seen that for a given frequency, the maximum value of K_1 occurs for the angle of incidence 90° . The stress intensity factor K_2 seemingly shows a different trend. It initially increases with frequency and then decreases after attaining a peak value. The frequency at which the peak occurs seems to depend on the value of \bar{a} .

3.9 Concluding remarks

A hybrid technique combining the finite element method with the flexural wave functions has been presented to study the scattering of flexural waves by inhomogeneities in an infinite plate. The numerical results presented here agree quite well with the analytical results available. The advantage of the method is that the near field region containing all inhomogeneities can have quite arbitrary material properties. Also the multiple scattering by a cluster of scatterers can be studied without much difficulty. It is found that the maximum value of the moment concentration factor around the cavities occur at the low-

est frequency and at the lowest a/h ratio. Moreover, the maximum value of the moment concentration factor seems to be unaffected by the direction of the incident wave. In the case of scattering by a crack, the stress intensity factor has been shown to be dependent upon the wave frequency, size of crack, thickness of plate and angle of wave incidence.

The performance of three Mindlin-type plate bending elements (four node and nine node Lagrange element and heterosis element) and the DKT element to model the flexural wave scattering phenomenon has been studied. The accuracy of the heterosis element is found to be excellent for the thick plates, but poor for thin ones. On the other hand, the DKT element is highly accurate for thin plates, but poor for thick ones. It is, therefore, crucial to select the appropriate plate bending element to analyse flexural wave propagation problems. There is a delicate problem here as it is not always possible to tell beforehand if a plate is thin or thick for a given thickness and frequency. The appropriate element should, therefore, be selected on the basis of comparison with some analytical results.

The effect of two different mass schemes has also been considered. For both the DKT and heterosis elements, the consistent mass scheme gives better accuracy than the special lumping scheme. This is in contrast to the previous study (Hinton et al, 1976), where the special lumping scheme was found to be more accurate than the consistent mass scheme.

Appendix D : Flexural Wave Functions for Plate

The terms g_1, g_2, \dots appearing in equations (3.17a-c) are as follows:

$$g_1 = H_n(\delta_1 r) \quad (D.1)$$

$$g_2 = K_n(\bar{\delta}_2 r) \quad (D.2)$$

$$g_{r1} = \bar{\sigma}_1 \left[\frac{n}{r} H_n(\delta_1 r) - \delta_1 H_{n+1}(\delta_1 r) \right] \quad (D.3)$$

$$g_{r2} = \bar{\sigma}_2 \left[\frac{n}{r} K_n(\bar{\delta}_2 r) - \bar{\delta}_2 K_{n+1}(\bar{\delta}_2 r) \right] \quad (D.4)$$

$$g_{r3} = \frac{n}{r} K_n(\bar{\delta}_3 r) \quad (D.5)$$

$$g_{\theta 1} = -\bar{\sigma}_1 \frac{n}{r} H_n(\delta_1 r) \quad (D.6)$$

$$g_{\theta 2} = -\bar{\sigma}_2 \frac{n}{r} K_n(\bar{\delta}_2 r) \quad (D.7)$$

$$g_{\theta 3} = - \left[\frac{n}{r} K_n(\bar{\delta}_3 r) - \bar{\delta}_3 K_{n+1}(\bar{\delta}_3 r) \right] \quad (D.8)$$

The terms Q_{r1}, Q_{r2}, M_{r1} , etc. appearing in equations (3.18a-c) are as follows:

$$Q_{r1} = \sigma_1 \left[\frac{n}{r} H_n(\delta_1 r) - \delta_1 H_{n+1}(\delta_1 r) \right] \quad (D.9)$$

$$Q_{r2} = \sigma_2 \left[\frac{n}{r} K_n(\bar{\delta}_2 r) - \bar{\delta}_2 K_{n+1}(\bar{\delta}_2 r) \right] \quad (D.10)$$

$$Q_{r3} = \frac{n}{r} K_n(\bar{\delta}_3 r) \quad (D.11)$$

$$M_{r1} = \bar{\sigma}_1 \left\{ \left[(1-\nu) \frac{n}{r^2} (n-1) - \delta_1^2 \right] H_n(\delta_1 r) + (1-\nu) \frac{\delta_1}{r} H_{n+1}(\delta_1 r) \right\} \quad (D.12)$$

$$M_{r2} = \bar{\sigma}_2 \left\{ \left[(1-\nu) \frac{n}{r^2} (n-1) + \bar{\delta}_2^2 \right] K_n(\bar{\delta}_2 r) + (1-\nu) \frac{\bar{\delta}_2}{r} K_{n+1}(\bar{\delta}_2 r) \right\} \quad (D.13)$$

$$M_{r3} = (1-\nu) \left[\frac{n}{r^2} (n-1) K_n(\bar{\delta}_3 r) - \frac{n \bar{\delta}_3}{r} K_{n+1}(\bar{\delta}_3 r) \right] \quad (D.14)$$

$$M_{r\theta 1} = -2\bar{\sigma}_1 \left[\frac{n}{r^2} (n-1) H_n(\delta_1 r) - \frac{n \delta_1}{r} H_{n+1}(\delta_1 r) \right] \quad (D.15)$$

$$M_{r\theta 2} = -2\bar{\sigma}_2 \left[\frac{n}{r^2} (n-1) K_n(\bar{\delta}_2 r) - \frac{n \bar{\delta}_2}{r} K_{n+1}(\bar{\delta}_2 r) \right] \quad (D.16)$$

$$M_{r\theta 3} = - \left\{ \left[\frac{2n}{r^2} (n-1) + \bar{\delta}_3^2 \right] K_n(\bar{\delta}_3 r) + \frac{2 \bar{\delta}_3}{r} K_{n+1}(\bar{\delta}_3 r) \right\} \quad (D.17)$$

where

$$\bar{\sigma}_1 = \sigma_1 - 1 \quad (D.18)$$

$$\bar{\sigma}_2 = \sigma_2 - 1 \quad (D.19)$$

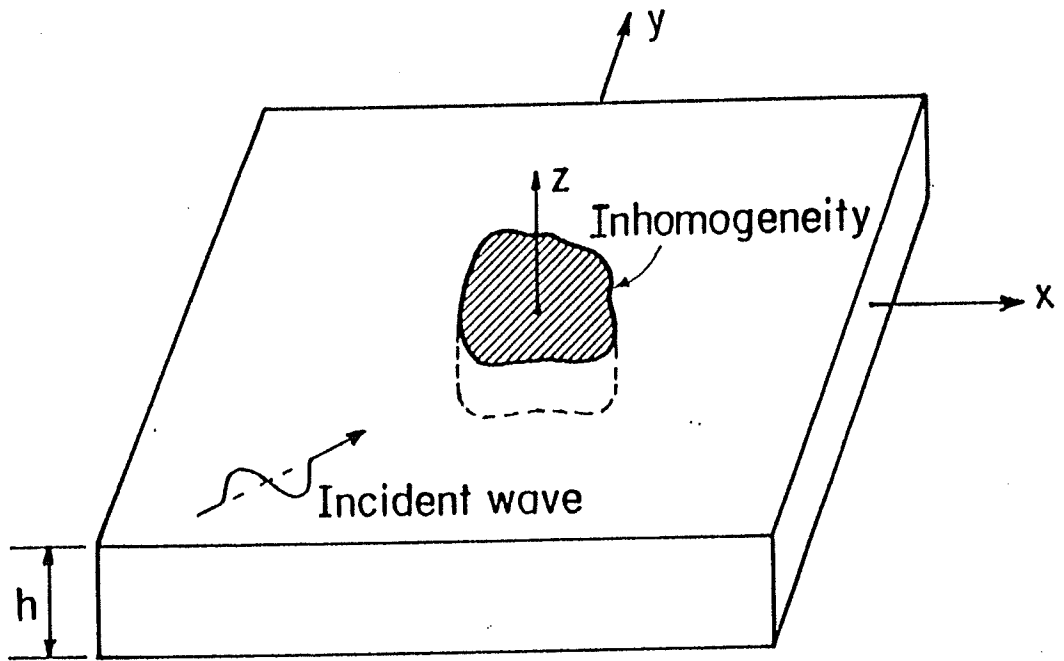


Figure 3.1 : Geometry of the problem

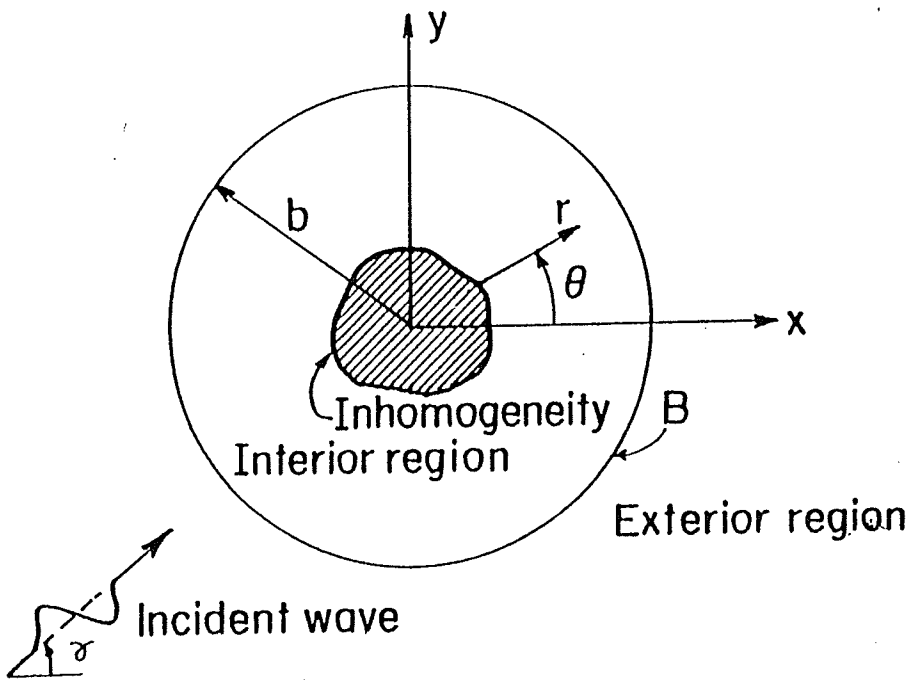


Figure 3.2 : Plan view showing mesh boundary B

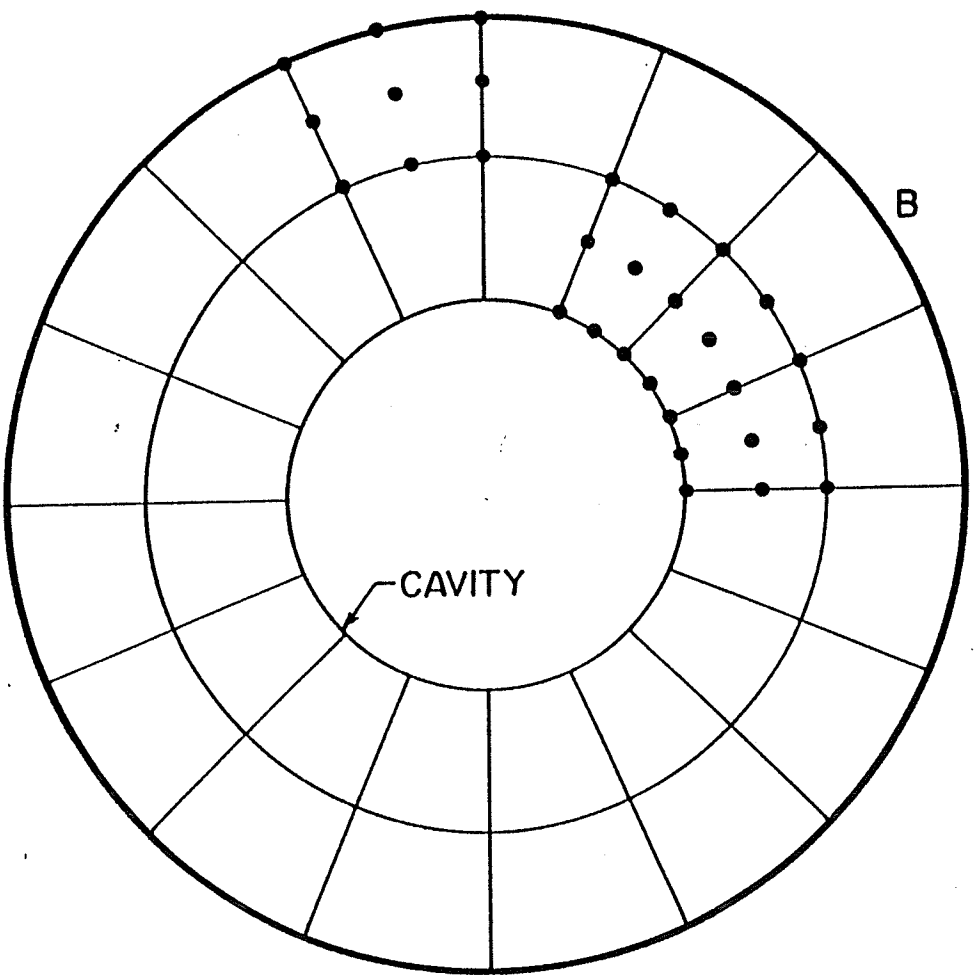
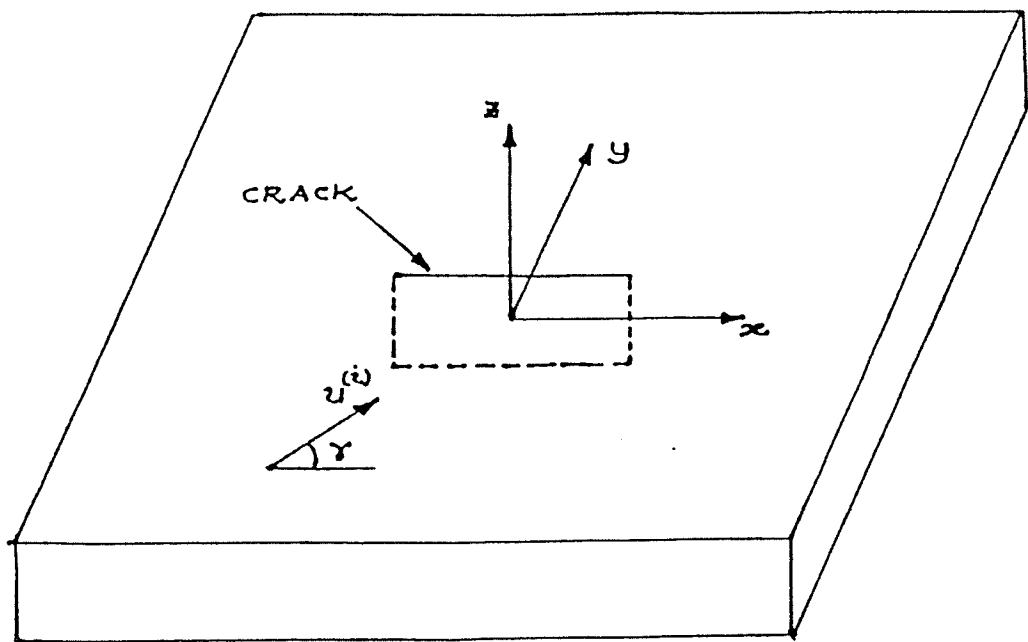
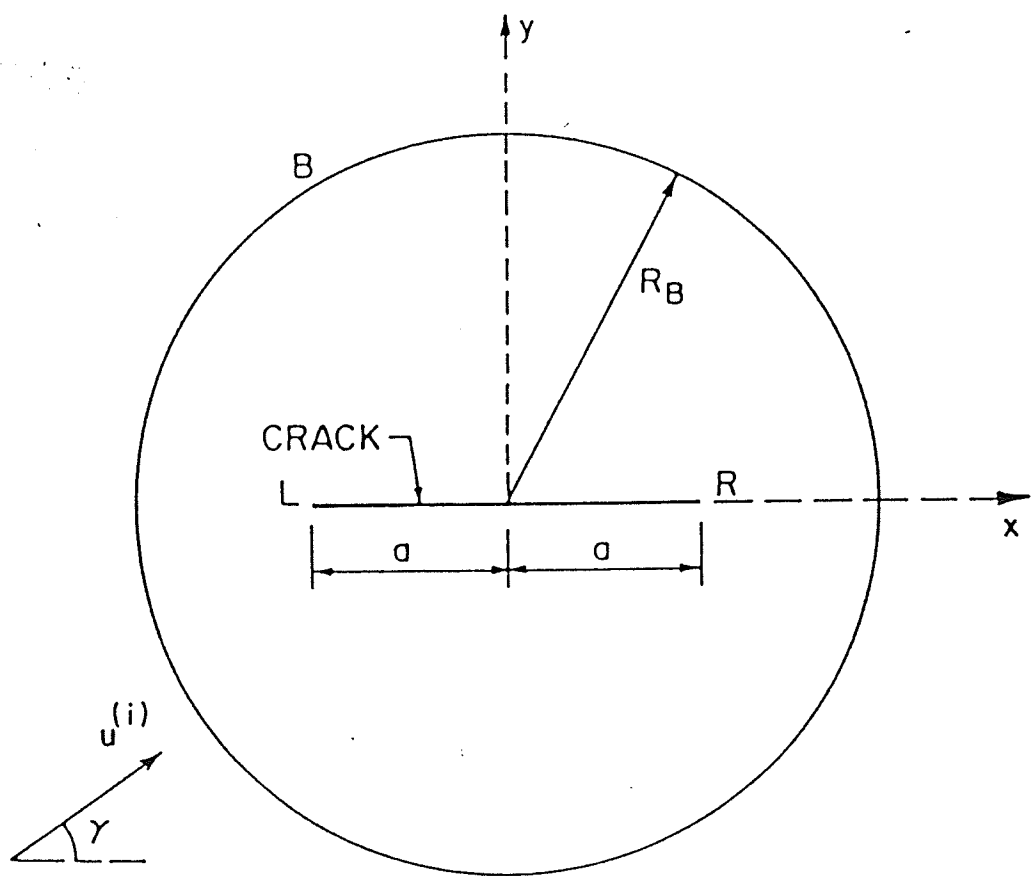


Figure 3.3 : A typical finite element model
(inhomogeneity is a circular cavity)



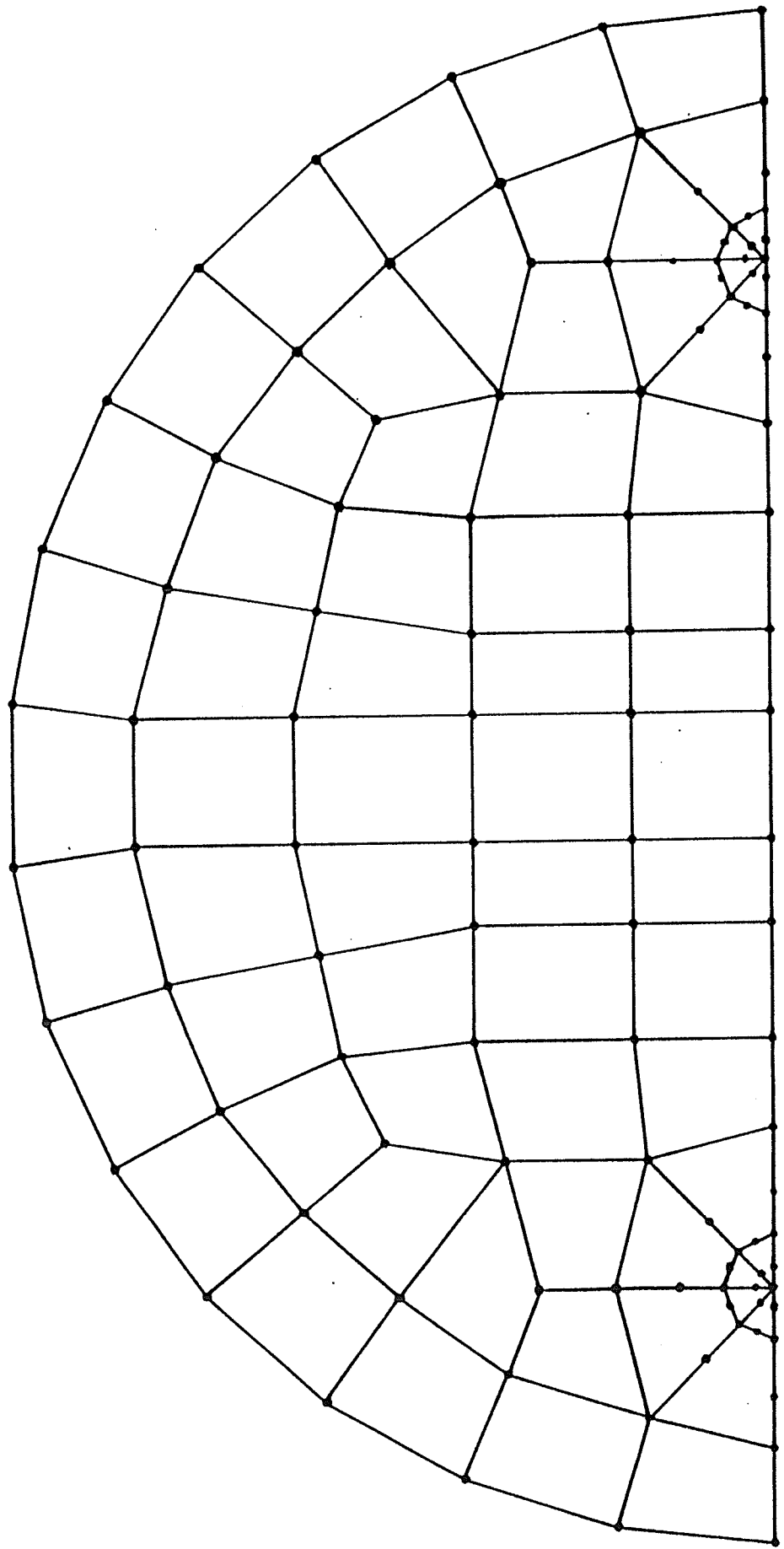
(a)



(b)

Figure 3.4 : Geometry of the crack and the hybrid model

Figure 3.5 : Finite element grid for crack in the plate



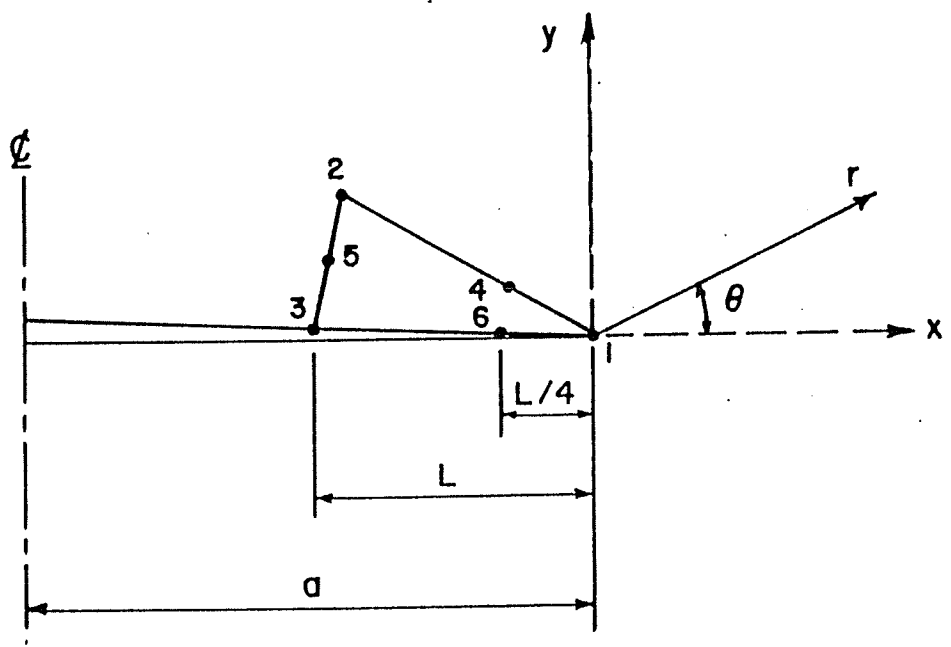


Figure 3.6 : Crack – tip element

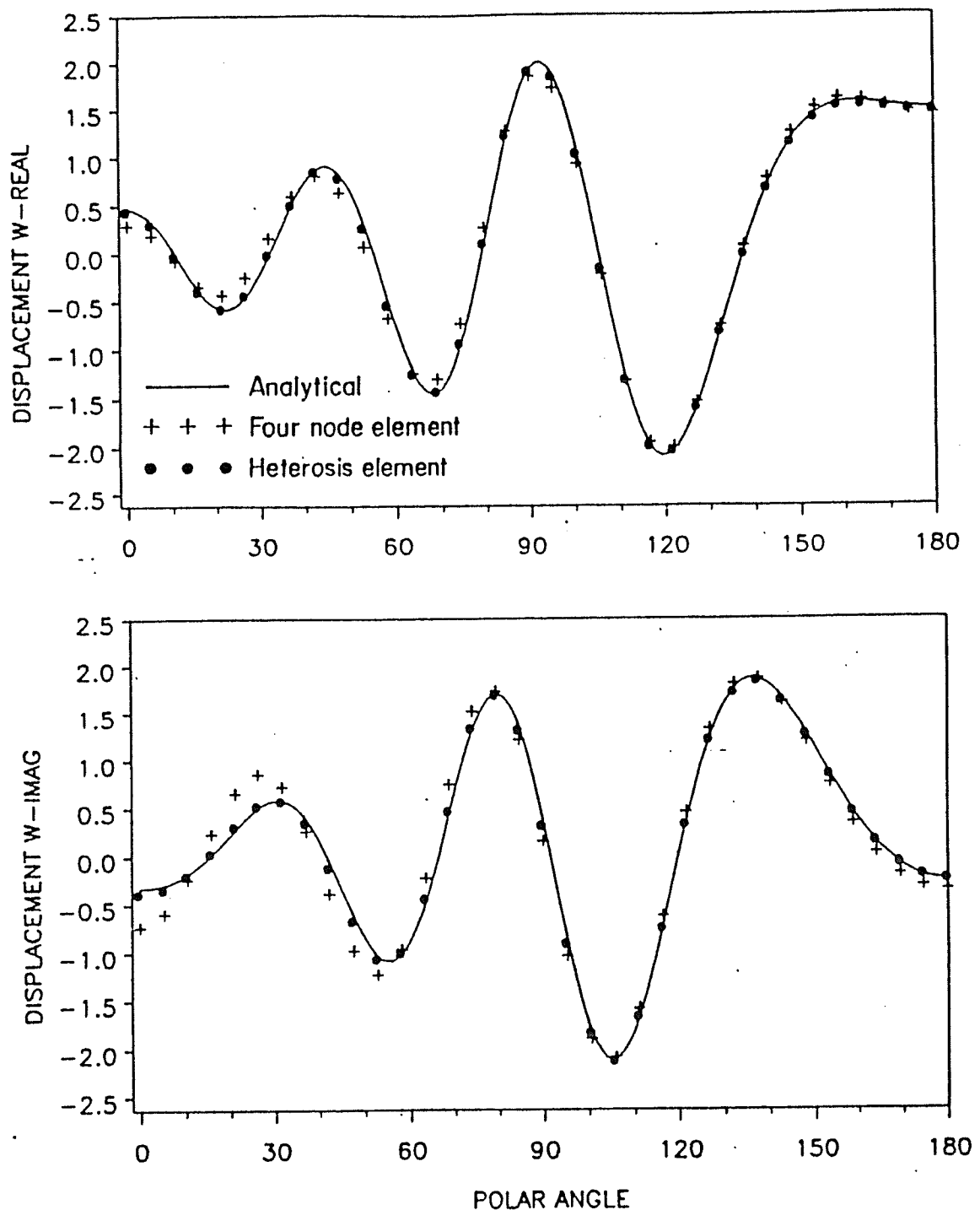


Figure 3.7 : Displacement along the circumference of the circular cavity
 $(\bar{w} = 0.9, \bar{a} = 0.5, \gamma = 0^\circ)$

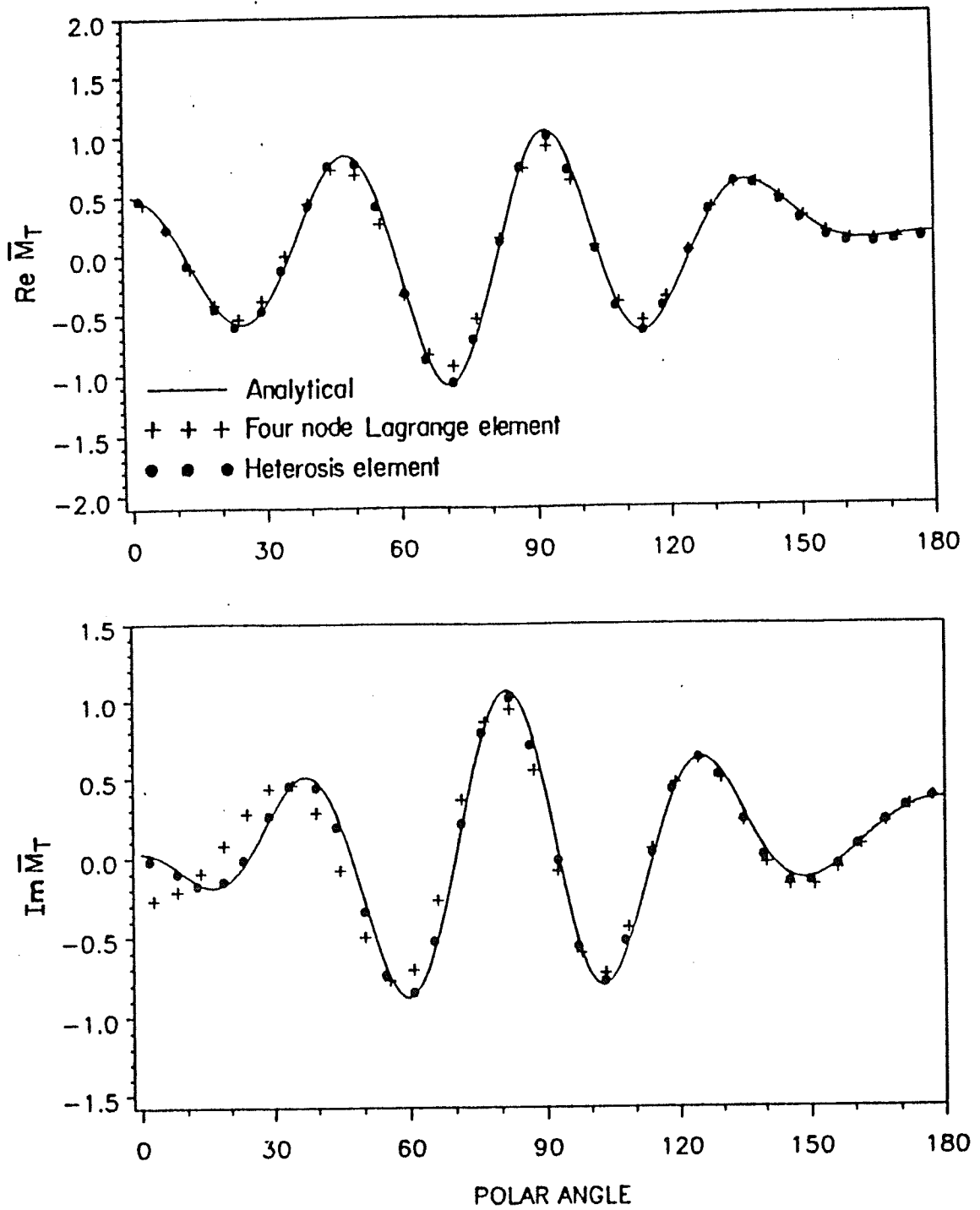
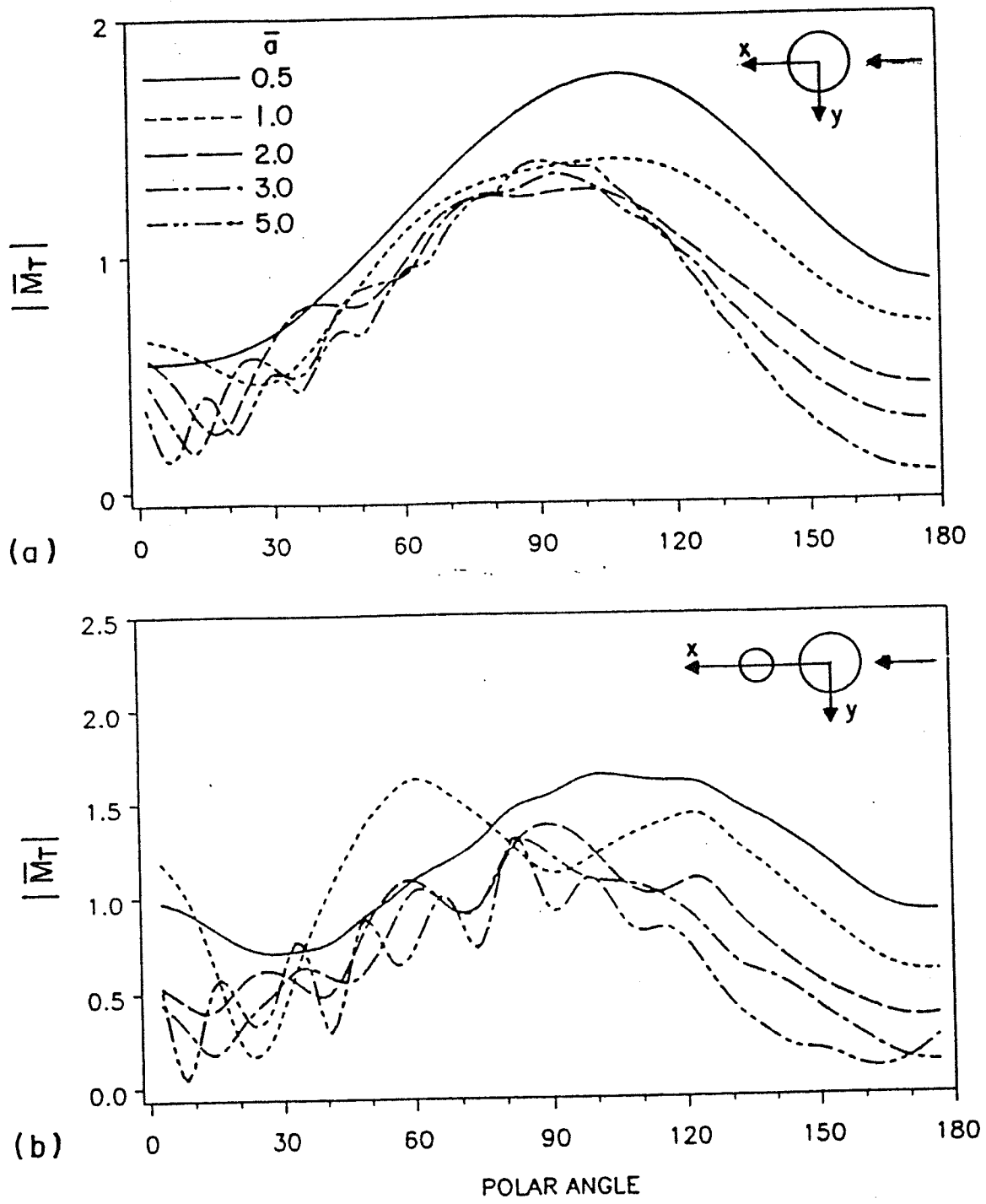


Figure 3.8 : Variation of tangential moment $(\bar{w} = 0.9, \bar{a} = 0.5, \gamma = 0^\circ)$



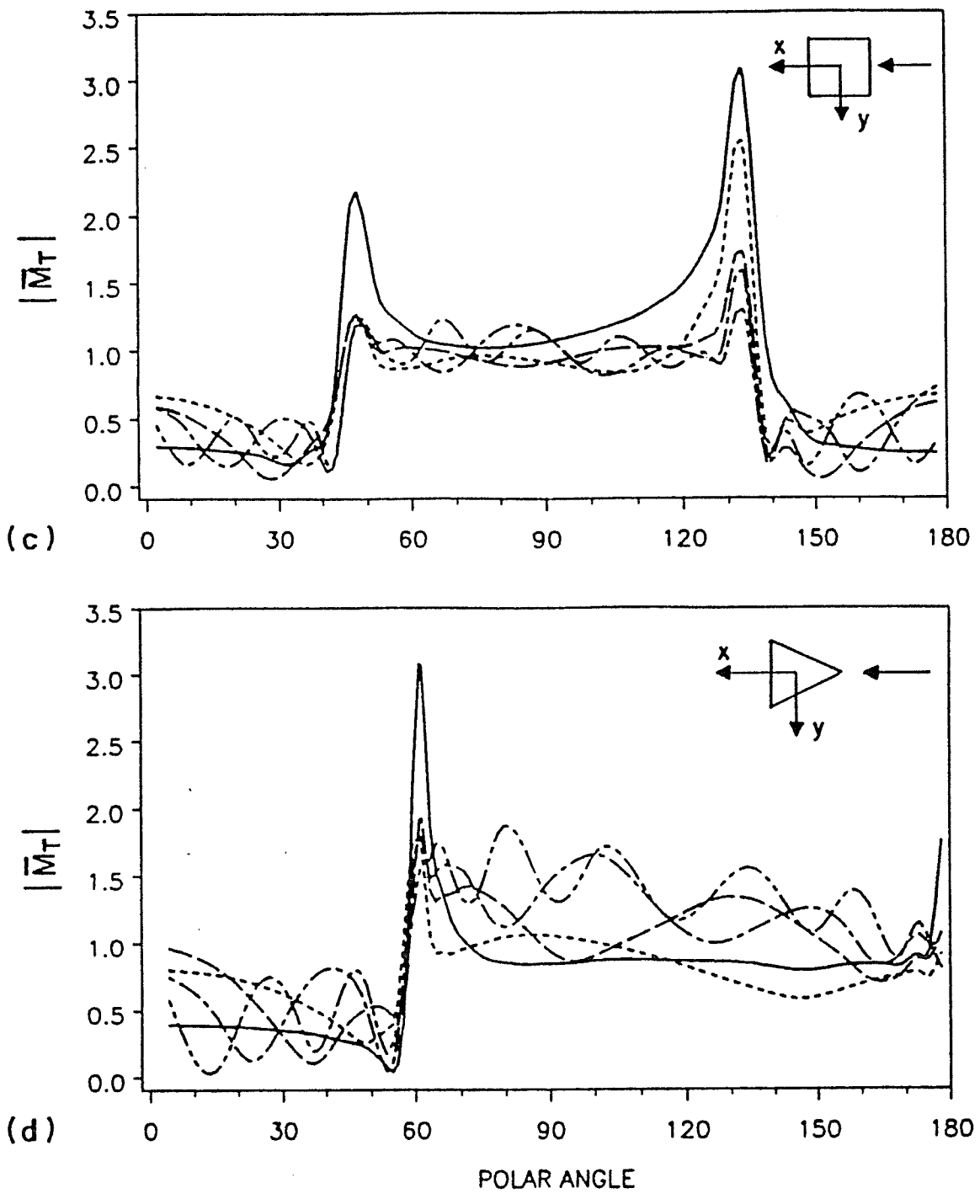
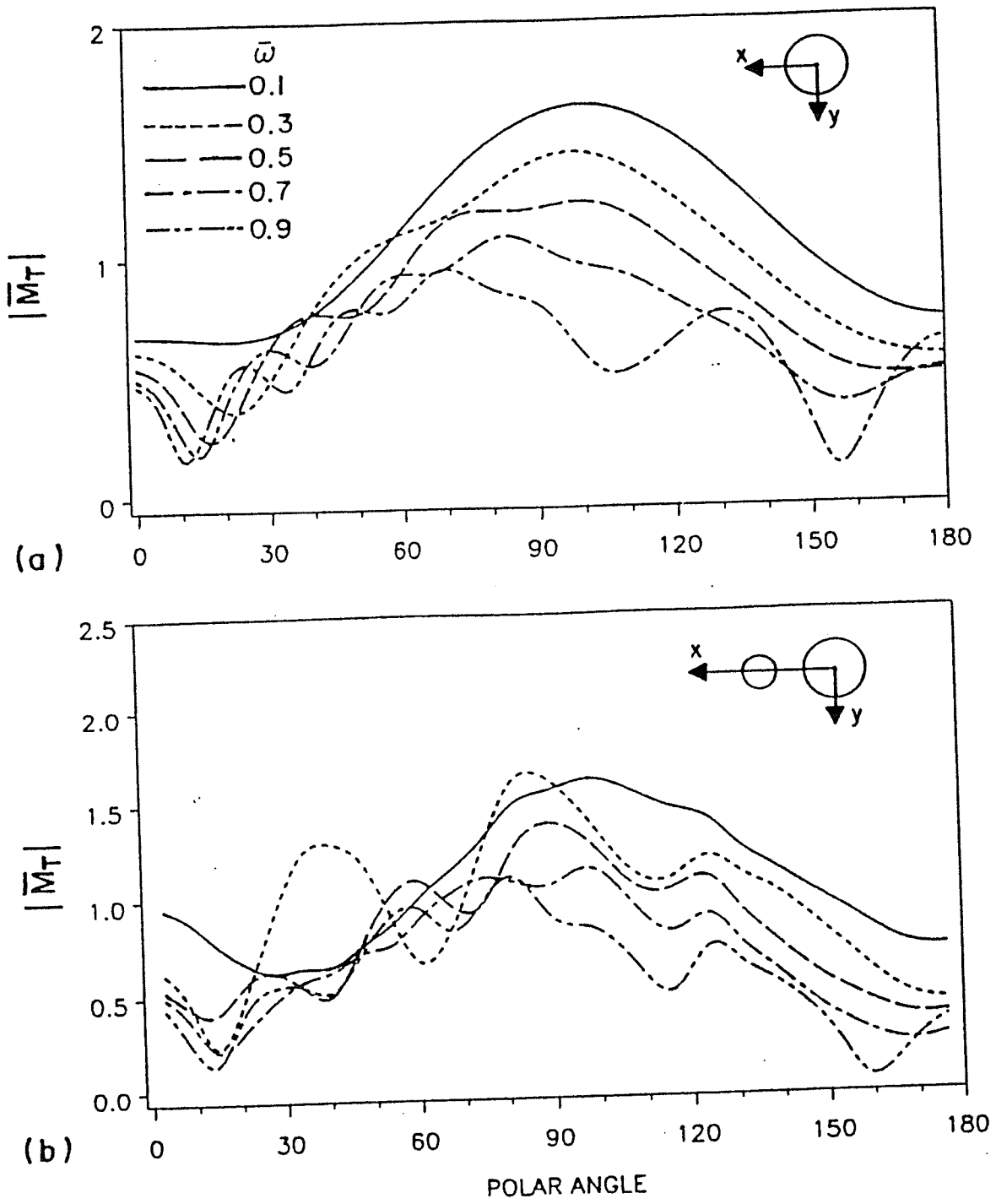


Figure 3.9 : Effect of \bar{a} on the tangential moment around cavities

$$(\bar{w} = 2.0, \gamma = 0^\circ)$$



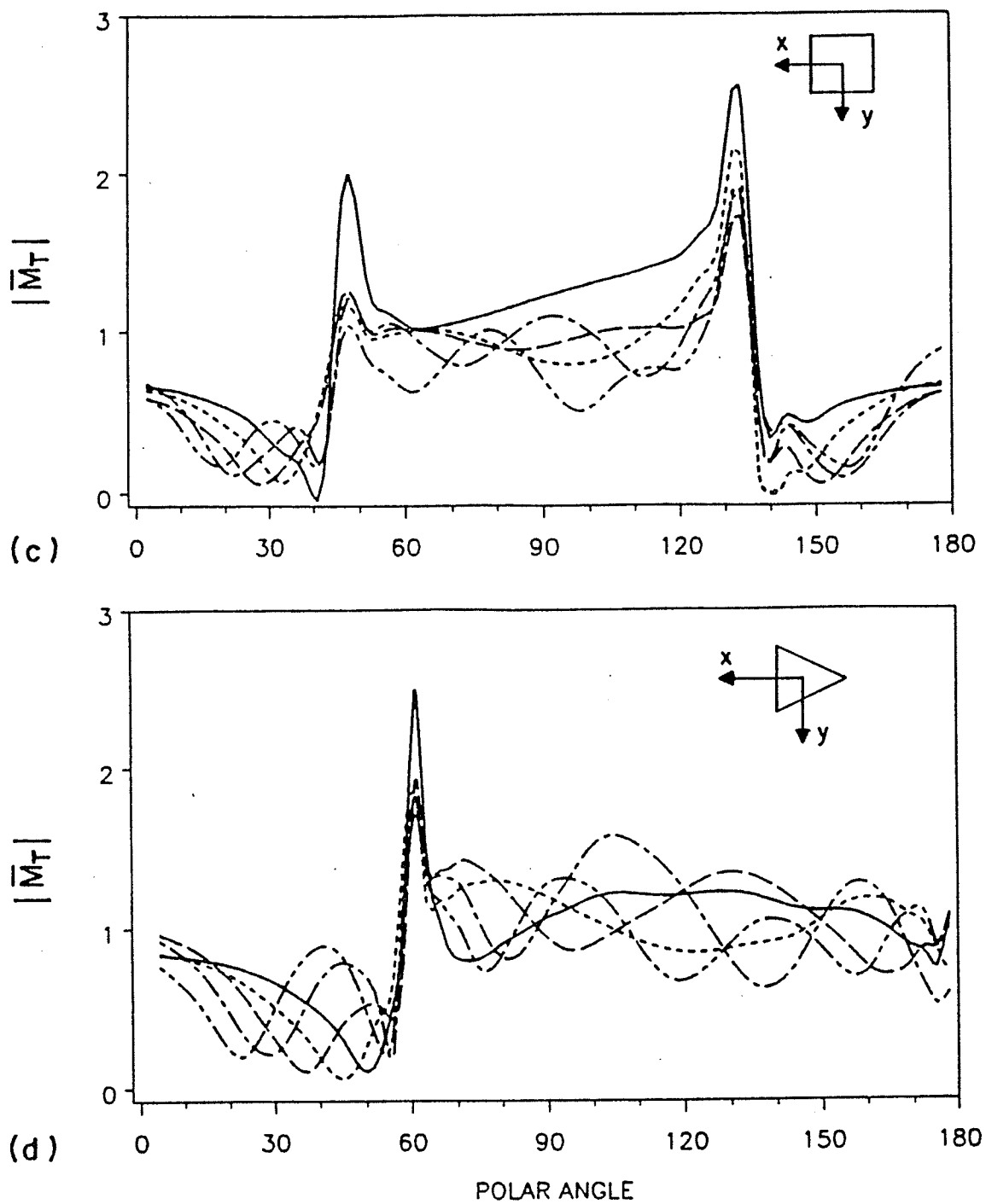
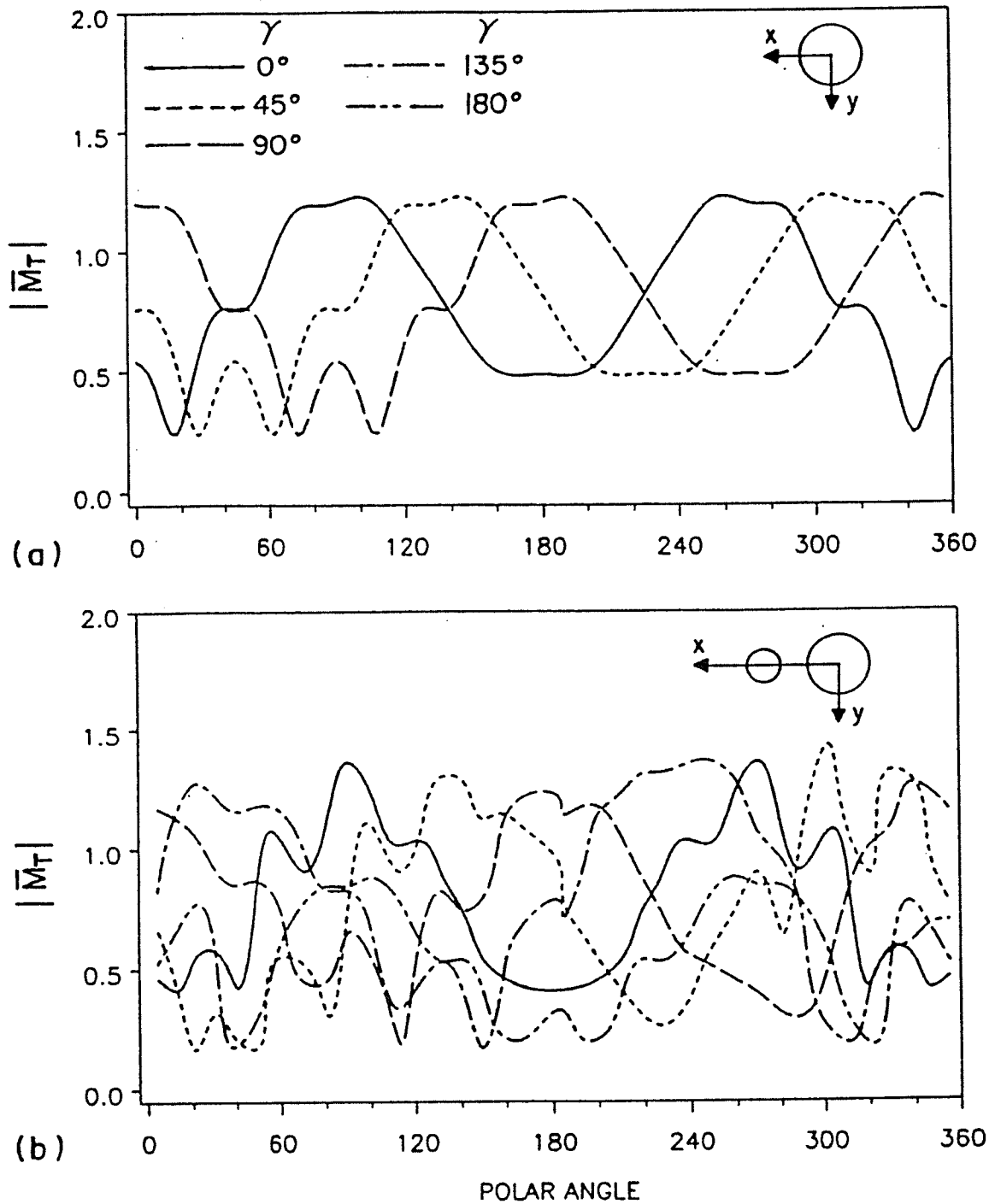


Figure 3.10 : Effect of frequencies on the tangential moment around the cavities ($\bar{a} = 2.0$, $\gamma = 0^\circ$)



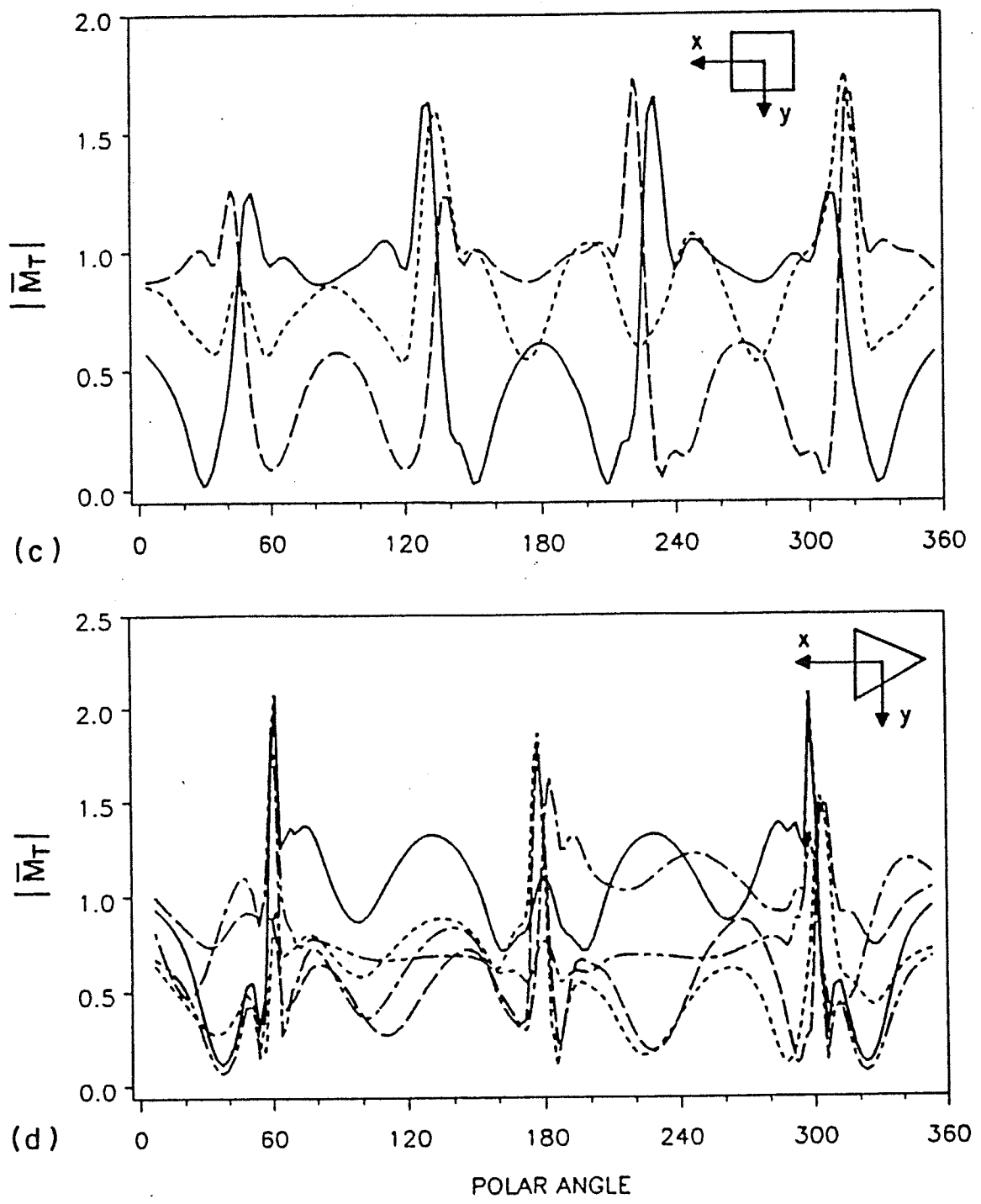


Figure 3.11 : Effect of incidence angles on the tangential moment around the cavities ($\bar{w} = 0.5$, $\bar{a} = 2.0$)

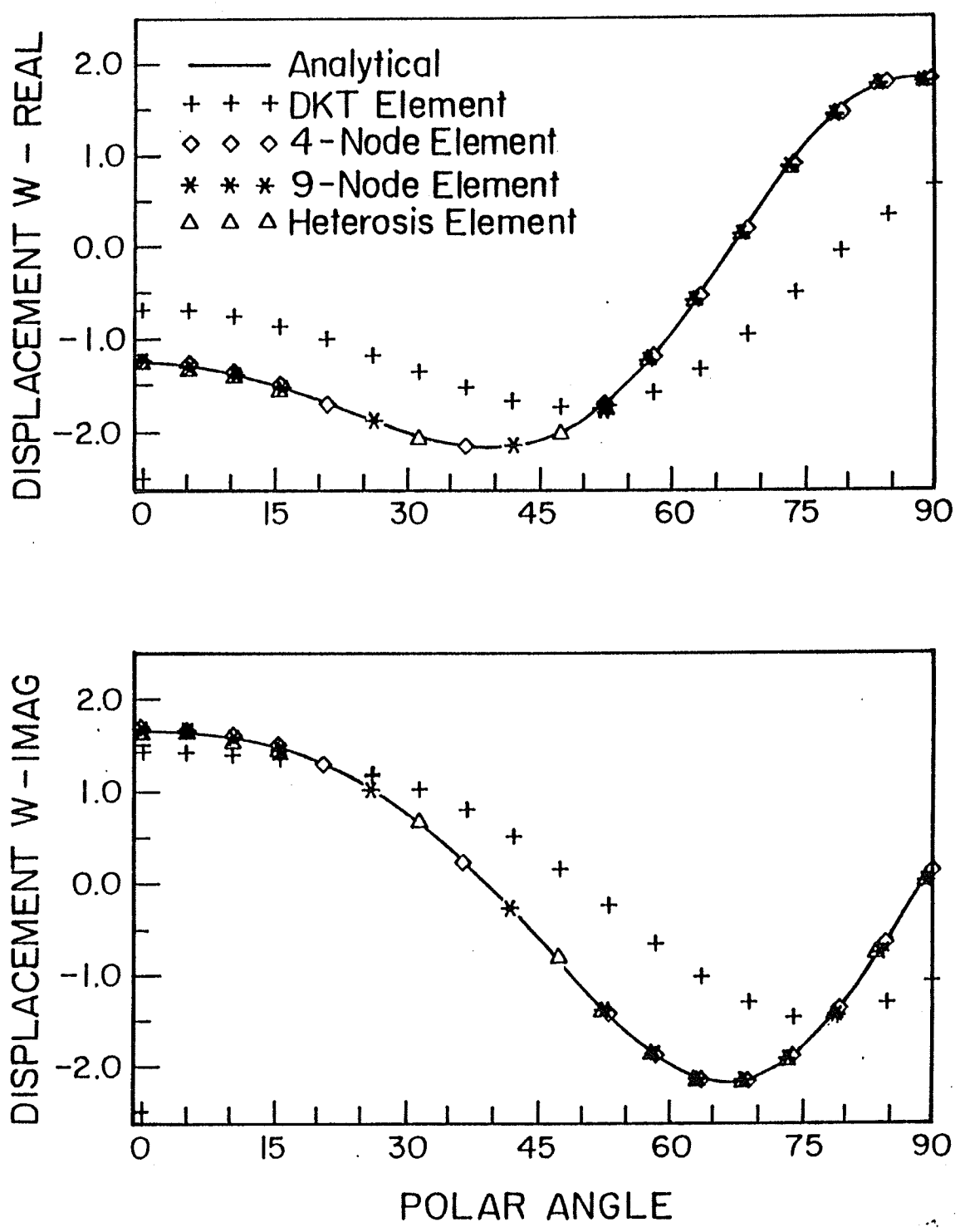


Figure 3.12 : Displacement at the circumference of the cavity for
 $\bar{a} = 2, \bar{w} = 0.5$

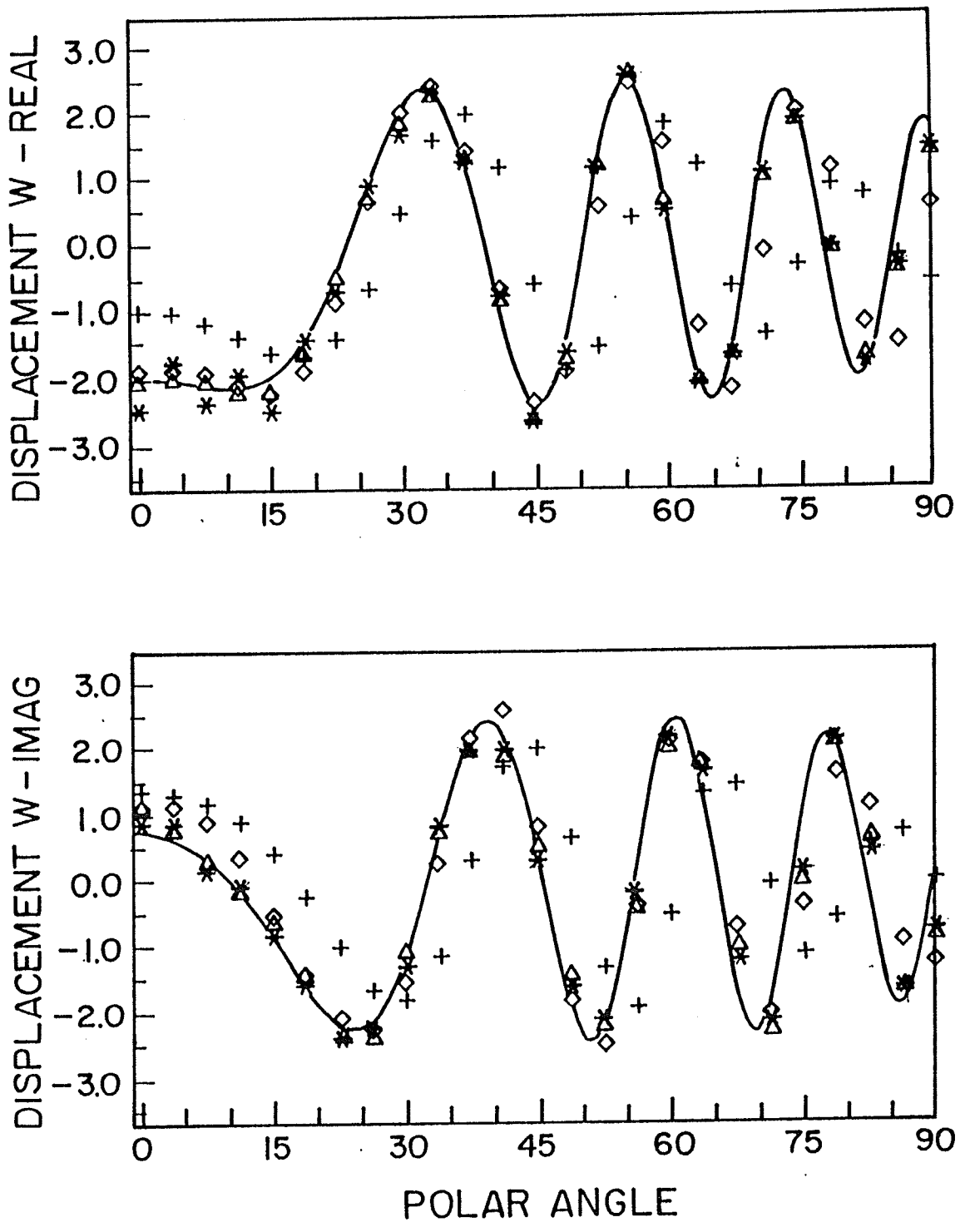


Figure 3.13 : Displacement at the circumference of the cavity for
 $\bar{a} = 10$, $\bar{w} = 0.5$

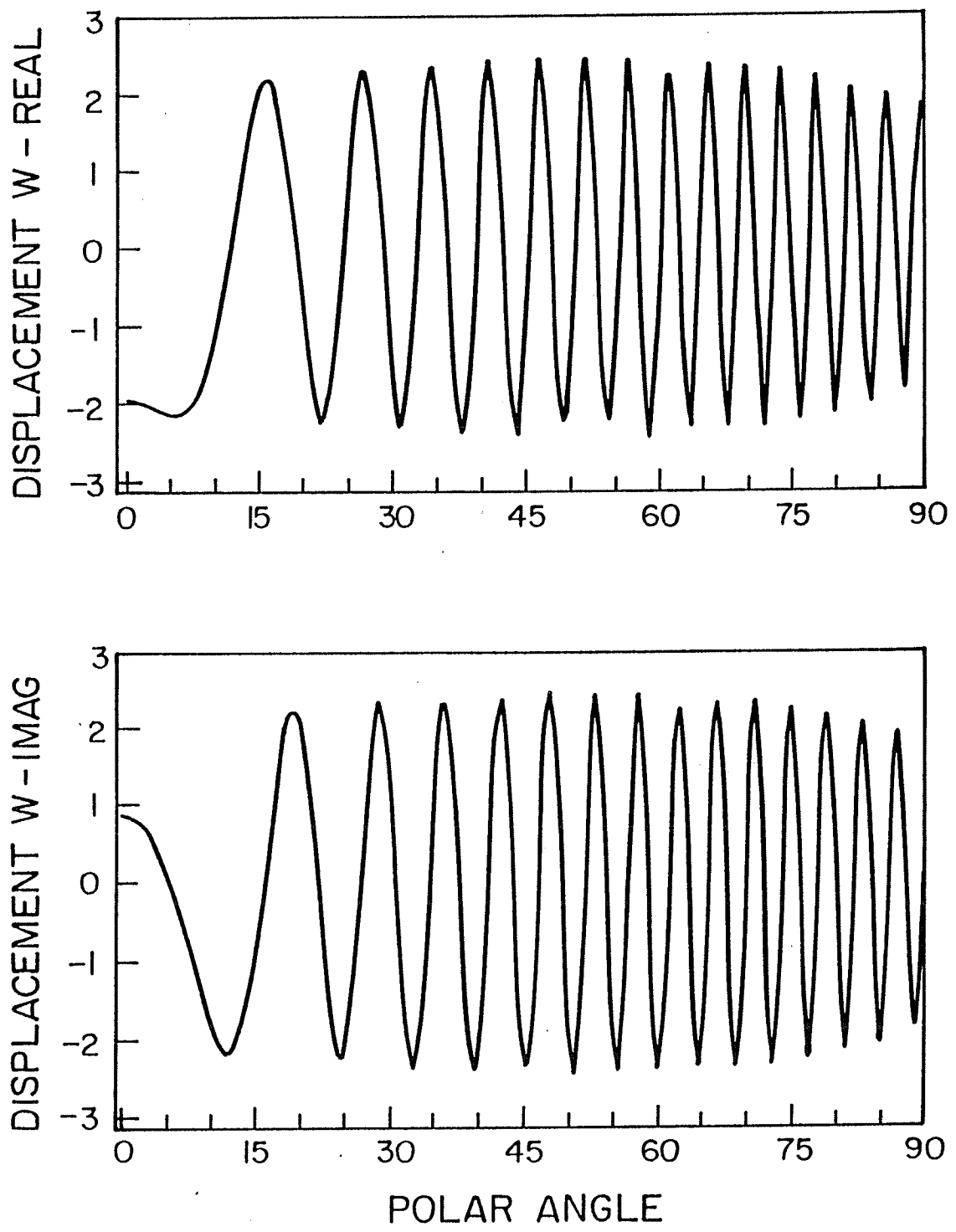


Figure 3.14 : Displacement at the circumference of the cavity for
 $\bar{a} = 40, \bar{w} = 0.5$ (analytical)

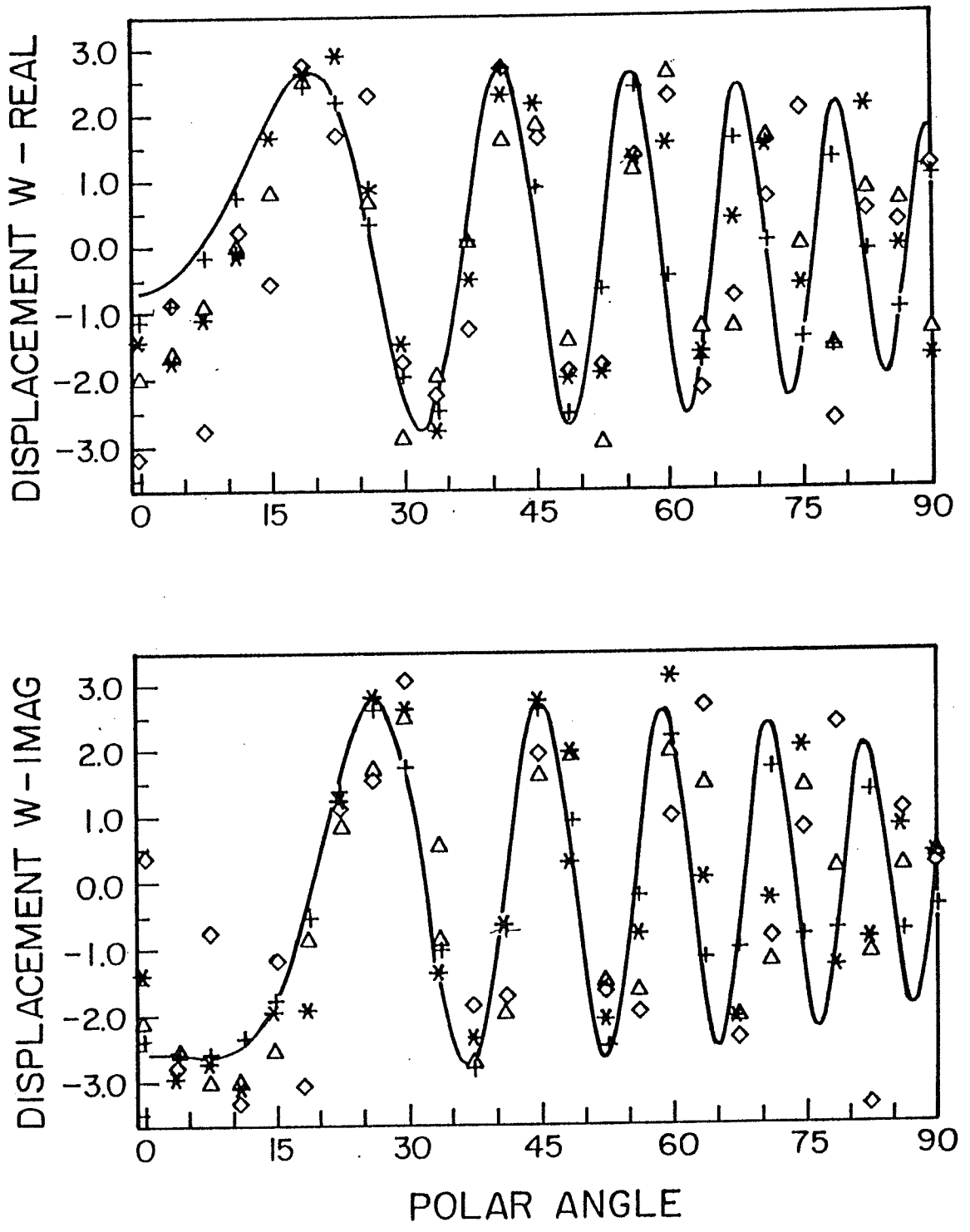


Figure 3.15 : Displacement at the circumference of the cavity for
 $\bar{a} = 40$, $\bar{w} = 0.1$

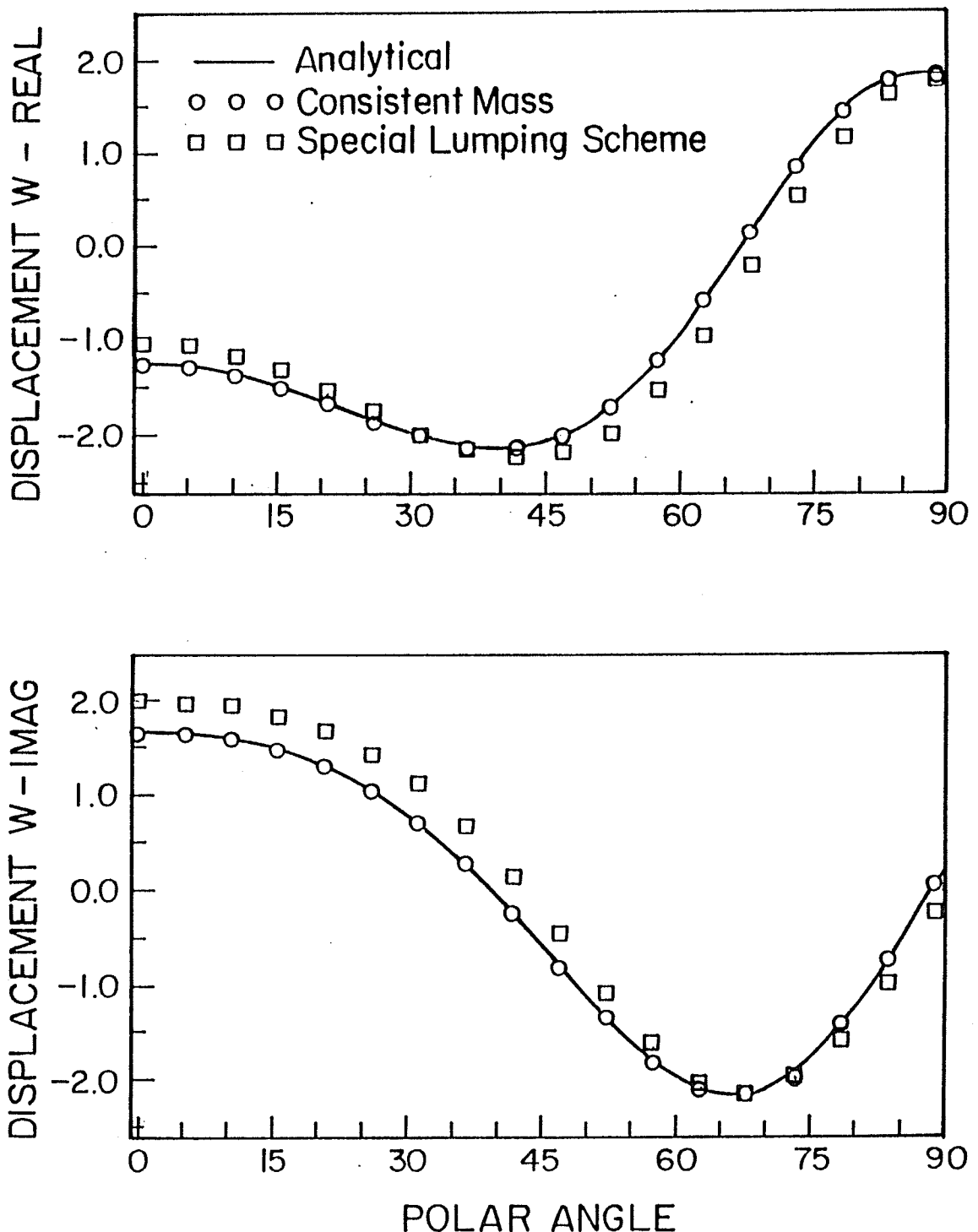


Figure 3.16 : Effect of mass schemes on the displacement for
 $\bar{a} = 2, \bar{w} = 0.5$ (heterosis element)

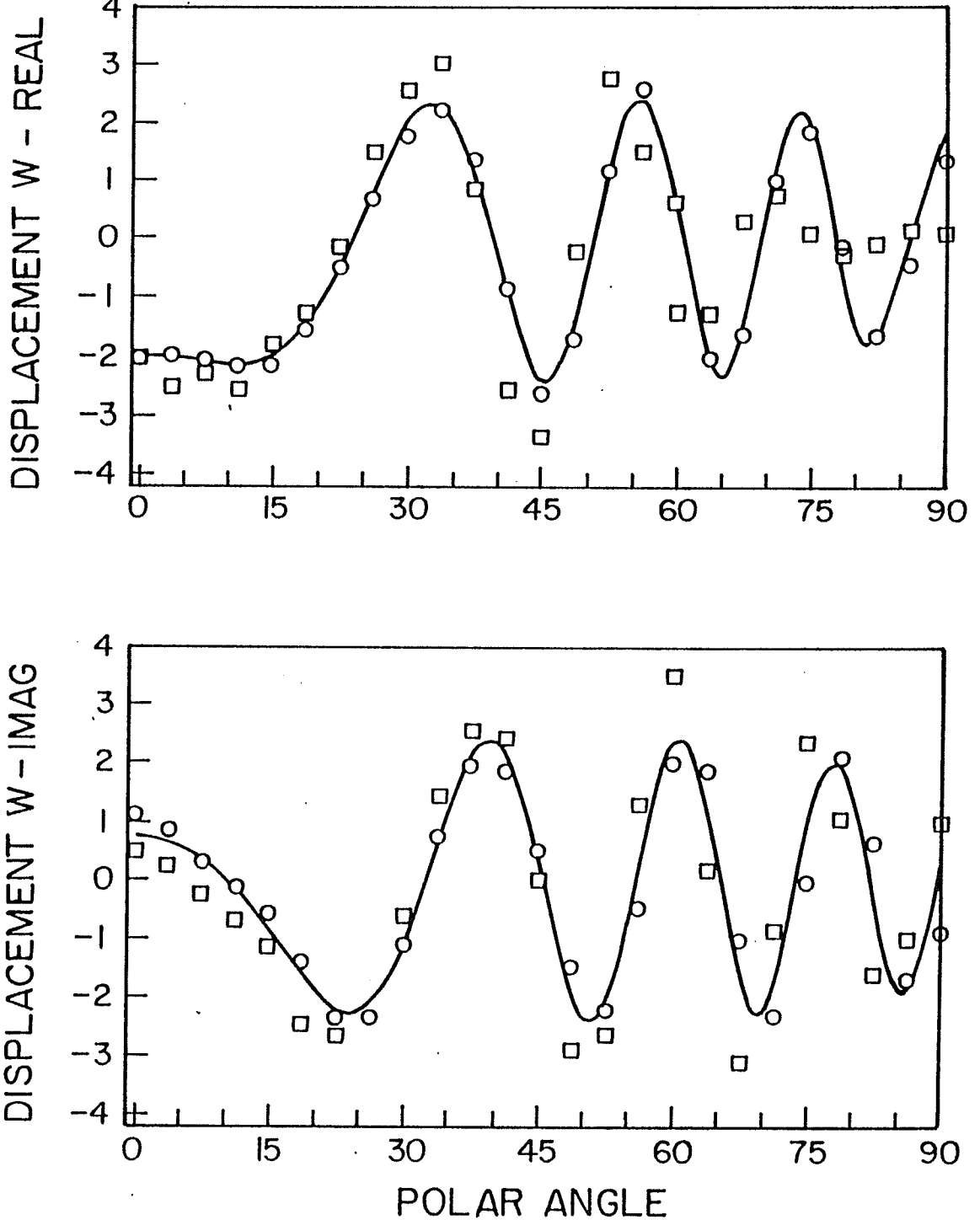


Figure 3.17 : Effect of mass schemes on the displacement for
 $\bar{a} = 10, \bar{w} = 0.5$ (heterosis element)

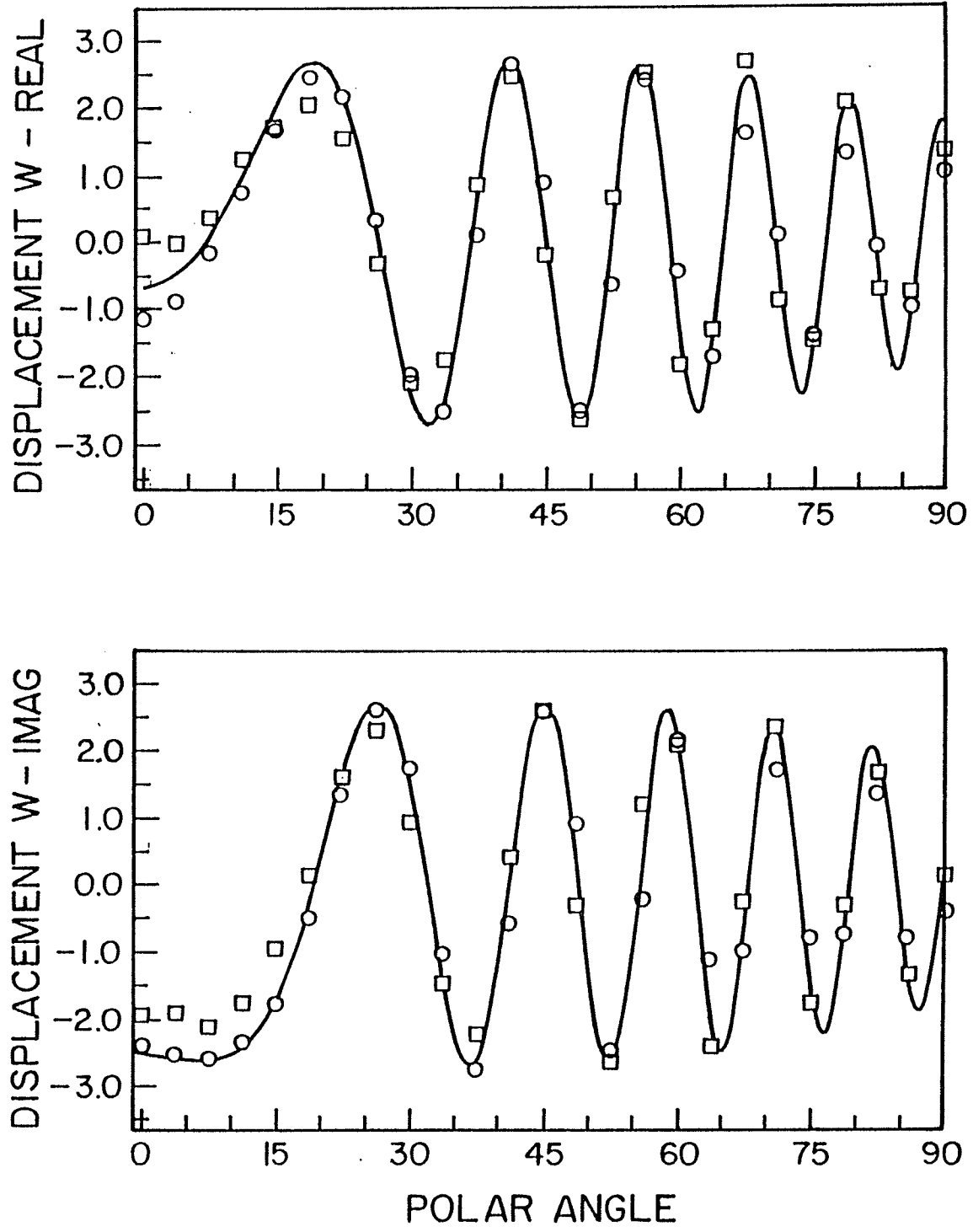


Figure 3.18 : Effect of mass schemes on the displacement for
 $\bar{a} = 40, \bar{w} = 0.1$ (DKT element)

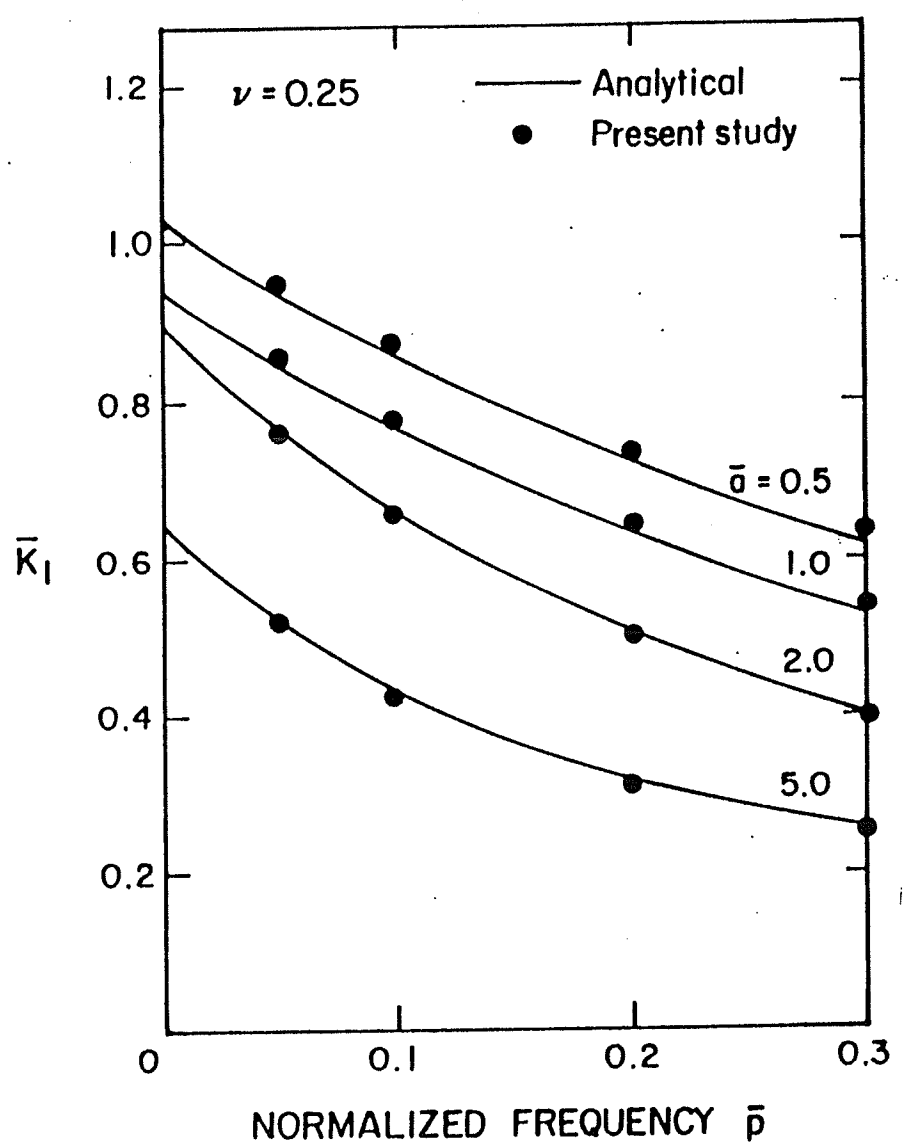


Figure 3.19 : Comparison of stress intensity factor \bar{K}_1

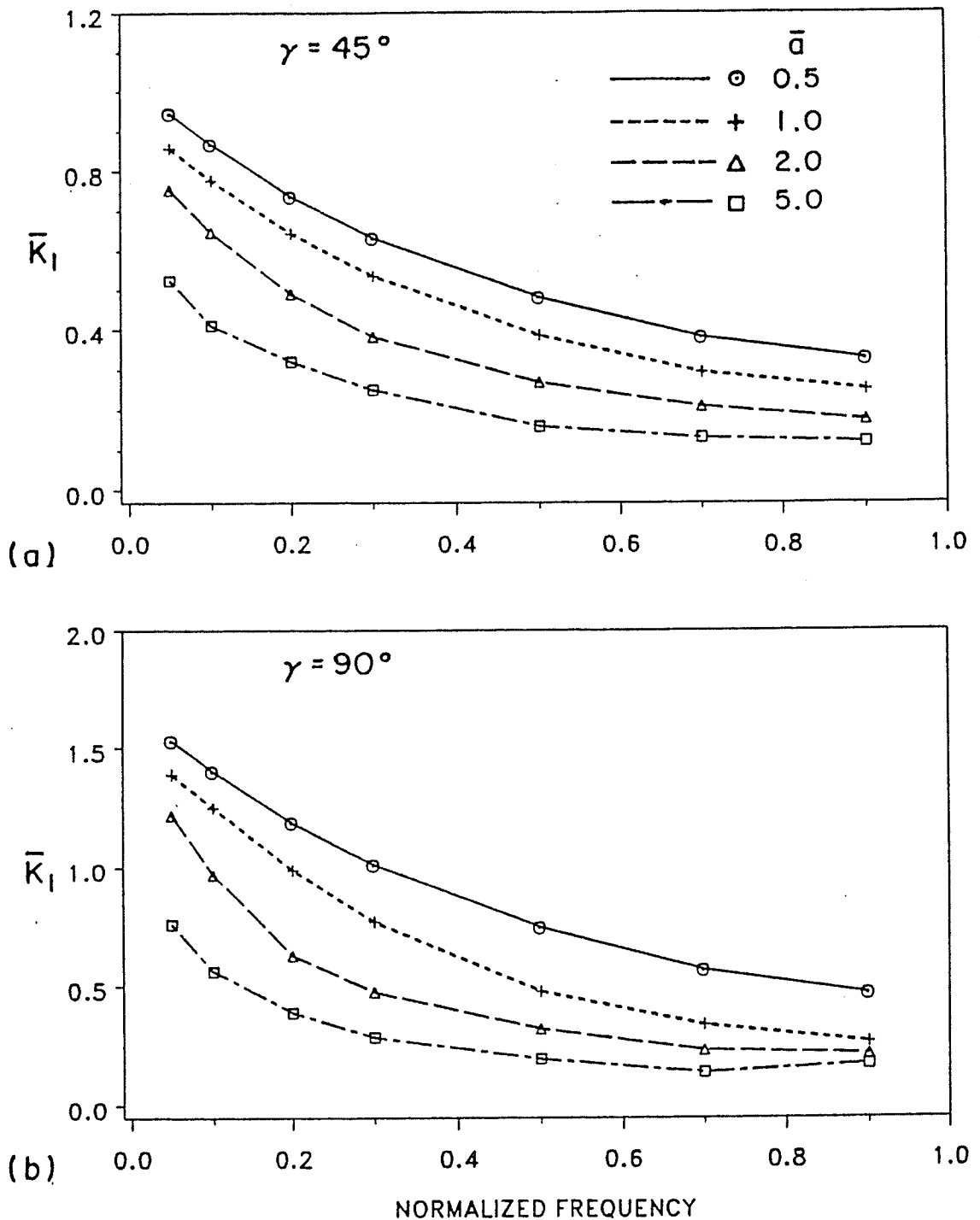


Figure 3.20 : Effect of \bar{a} on stress intensity factor \bar{K}_I

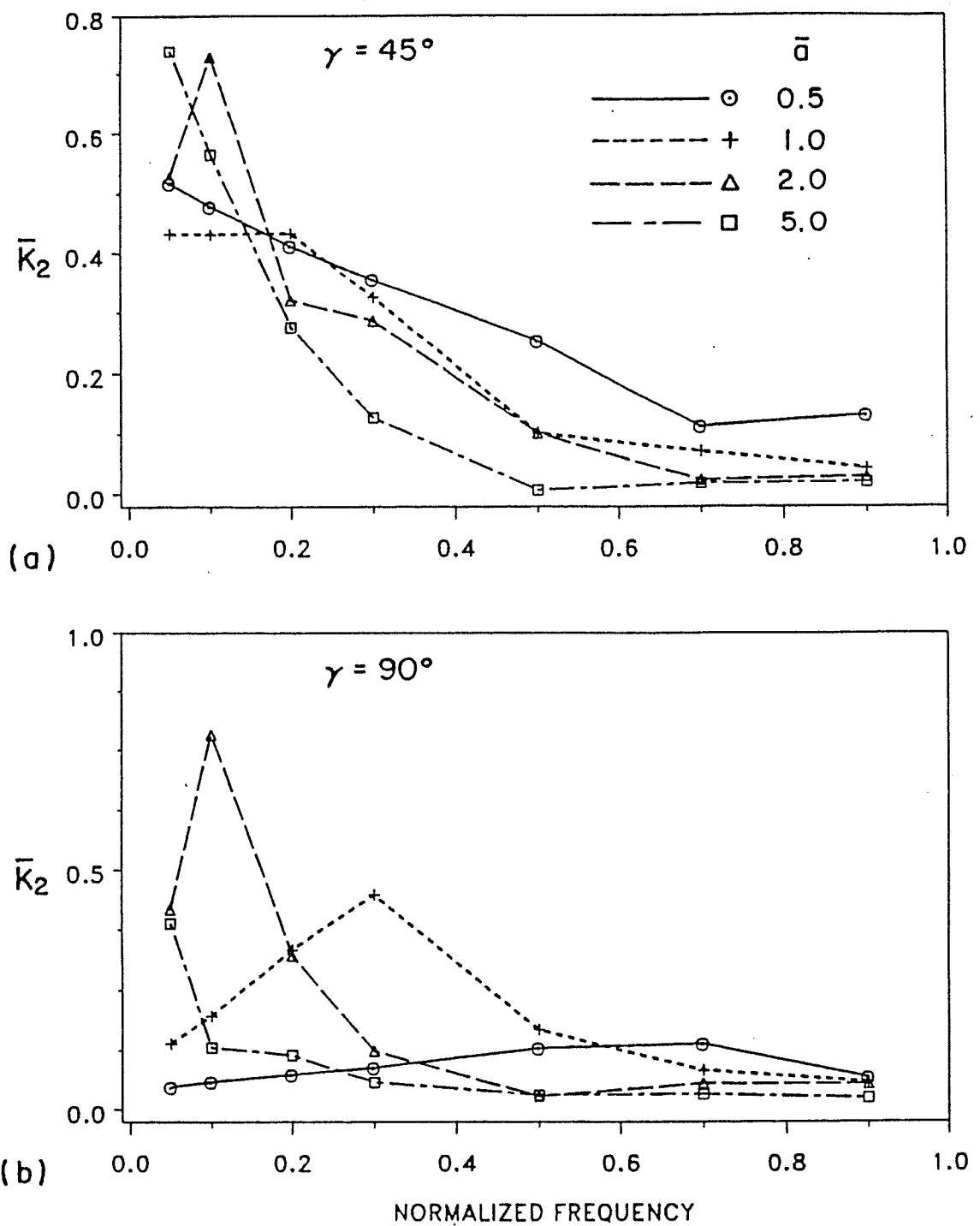


Figure 3.21 : Effect of \bar{a} on stress intensity factor \bar{K}_2

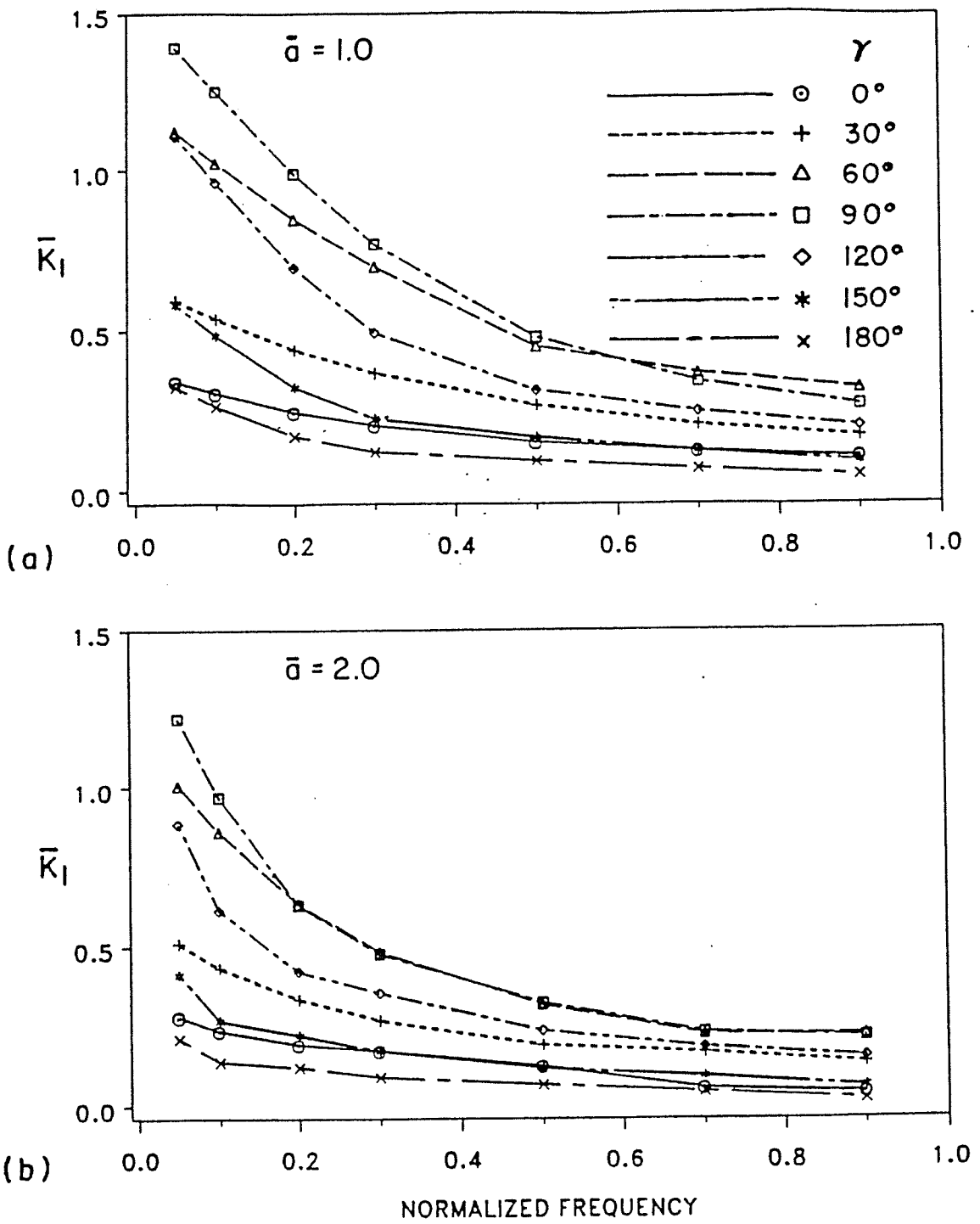


Figure 3.22 : Effect of angle of incidence on stress intensity factor \bar{K}_1

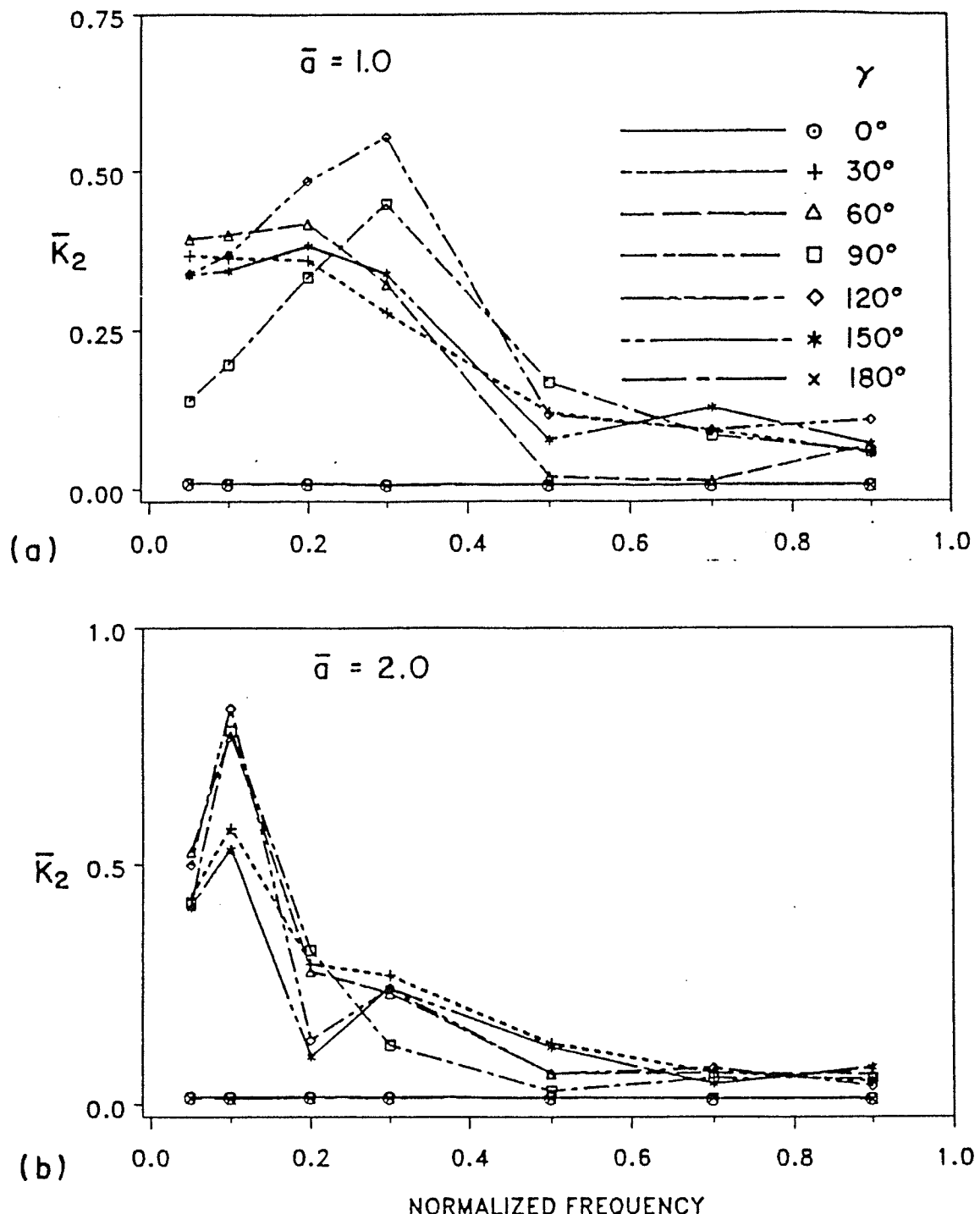


Figure 3.23 : Effect of angle of incidence on stress intensity factor \bar{K}_2

4. HYBRID MODELLING WITH BOUNDARY INTEGRAL EQUATIONS FOR HALF SPACE PROBLEM

So far, wave functions have been used to represent the far field. The modelling is fairly straightforward and could be used to study a variety of problems. *Half-space* problems, however, present difficulties. The wave functions obtained from the solution of governing equations of far-field do not satisfy traction free boundary conditions on the surface of the half space. This means that numerical treatment should be extended to the surface of the half space. A layered half space brings in additional difficulties which, at present, seems intractable with wave functions. A boundary integral representation which does not suffer from the aforementioned difficulties could be used to model the far field. This is the subject of this chapter. Note that the attention is, however, limited to a homogeneous half space. Note also that emphasis is placed on field representation and on verification of the algorithm proposed rather than its application to a variety of complicated practical problems.

4.1 Description of the problem

The geometry of the problem is depicted in figure 4.1. The surface of the half space is denoted by $z = 0$. The geometry is assumed to be axisymmetric; z -axis being the symmetry axis. Material of each domain is assumed to be homogeneous, isotropic and linearly elastic.

The system is set into motion by an incident P or SV wave propagating in a direction making an angle γ with the symmetry axis. Without loss of generality, the plane of propagation may be assumed to be the xz -plane. The resulting motion is three dimensional. For harmonic excitation (given by the factor $e^{i\omega t}$) the displacement vector \mathbf{U} must satisfy

the reduced Navier's equation

$$\mu \nabla^2 \mathbf{U} + (\lambda + \mu) \nabla \nabla \cdot \mathbf{U} + \rho \omega^2 \mathbf{U} = 0 \quad (4.1)$$

where λ and μ are Lamé constants, ρ the mass density and ω the circular frequency. For each medium the elastic constants and the mass density should be particularized. Boundary conditions are zero tractions on the surface of the half space. Perfect bonding along the interface requires continuity of displacements and tractions. In addition, the diffracted field must satisfy the elastic radiation conditions at infinity.

4.2 Hybrid model: Finite element – Boundary integral equation technique

A hybrid model combining the finite element method with a boundary integral representation is presented here that could be used to study the problem described above.

Let B , C , C_{ab} , C_{ac} , C_{bd} and C_∞ denote the contours fc , eb , ab , ac , bd and gd in figure 4.2. The surfaces of revolution generated by these contours are denoted by S_B , S_C , S_{ab} , S_{ac} , S_{bd} and S_∞ , respectively. In the above S_∞ is a hemispherical surface of very large radius; thus, it is assumed to represent the boundary at infinity. $(S_{ab} + S_{bd})$ defines the free surface of the half space. The surface S_C is so chosen that the region interior to S_C includes all the irregularities. The surface S_B is located outside S_C . Note that the surfaces S_B and S_C need not be hemispherical. We define R_I to be the finite region bounded by the surfaces S_B and S_{ac} , and R_E to be the region bounded by the surfaces S_C , S_{bd} and S_∞ . The region R_I is discretized with finite elements. A boundary integral representation is employed for the region R_E . The overlapping of two regions permits placement of source and observation points on two different contours. This precludes the singularities associated with the Green's functions when the source and observation points coincide. The evaluation of the Green's functions is very costly and time consuming and may, sometimes, require supercomputer environment. The advantage of the method resides

in the fact that the Green's functions for a given frequency has to be evaluated only once regardless of the shape of the scatterer that fits inside the contour C . This differs from the standard boundary integral equation formulation on the boundary of the inclusion for which Green's function has to be reevaluated every time a different scatterer is analysed. The present method, in its full ramifications, is quite general and can treat irregularities which may contain inhomogeneous and nonisotropic materials. Moreover, the conventional foundation problem, i.e., a foundation resting on or embedded in an elastic half space also qualifies to be solved by the proposed algorithm.

4.3 Finite element formulation of the region R_I

The domain R_I is discretized by using axisymmetric elements, formulation of which is given in Chapter 2. Recapitulating, the force and displacement components are expanded in the circumferential direction ϕ in terms of Fourier harmonics. For instance, the displacements are written as

$$U_r(r, \phi, z, t) = \sum_{m=0}^{\infty} [\bar{U}_{rm}(r, z) \cos m\phi] e^{i\omega t} \quad (4.2a)$$

$$U_z(r, \phi, z, t) = \sum_{m=0}^{\infty} [\bar{U}_{zm}(r, z) \cos m\phi] e^{i\omega t} \quad (4.2b)$$

$$U_{\phi}(r, \phi, z, t) = \sum_{m=0}^{\infty} [-\bar{U}_{\phi m}(r, z) \sin m\phi] e^{i\omega t} \quad (4.2c)$$

where the overbarred terms denote amplitudes. The time factor $e^{i\omega t}$ is suppressed in the sequel. The Fourier harmonics are uncoupled and, therefore the analysis may be carried out by considering only one harmonic at a time with the complete solution given by the summation of all harmonics considered. Thus the formulation is given only for an arbitrary harmonic number m .

In order to derive the equation of motion, the displacement field is written in the usual way in terms of the shape functions and the nodal displacements. The discretized

equation of motion, for each harmonic m , over the region R_I is found to be (see equation 2.11)

$$\begin{bmatrix} S_{II} & S_{IB} \\ S_{BI} & S_{BB} \end{bmatrix} \begin{Bmatrix} \bar{q}_I \\ \bar{q}_B \end{Bmatrix} = \begin{Bmatrix} 0 \\ \bar{P}_B \end{Bmatrix} \quad (4.3)$$

where S_{IJ} represent the impedance matrices, \bar{q}_I and \bar{q}_B the interior and boundary nodal displacements, respectively, and \bar{P}_B the boundary nodal forces. The overbar is understood to stand for amplitudes. For our purpose, only a relationship between the inside nodal displacements and the boundary ones is needed which is given by

$$\{\bar{q}_I\} = -[S_{IC}]\{\bar{q}_B\} \quad (4.4a)$$

where

$$[S_{IC}] = [S_{II}]^{-1}[S_{IB}]. \quad (4.4b)$$

4.4 Boundary integral representation of the region R_E

A boundary integral representation for the scattered field in the region R_E is derived from the elastodynamic reciprocity theorem (Achenbach, 1973) which may be written using tensor notation in the following form:

$$\int_V (f_j^A U_j^B - f_j^B U_j^A) dV = \oint_S (U_j^A T_{jk}^B - U_j^B T_{jk}^A) n_k dS \quad j, k = r, \phi, z \quad (4.5)$$

where U_j^A and T_{jk}^A represent the displacements and stresses caused by body forces f_j^A while U_j^B and T_{jk}^B are the displacements and stresses caused by body forces f_j^B , in a volume V bounded by a surface S . Einstein summation convention of repeated indices is understood. We first apply equation (4.4) to the region R_E . The A field is taken to be the scattered field U_j^s and the B field the Green's displacements G_{ij} . The scattered field has no sources in this domain since the inhomogeneities lie outside the domain under consideration, hence $f_j^A = 0$. For Green's sources located inside R_E , we obtain

$$-U_i^s = \oint_S (U_j^s \Sigma_{ijk} - G_{ij} \sigma_{jk}^s) n_k dS \quad i, j, k = r, \phi, z \quad (4.6)$$

where n_k is the normal vector on the surface S directed outward as shown in figure 4.2, S indicates the closed surface formed by the surfaces S_C , S_{bd} and S_∞ and the half space Green's tensors $G_{ij}(\mathbf{x}, \mathbf{x}')$ and $\Sigma_{ijk}(\mathbf{x}, \mathbf{x}')$ represent, respectively, the j th component of the displacement vector and the jk th component of the stress tensor at point \mathbf{x} , caused by a ring source in R_E at point \mathbf{x}' and polarized along the i th axis. Since the scattered displacements as well as the Green's displacements satisfy the radiation condition, the integral over S_∞ in equation (4.6) vanishes. On the surface S_{bd} , the stresses due to the scattered waves vanish. The Green's functions are constructed in such a way that they satisfy the same boundary conditions as the scattered field on the free surface. Thus the stresses due to the Green's field also vanish on the surface S_{bd} . This means that the integral over the surface S_{bd} in equation (4.6) vanishes. There remains

$$-U_i^s = \int_{S_C} (U_j^s \Sigma_{ijk} - G_{ij} \sigma_{jk}^s) n_k dS. \quad (4.7)$$

Note in equation (4.7) that the integration is to be carried out only on the surface S_C . That is to say, in the terminology of Green's functions, the observation points are located on the surface S_C . The Green's sources are inside R_E , but their location is arbitrary at the moment. The differential surface element on the surface S_C may be written as

$$dS = r d\phi dl$$

where dl represents a line element on the contour C . The circumferential dependence of the displacements and stresses in equation (4.7) may be integrated explicitly to become

$$-\bar{U}_i^s = \delta_m \int_C (\bar{U}_j^s \bar{\Sigma}_{ijk} - \bar{G}_{ij} \bar{\sigma}_{jk}^s) n_k r dl \quad (4.8)$$

where

$$\delta_m = \begin{cases} 2\pi & , \quad m = 0 \\ \pi & , \quad m \geq 1 \end{cases}.$$

We now apply equation (4.6) to the region bounded by the surfaces S_C and S_{ab} . The A field is now chosen to be the free field U_i^{ff} and the B field is again the Green's field. The

Green's sources are again located inside R_E . Since the free field is due to sources located very far from the scatterer, it is not singular in this region. Moreover, the stresses on the surface S_{ab} due to the free field as well as the Green's field vanish. Thus one obtains

$$0 = \delta_m \int_C (\bar{U}_j^{ff} \bar{\Sigma}_{ijk} - \bar{G}_{ij} \bar{\sigma}_{jk}^{ff})(-n_k) r dl \quad (4.9)$$

The negative sign for n_k is due to the chosen direction. Adding equations (4.8) and (4.9) yields

$$\bar{U}_i^s = \delta_m \int_C (\bar{G}_{ij} \bar{\sigma}_{jk} - \bar{\Sigma}_{ijk} \bar{U}_j) n_k r dl \quad (4.10)$$

where \bar{U}_j and $\bar{\sigma}_{jk}$ represent the total wave fields:

$$\bar{U}_j = \bar{U}_j^{ff} + \bar{U}_j^s \quad (4.11a)$$

$$\bar{\sigma}_{jk} = \bar{\sigma}_{jk}^{ff} + \bar{\sigma}_{jk}^s \quad (4.11b)$$

Let us now assume that the Green's sources are placed on the mesh boundary B. Substituting equation (4.10) into equation (4.11a), an expression for the total wave field is now obtained as

$$\bar{U}_i(B) = \delta_m \int_C (\bar{G}_{ij} \bar{\sigma}_{jk} - \bar{\Sigma}_{ijk} \bar{U}_j) n_k r dl + U_j^{ff}(B) \quad (4.12)$$

In the above the contour integral along C is calculated in a clockwise direction from b to e . Arguments are included to specify where the field values are calculated. The variables in the integrand are calculated on the contour C for Green sources located on the contour B. Evaluating equation (4.12) for Green sources located at each node on the boundary B, one obtains

$$\{\bar{q}_B\} = \delta_m \int_C \left\{ [G^g][n]\{\sigma\} - [\Gamma^g]\{U\} \right\} r dl + \{\bar{q}_B^{ff}\} \quad (4.13)$$

where $[G^g]$, $[n]$, $\{\sigma\}$, $[\Gamma^g]$ and $\{U\}$ contain, respectively, terms of \bar{G}_{ij} , n_k , $\bar{\sigma}_{ij}$, $\bar{\Sigma}_{ijk} n_k$ and \bar{U}_j and \bar{q}_B denotes boundary nodal values. Note that the terms $\{\sigma\}$ and $\{U\}$ appearing on the right hand side are still unknown. Let us now assume that the region between C and B is discretized as shown in figure 4.3. (In actual discretization, substantially large

numbers of nine node elements are used). The contour integral is now divided into integrals over the segments 1–2, 2–3 and 3–4. Using the standard finite element methodology, the displacements and stresses on each segment can be related to the nodal displacements of the element which contains the segment:

$$\{\sigma\} = [L_\sigma]\{\bar{q}\} \quad (4.14a)$$

$$\{U\} = [N]\{\bar{q}\}. \quad (4.14b)$$

In the above, $[N]$ contains shape functions and $[L_\sigma]$ contains shape functions, its derivatives and material constants. Substituting equation (4.14) into equation (4.13), we obtain

$$\{\bar{U}(B)\} = [A]\{\bar{q}\} + \{\bar{U}^{ff}(B)\}. \quad (4.15)$$

In the above equation,

$$[A] = \delta_m \left\{ \int_{C_{1-2}} [Q]rdl + \int_{C_{2-3}} [Q]rdl + \int_{C_{3-4}} [Q]rdl \right\} \quad (4.16a)$$

where

$$[Q] = [[G^g][n][L_\sigma] - [\Gamma^g][N]]. \quad (4.16b)$$

The integral may now be evaluated on each segment by using a Gauss quadrature. Let us now partition $\{\bar{q}\}$ into $\{\bar{q}_B\}$ corresponding to the displacement on the contour B and $\{\bar{q}_I\}$ corresponding to the displacement interior to B . Equation (4.15) then takes the form

$$\{\bar{q}_B\} = [A_I]\{\bar{q}_I\} + [A_B]\{\bar{q}_B\} + \{\bar{q}_B^{ff}\}. \quad (4.17)$$

We note here that, in obtaining this equation, the continuity of the displacements and stresses across the finite element mesh boundary B is implicitly satisfied since it is built into the Green's functions. Substituting equation (4.4) into equation (4.17), and rearranging it, we obtain

$$\{\bar{q}_B^{ff}\} = [[I] + [A_I][S_{IC}] - [A_B]]\{\bar{q}_B\}. \quad (4.18)$$

Equation (4.18) may be solved for the displacements of the boundary nodes. Then, equation (4.4) may be used to obtain the displacements of interior nodes. The displacements due to scattered field at any point in the region exterior to boundary B may be obtained by using equation (4.10) with the Green's sources placed at the point of interest. We note here that G_{ij} and Σ_{ijk} in the above formulation represent the half space Green's tensors. The formulation is equally valid for a full space problem when full space Green's functions are used.

4.5 Green's function for axisymmetric analysis

The boundary integral formulation relies heavily on the availability of appropriate Green functions. In this section, we derive the Green functions for a time harmonic ring source buried in an elastic half space. However, we find that it is more instructive to start with the derivation of full space Green functions. It will be seen that half space Green functions are comprised of full space Green functions and additional terms arising from the free surface of the half space. We use a method of potential combined with the Hankel transform in the derivation. The procedure is of sufficient generality to be useful in general elastodynamic problems involving axisymmetric geometry.

4.5.1 Green's function for full space

Consider an entire space region as shown in figure 4.4 where (x, y, z) is the Cartesian coordinate system and (r, ϕ, z) the cylindrical coordinate system. z -axis is vertical. An arbitrary load (source) is assumed to be distributed over a ring of radius r' which is located at a depth z' . The medium is assumed to be homogeneous, isotropic and linearly elastic. It is understood that the motion is time-harmonic and the term, $e^{i\omega t}$ (ω is circular frequency), is suppressed in all expressions.

For the purpose of derivation, it is convenient to view the entire space as being com-

posed of two regions of the same material (figure 4.4). The source, which is singular, is then treated as a stress discontinuity across the plane $z = z'$. The governing equation of motion of a time-harmonic system in the absence of body forces may be written as

$$\mu \nabla^2 \mathbf{U} + (\lambda + \mu) \nabla \nabla \cdot \mathbf{U} + \rho \omega^2 \mathbf{U} = 0. \quad (4.19)$$

It is easy to show that the Helmholtz decomposition of displacements written in the form

$$\mathbf{U} = \nabla \varphi + \nabla \times (\chi \vec{e}_z) + \nabla \times \nabla \times (\eta \vec{e}_z) \quad (4.20)$$

satisfies equation (4.19) provided that the potentials φ, χ and η are the solutions of the scalar wave equations

$$(\nabla^2 + k_p^2) \varphi = 0 \quad (4.21a)$$

$$(\nabla^2 + k_s^2) \chi = 0 \quad (4.21b)$$

$$(\nabla^2 + k_s^2) \eta = 0 \quad (4.21c)$$

where k_p and k_s are the pressure and shear wave numbers, respectively:

$$k_p = \omega \sqrt{\frac{\rho}{\lambda + 2\mu}} \quad k_s = \omega \sqrt{\frac{\rho}{\mu}}.$$

The functional dependence of the potentials on the coordinate ϕ may be expressed as a Fourier series

$$\varphi(r, \phi, z) = \sum \varphi_m(r, z) e^{im\phi} \quad (4.22a)$$

$$\chi(r, \phi, z) = \sum \chi_m(r, z) e^{im\phi} \quad (4.22b)$$

$$\eta(r, \phi, z) = \sum \eta_m(r, z) e^{im\phi} \quad (4.22c)$$

where the summation is over the integral values of m from $-\infty$ to ∞ . Substituting equations (4.22) into equations (4.21) and invoking the orthogonality condition of the eigenfunctions $e^{im\phi}$, one obtains

$$\frac{\partial^2 \varphi_m}{\partial r^2} + \frac{1}{r} \frac{\partial \varphi_m}{\partial r} + \left(k_d^2 - \frac{m^2}{r^2} \right) \varphi_m + \frac{\partial^2 \varphi_m}{\partial z^2} = 0 \quad (4.23a)$$

$$\frac{\partial^2 \chi_m}{\partial r^2} + \frac{1}{r} \frac{\partial \chi_m}{\partial r} + \left(k_s^2 - \frac{m^2}{r^2} \right) \chi_m + \frac{\partial^2 \chi_m}{\partial z^2} = 0 \quad (4.23b)$$

$$\frac{\partial^2 \eta_m}{\partial r^2} + \frac{1}{r} \frac{\partial \eta_m}{\partial r} + \left(k_s^2 - \frac{m^2}{r^2} \right) \eta_m + \frac{\partial^2 \eta_m}{\partial z^2} = 0 \quad (4.23c)$$

for $m = 0, \pm 1, \pm 2, \dots$

In view of the axisymmetric geometry of the problem, we introduce the m th order Hankel transform

$$\tilde{f}^m(\xi, z) = \int_0^\infty f(r, z) r J_m(\xi r) dr \quad (4.24a)$$

whose inversion formula is

$$f(r, z) = \int_0^\infty \tilde{f}^m(\xi, z) \xi J_m(\xi r) d\xi \quad (4.24b)$$

where $f(r, z)$ is a sufficiently smooth function, ξ the transformation parameter and J_m the Bessel function of the first kind and order m .

Upon applying the m th order Hankel transform to the equations of motion corresponding to the m th harmonic number, equation (4.23), one obtains a set of ordinary differential equations in z

$$\frac{d^2 \tilde{\varphi}_m^m}{dz^2} + (k_d^2 - \xi^2) \tilde{\varphi}_m^m = 0 \quad (4.25a)$$

$$\frac{d^2 \tilde{\chi}_m^m}{dz^2} + (k_s^2 - \xi^2) \tilde{\chi}_m^m = 0 \quad (4.25b)$$

$$\frac{d^2 \tilde{\eta}_m^m}{dz^2} + (k_s^2 - \xi^2) \tilde{\eta}_m^m = 0 \quad (4.25c)$$

whose solutions are found to be, for Region 1,

$$\tilde{\varphi}_m^m(\xi, z) = A_m^1(\xi) e^{\alpha z} \quad (4.26a)$$

$$\tilde{\chi}_m^m(\xi, z) = C_m^1(\xi) e^{\beta z} \quad (4.26b)$$

$$\tilde{\eta}_m^m(\xi, z) = E_m^1(\xi) e^{\beta z} \quad (4.26c)$$

and for Region 2,

$$\tilde{\varphi}_m^m(\xi, z) = B_m^2(\xi) e^{-\alpha z} \quad (4.27a)$$

$$\tilde{\chi}_m^m(\xi, z) = D_m^2(\xi) e^{-\beta z} \quad (4.27b)$$

$$\tilde{\eta}_m^m(\xi, z) = F_m^2(\xi) e^{-\beta z} \quad (4.27c)$$

where A_m^1, B_m^2 , etc., are constants of integration to be determined from the boundary conditions and

$$\alpha = \sqrt{\xi^2 - k_p^2}$$

$$\beta = \sqrt{\xi^2 - k_s^2}.$$

The radicals α and β are made single valued by specifying the branch cuts emanating from the branch points $\xi = k_p$ and $\xi = k_s$, respectively. The branches are chosen such that the real parts of α and β are nonnegative (figure 4.5). Under this choice of the branches, the $e^{-\alpha z}$ and $e^{-\beta z}$ terms in Region 1, the $e^{\alpha z}$ and $e^{\beta z}$ terms in Region 2 are not admissible and are thus omitted in equations (4.26) and (4.27). In view of equations (4.22), (4.24) and (4.26), a solution of the scalar wave equations (4.21) can now be written, for Region 1, as

$$\varphi^1(r, \phi, z) = \sum e^{im\phi} \int_0^\infty A_m^1 e^{\alpha z} \xi J_m(\xi r) d\xi \quad (4.28a)$$

$$\chi^1(r, \phi, z) = \sum e^{im\phi} \int_0^\infty C_m^1 e^{\beta z} \xi J_m(\xi r) d\xi \quad (4.28b)$$

$$\eta^1(r, \phi, z) = \sum e^{im\phi} \int_0^\infty E_m^1 e^{\beta z} \xi J_m(\xi r) d\xi \quad (4.28c)$$

and for Region 2, as

$$\varphi^2(r, \phi, z) = \sum e^{im\phi} \int_0^\infty B_m^2 e^{-\alpha z} \xi J_m(\xi r) d\xi \quad (4.29a)$$

$$\chi^2(r, \phi, z) = \sum e^{im\phi} \int_0^\infty D_m^2 e^{-\beta z} \xi J_m(\xi r) d\xi \quad (4.29b)$$

$$\eta^2(r, \phi, z) = \sum e^{im\phi} \int_0^\infty F_m^2 e^{-\beta z} \xi J_m(\xi r) d\xi \quad (4.29c)$$

The determination of the unknown constants now remains.

In cylindrical coordinates, the displacements are related to the potentials through

$$U_r = \frac{\partial \varphi}{\partial r} + \frac{\partial \chi}{r \partial \phi} + \frac{\partial^2 \eta}{\partial z \partial r} \quad (4.30a)$$

$$U_\phi = \frac{\partial \varphi}{r \partial \phi} - \frac{\partial \chi}{\partial r} + \frac{\partial^2 \eta}{r \partial z \partial \phi} \quad (4.30b)$$

$$U_z = \frac{\partial \varphi}{\partial z} - \frac{\partial}{r \partial r} \left(r \frac{\partial \eta}{\partial r} \right) - \frac{\partial^2 \eta}{r^2 \partial \phi^2} \quad (4.30c)$$

Upon substituting equations (4.28) into equations (4.30), it takes the form, for Region 1,

$$U_z^1 = \sum e^{im\phi} \int_0^\infty [\alpha A_m^1 e^{\alpha z} + \xi^2 E_m^1 e^{\beta z}] \xi J_m(\xi r) d\xi \quad (4.31a)$$

$$U_r^1 \mp iU_\phi^1 = \sum e^{im\phi} \int_0^\infty \pm \xi [A_m^1 e^{\alpha z} \pm iC_m^1 e^{\beta z} + \beta E_m^1 e^{\beta z}] \xi J_{m\mp 1}(\xi r) d\xi. \quad (4.31b)$$

The stresses may be obtained from the constitutive law of classical linear elasticity

$$\sigma_{ij} = \lambda \delta_{ij} U_{k,k} + 2\mu(U_{i,j} + U_{j,i}). \quad (4.32)$$

Substituting equations (4.31) into equations (4.32), the expressions for stresses required for the analysis, in Region 1, are found to be

$$\sigma_{zz}^1 = \sum e^{im\phi} \int_0^\infty [\mu(2\xi^2 - k_s^2) A_m^1 e^{\alpha z} + 2\mu\xi^2 \beta E_m^1 e^{-\beta z}] \xi J_m(\xi r) d\xi \quad (4.33a)$$

$$\sigma_{rz}^1 \mp i\sigma_{z\phi}^1 = \sum e^{im\phi} \int_0^\infty \pm \mu\xi [2\alpha A_m^1 e^{\alpha z} + (\beta^2 + \xi^2) E_m^1 e^{\beta z} \pm i\beta C_m^1 e^{\beta z}] \xi J_{m\mp 1}(\xi r) d\xi \quad (4.33b)$$

The expressions for the displacements and stresses for Region 2 may be found from those for Region 1 by replacing the coefficients A_m^1 , C_m^1 and E_m^1 by B_m^2 , D_m^2 and F_m^2 , and α and β by $-\alpha$ and $-\beta$, respectively. The continuity conditions may be written as

$$\sigma_{zz}^1(r, \phi, z') - \sigma_{zz}^2(r, \phi, z') = F_r \quad (4.34a)$$

$$\sigma_{z\phi}^1(r, \phi, z') - \sigma_{z\phi}^2(r, \phi, z') = F_\phi \quad (4.34b)$$

$$\sigma_{zz}^1(r, \phi, z') - \sigma_{zz}^2(r, \phi, z') = F_z \quad (4.34c)$$

$$U_r^1(r, \phi, z') - U_r^2(r, \phi, z') = 0 \quad (4.34d)$$

$$U_\phi^1(r, \phi, z') - U_\phi^2(r, \phi, z') = 0 \quad (4.34e)$$

$$U_z^1(r, \phi, z') - U_z^2(r, \phi, z') = 0 \quad (4.34f)$$

where F_r , F_ϕ and F_z denote the components of the intensity of the source-load. The loading may be expanded in Fourier harmonics to become

$$F_j(r, \phi, z) = \sum F_{jm}(r, z) e^{im\phi} \quad j = r, \phi, z \quad (4.35)$$

Figure 4.6 shows the distribution of ring loads for the harmonics $m = 0$ and $m = 1$. Before substituting expressions for displacements and stresses in equations (4.34), we rewrite the continuity conditions at $z = z'$ in the following form:

$$(\sigma_{zr}^1 - i\sigma_{z\phi}^1) - (\sigma_{zr}^2 - i\sigma_{z\phi}^2) = \sum e^{im\phi}(F_{rm} - iF_{\phi m}) \quad (4.36a)$$

$$(\sigma_{zr}^1 + i\sigma_{z\phi}^1) - (\sigma_{zr}^2 + i\sigma_{z\phi}^2) = \sum e^{im\phi}(F_{rm} + iF_{\phi m}) \quad (4.36b)$$

$$\sigma_{zz}^1 - \sigma_{zz}^2 = \sum e^{im\phi} F_{zm} \quad (4.36c)$$

$$(U_r^1 - iU_\phi^1) - (U_r^2 - iU_\phi^2) = 0 \quad (4.36d)$$

$$(U_r^1 + iU_\phi^1) - (U_r^2 + iU_\phi^2) = 0 \quad (4.36e)$$

$$U_z^1 - U_z^2 = 0, \quad (4.36f)$$

and note that, the terms on the right hand side of equations (4.36) readily admit the following integral forms:

$$F_{rm} - iF_{\phi m} = \int_0^\infty (\tilde{F}_{rm}^{m-1} - i\tilde{F}_{\phi m}^{m-1}) \xi J_{m-1}(\xi r) d\xi \quad (4.37a)$$

$$F_{rm} + iF_{\phi m} = \int_0^\infty (\tilde{F}_{rm}^{m+1} + i\tilde{F}_{\phi m}^{m+1}) \xi J_{m+1}(\xi r) d\xi \quad (4.37b)$$

$$F_{zm} = \int_0^\infty \tilde{F}_{zm}^m \xi J_m(\xi r) d\xi \quad (4.37c)$$

which greatly facilitate the imposition of the continuity conditions. Substitution of equations (4.31), (4.33) and (4.37) into equations (4.36) results in a set of linear simultaneous equations which may be solved explicitly for the six unknowns A_m^1, \dots, F_m^2 . Substitution of the coefficients into equations (4.31) and (4.33) gives the displacements and stresses required for the analysis. The expressions for the Green's displacements and stresses for the case $m = 0$ may be found in Appendix E.

4.5.2 Green's function for half space

The half space Green functions are derived following the steps presented in the previous section. All the expressions and equations remain valid with the exceptions as noted

below. The Region 1 is now finite ($0 < z \leq z'$) and therefore admits $e^{-\alpha z}$ and $e^{-\beta z}$ terms in equations (4.26) which become

$$\tilde{\varphi}_m^m(\xi, z) = A_m^1(\xi)e^{\alpha z} + B_m^1(\xi)e^{-\alpha z} \quad (4.38a)$$

$$\tilde{\chi}_m^m(\xi, z) = C_m^1(\xi)e^{\beta z} + D_m^1(\xi)e^{-\beta z} \quad (4.38b)$$

$$\tilde{\eta}_m^m(\xi, z) = E_m^1(\xi)e^{\beta z} + F_m^1(\xi)e^{-\beta z} \quad (4.38c)$$

The nine integration constants A_m^1, \dots, F_m^2 are determined by solving nine equations, six of which are the continuity conditions (equations 4.36a–f). The remaining three arise from the boundary conditions at the surface of the half space:

$$\sigma_{zr}^1(r, \phi, 0) = 0 \quad (4.39a)$$

$$\sigma_{z\phi}^1(r, \phi, 0) = 0 \quad (4.39b)$$

$$\sigma_{zz}^1(r, \phi, 0) = 0 \quad (4.39c)$$

which are written at $z = 0$ as:

$$\sigma_{zr}^1 - i\sigma_{z\phi}^1 = 0 \quad (4.40a)$$

$$\sigma_{zr}^1 + i\sigma_{z\phi}^1 = 0 \quad (4.40b)$$

$$\sigma_{zz}^1 = 0 \quad (4.40c)$$

Upon solving the nine constants, displacements and stresses are obtained from equation (4.31) and (4.33). Expressions for half space Green functions are given in Appendix E. For illustration, we present here the expression corresponding to $m = 0$ for vertical displacement due to a unit ring source in the radial direction.

Full space:

$$G_{13} = - \int_0^\infty -sgn(z - z') \frac{\xi}{2k_s^2} [e^{-\alpha|z-z'|} - e^{-\beta|z-z'|}] \frac{J_1(\xi r')}{2\pi\mu} \xi J_0(\xi r) d\xi \quad (4.41a)$$

Half space:

$$\begin{aligned}
G_{13} = & - \int_0^\infty \left\{ -\text{sgn}(z-z') \frac{\xi}{2k_s^2} [e^{-\alpha|z-z'|} - e^{-\beta|z-z'|}] \right. \\
& + \frac{\xi F^+(\xi)}{2k_s^2 F^-(\xi)} [e^{-\alpha(z+z')} + e^{-\beta(z+z')}] \\
& \left. - \frac{2\xi(2\xi^2 - k_s^2)}{k_s^2 F^-(\xi)} [\xi^2 e^{-(\beta z + \alpha z')} + \alpha\beta e^{-(\alpha z + \beta z')}] \right\} \frac{J_1(\xi r')}{2\pi\mu} \xi J_0(\xi r) d\xi \quad (4.41b)
\end{aligned}$$

It may now be noted from these expressions and those given in Appendix E, that the half space Green functions may be obtained by adding extra terms to the full space Green functions. The additional terms represent the reflection at the surface of the half space of waves emanating from the Green's source. Since these expressions are very cumbersome, we carried out two checks in order to eliminate possible blunders and errors in the derivation. The first check is the reciprocity relations. In this, the Green functions should satisfy

$$G_{11}(x', z'; x, z) = G_{11}(x, z; x', z') \quad (4.42a)$$

$$G_{33}(x', z'; x, z) = G_{33}(x, z; x', z') \quad (4.42b)$$

$$G_{13}(x', z'; x, z) = G_{31}(x, z; x', z') \quad (4.42c)$$

where the primed coordinates denote source points and the unprimed ones denote observation points. These relations are checked numerically by switching the locations of source and observation points. In the second check, the source and observation points are assumed to be located on the contours C and B respectively and the elastodynamic reciprocity theorem (equation 4.6) is applied to the region bounded by the surfaces S_B and S_{ac} . The A field is chosen to be the free field \bar{U}_i^{ff} and the B field is the Green's field. In this case, one obtains

$$\bar{U}_i^{ff}(C) = \delta_m \int_B (\bar{G}_{ij} \bar{\sigma}_{jk}^{ff} - \bar{\Sigma}_{ijk} \bar{U}_j^{ff})(-n_k) r dl \quad (4.43)$$

The right hand side is computed for sources located at various locations on C. It was observed that the left and right hand sides matched at least to three significant digits.

4.6 Evaluation of Green's functions

The calculation of the Green's function is computationally very expensive. There are two branch points, as mentioned previously, at k_p and k_s lying on the formal path of integration. Moreover, an examination of the expressions for the Green's functions reveals that they have simple poles at k_r which corresponds to the root of the Rayleigh wave function $F^-(\xi)$. To be consistent with the radiation conditions and the choice of branches, the path of integration should be deformed around the singularities as shown in figure 4.5.

The integrals, often referred to as wave-number integrals, are evaluated numerically since exact integration seems impossible. It is proposed to carry out the integration on the complex plane along the deformed contour as shown in figure 4.5. This is necessitated by the proximity of the singular points to the formal path of integration. Note that this introduces no error as the integrands have no singularities in the first quadrant of the complex plane. Note also that the integrands are highly oscillatory due to the presence of Bessel functions. This entails a great deal of computational effort. In two dimensional wave propagation problems, the wave number integrals are of the form $\int_0^\infty F(\xi) \cos(r\xi) d\xi$ where the integrand is a complex function with a rapidly oscillatory behaviour. Two widely used methods emerge in the literature as the dominating philosophies for integrating oscillatory functions (Davis and Rabinowich, 1983). In one, integration is performed between the zeros of the integrand. In the other, a quadratic curve is fitted to $F(\xi)$ in each subinterval and the integral is evaluated analytically. For the problem at hand, the integrals to be evaluated are of the form $\int_0^\infty F(\xi) J_n(r_1 \xi) J_m(r_2 \xi) d\xi$ and none of the methods cited above can be used. Xu and Mal (1985, 1987) proposed a scheme based on the modified Clenshaw-Curtis approach for evaluation of wave number integrals encountered in two dimensional problems. Extension of this method for the fully three dimensional case seems difficult. The present author designed an adaptive scheme with self-adjusting interval lengths. The algorithm is based on the Simpson's quadrature. The routine automatically halves the

current subinterval if a certain error criterion is not satisfied. The advantage of this algorithm is that all ordinates from the failed trials are reused. Numerical experiments with some known integrals indicated that the adaptive scheme is superior to the conventional quadrature schemes using fixed step length.

In order to test the adaptive routine, the following integrals

$$I_1 = \int_0^\infty \frac{e^{-\gamma y}}{\gamma} \cos \xi x d\xi = -\frac{\pi i}{2} H_0^{(2)}(\beta r) \quad (4.44a)$$

$$I_2 = \int_0^\infty \frac{e^{-\gamma z}}{\gamma} J_0(\xi r) d\xi = \frac{e^{-i\beta R}}{R} \quad (4.44b)$$

$$\tau = \sqrt{\xi^2 - \beta^2} \quad r = \sqrt{x^2 + y^2} \quad R = \sqrt{r^2 + z^2}$$

are evaluated and the results are shown in Table 4.1. The values of a_1 and b_1 in figure 4.5 do not seriously affect the accuracy. Common sense should prevail in selecting values for a_1 and b_1 . Too small value of a_1 would bring that part of the contour that is parallel to the real axis too close to the singularities. On the other hand, too large value of a_1 has the undesirable effect of making the total length of the contour large which, in turn, increases the number of integrand evaluations. The value of b_1 should be larger than k_r to avoid the singularities. Based on extensive numerical testing, we recommend the following values:

$$a_1 = 0.5k_s \rightarrow 1.5k_s$$

$$b_1 = 1.5k_r \rightarrow 3.0k_r$$

From a numerical view point, the upper limit of integration, ∞ , merely represent some large number which is assumed to be equal to 2000 in the program. The program is designed to terminate as soon as the integral has converged. For instance, termination occurred at $c_1=36$ for the above two integrals. This is due to the fast decay of the negative exponential terms in the integrand.

The adaptive routine greatly aided the evaluation of Green's functions. The convergence of the Green's function integrals (equation 4.41) is mainly governed by $\Delta z = |z - z'|$

which indicates the difference of the levels on which source and observation points are located. When Δz is small, the negative exponential functions are weak and the integrand decays very slowly. Consequently the routine does not terminate until after c_1 has reached a large value. Very often, this causes numerical precision problems (underflow and loss of significant digits) and round-off error dominates the final value of the integral. Therefore, in the computation of Green's functions, c_1 was allowed to reach a maximum value of 150, at which point the integrals are assumed to have converged. We wish to emphasize here that the integrals converge by themselves most of the times before c_1 reaches the value 150. Only when the source and observation points are located almost on the same level does the numerical problem arise. Despite this, the final results are seen to be very good as shown in the next section.

4.7 Validation of the model

In order to validate the hybrid model, we consider the scattering P waves by a spherical cavity in a *full-space*. The selection of the full-space problem was motivated by the lack of benchmark solutions for scattering of P and SV waves in a half-space. The incident P wave is propagating in the direction parallel to the z -axis. In this case, only one harmonic number, namely $m=0$, is required. A typical mesh is shown in figure 4.7 which contains $5N_B$ number of nodes where N_B is the number of boundary nodes. The accuracy of the results depends on the fineness of the mesh as well as the number of boundary nodes. The fineness of the mesh addresses the finite element representation of the near field while the number of boundary nodes refers to the boundary integral representation of the far field. In general, the fineness of the mesh is increased until no appreciable variation is observed in the response. The following material properties are used: $\mu = 1.0$, $\rho = 1.0$ and $\nu = 0.25$. The normalized frequency is defined as

$$\bar{\omega} = \frac{\omega a}{\pi C_p} = \frac{2a}{\Lambda_p}$$

where

$$C_p = \sqrt{\frac{\lambda + 2\mu}{\rho}}$$

in which a is the radius of the cavity, C_p is the pressure-wave velocity and Λ_p is the wavelength of the incident P wave. Numerical results obtained from the hybrid model are compared with the analytical solution in figures 4.8–4.10. It is observed that the results for both real and imaginary parts obtained by using the hybrid model are in excellent agreement with the analytical ones. This clearly establishes the accuracy of the evaluation of Green functions for full space. We here note that the additional terms in equation (4.41b) required to form the half space Green functions contain strong negative exponential functions and, therefore, decay faster than the terms in full space Green functions. In view of this, one may conclude that the numerical evaluation of half space Green functions is no more difficult than the evaluation of full space Green functions.

4.8 Scattering by a canyon in a half space

Next we consider a half space. Embedded in the half space is a canyon of hemispherical geometry which is excited by a vertically incident P wave. It is defined by its potential $\varphi^i = e^{ik_p z}$ which is reflected by the free surface of the half space as another P wave of potential $\varphi^r = -e^{-ik_p z}$. The incident and reflected parts combined together constitute the free field φ^{ff} :

$$\varphi^{ff} = \varphi^i + \varphi^r = 2ik_p \sin(k_p z)$$

which gives rise to displacements

$$U_r^{ff} = 0 \quad U_z^{ff} = 2ik_p \cos(k_p z).$$

The resulting motion is axisymmetric. Therefore, only the harmonic number $m = 0$ is required. Sanchez-Sesma (1983) and Eshraghi and Dravinski (1989c) have obtained solutions to this problem using a numerical procedure which consists of constructing the

scattered field from a linear combination of wave functions for full space. Since the wave functions do not satisfy the zero-traction boundary conditions on the surface of the half space, they were imposed on a part of the surface in a least-square sense. Mossessian and Dravinski (1989) have also presented a solution scheme based on an indirect boundary integral formulation on the surface of the canyon using the half space Green functions. Figures 4.11–4.12 illustrate the response of the canyon for various frequencies. The amplitudes of vertical and horizontal displacements on the surface are normalized with k_p . Note that in the absence of irregularity, the displacement would be vertical and with relative amplitude of two. The selection of the material properties and the normalization factor were guided by our desire to compare our results with those of Mossessian and Dravinski (1989). We used 31 nodes on the boundary. Trial calculations with 21 boundary nodes did not show appreciable difference. Note the excellent agreement between the two sets of results. The ability of the hybrid model to produce very good results for both the full and half space problems is thus demonstrated. For an obliquely incident wave, the present approach requires many circumferential harmonic numbers. Moreover, the case of incident Rayleigh waves could also be treated. Extension of the hybrid model in these directions is currently underway.

4.9 Concluding remarks

The validity of the hybrid method that combines the finite element method with the direct boundary integral equation formulation has been established. For a smooth canyon, the indirect boundary integral formulation is slightly more efficient than the hybrid method. This is because the number of Green function calculations is the same for both methods, but the hybrid method requires additional computations for the finite element model. We wish to point out, however, that the finite element computations increase the total CPU time by only three percent. In multiple scattering problems involving more than one canyon, or in problems involving alluvial valleys, the indirect formulation on the boundary of the

scatterer would require a much higher number of Green function evaluations than required in the hybrid method. Very often, the CPU time in a complex problem is reduced by a factor of at least two by going from the indirect boundary technique to the hybrid method. The only drawback of the hybrid method is that it requires large memory storage for high frequencies and for complex geometries. It is of interest to note here that the hybrid method could be extended to include layered and orthotropic materials. In addition, it would be very interesting and useful to extend this investigation to poroelastic medium, in view of the applicability to realistic earthquake response evaluation. However, this would have to be a topic for future study.

Appendix E : Green's Functions for Axisymmetric Analysis

The following are used below:

$$\begin{aligned}
 \mathcal{L}_n\{\} &= \int_0^\infty \{\} \xi J_n(\xi r) d\xi \\
 sgn(z - z') &= \begin{cases} 1 & , \quad z > z' \\ -1 & , \quad z < z' \end{cases} \\
 F^\pm(\xi) &= (2\xi^2 - k_s^2)^2 \pm 4\alpha\beta\xi^2 \\
 H &= \frac{J_1(\xi r')}{2\pi} \\
 V &= \frac{J_0(\xi r')}{2\pi}.
 \end{aligned}$$

1. Green's functions for full-space: case $m = 0$

$$G_{11} = \mathcal{L}_1 \left\{ \left(\frac{\xi^2}{2\alpha k_s^2} e^{-\alpha|z-z'|} - \frac{\beta}{2k_s^2} e^{-\beta|z-z'|} \right) \frac{H}{\mu} \right\} \quad (E.1)$$

$$G_{31} = \mathcal{L}_1 \left\{ \left(sgn(z - z') \frac{\xi}{2k_s^2} [-e^{-\alpha|z-z'|} + e^{-\beta|z-z'|}] \right) \frac{V}{\mu} \right\} \quad (E.2)$$

$$G_{13} = \mathcal{L}_0 \left\{ \left(sgn(z - z') \frac{\xi}{2k_s^2} [e^{-\alpha|z-z'|} - e^{-\beta|z-z'|}] \right) \frac{H}{\mu} \right\} \quad (E.3)$$

$$G_{33} = \mathcal{L}_0 \left\{ \left(-\frac{\alpha}{2k_s^2} e^{-\alpha|z-z'|} + \frac{\xi^2}{2\beta k_s^2} e^{-\beta|z-z'|} \right) \frac{V}{\mu} \right\} \quad (E.4)$$

$$\Sigma_{133} = \mathcal{L}_0 \left\{ \left(-\frac{(2\xi^2 - k_s^2)\xi}{2\alpha k_s^2} e^{-\alpha|z-z'|} + \frac{\beta\xi}{k_s^2} e^{-\beta|z-z'|} \right) H \right\} \quad (E.5)$$

$$\Sigma_{333} = \mathcal{L}_0 \left\{ \left(sgn(z - z') \left[\frac{(2\xi^2 - k_s^2)}{2k_s^2} e^{-\alpha|z-z'|} - \frac{\xi^2}{k_s^2} e^{-\beta|z-z'|} \right] \right) V \right\} \quad (E.6)$$

$$\Sigma_{131} = \mathcal{L}_1 \left\{ \left(sgn(z - z') \left[-\frac{\xi^2}{k_s^2} e^{-\alpha|z-z'|} + \frac{(2\xi^2 - k_s^2)}{2k_s^2} e^{-\beta|z-z'|} \right] \right) H \right\} \quad (E.7)$$

$$\Sigma_{331} = \mathcal{L}_1 \left\{ \left(\frac{\alpha\xi}{k_s^2} e^{-\alpha|z-z'|} - \frac{(2\xi^2 - k_s^2)\xi}{2\beta k_s^2} e^{-\beta|z-z'|} \right) V \right\} \quad (E.8)$$

$$\Sigma_{111} = \mathcal{L}_0 \left\{ \left(\frac{(\lambda k_p^2 + 2\mu\xi^2)\xi}{2\alpha k_s^2} e^{-\alpha|z-z'|} - \frac{\mu\xi\beta}{k_s^2} e^{-\beta|z-z'|} \right) \frac{H}{\mu} \right\} - \frac{2\mu}{r} G_{11} \quad (E.9)$$

$$\begin{aligned}
 \Sigma_{311} = \mathcal{L}_0 \left\{ \left(sgn(z - z') \left[-\frac{(\lambda k_p^2 + 2\mu\xi^2)}{2k_s^2} e^{-\alpha|z-z'|} + \frac{\mu\xi^2}{k_s^2} e^{-\beta|z-z'|} \right] \right) \frac{V}{\mu} \right\} \\
 - \frac{2\mu}{r} G_{31} \quad (E.10)
 \end{aligned}$$

2. Green's function for half-space: case $m = 0$

$$G_{11} = \mathcal{L}_1 \left\{ \left(\frac{\xi^2}{2\alpha k_s^2} e^{-\alpha|z-z'|} - \frac{\beta}{2k_s^2} e^{-\beta|z-z'|} \right. \right. \\ \left. \left. - \frac{F^+(\xi)}{2k_s^2 F^-(\xi)} \left[\frac{\xi^2}{\alpha} e^{-\alpha(z+z')} + \beta e^{-\beta(z+z')} \right] \right. \right. \\ \left. \left. + \frac{2\xi^2 \beta (2\xi^2 - k_s^2)}{k_s^2 F^-(\xi)} [e^{-(\beta z + \alpha z')} + e^{-(\alpha z + \beta z')}] \right) \frac{H}{\mu} \right\} \quad (E.11)$$

$$G_{31} = \mathcal{L}_1 \left\{ \left(sgn(z - z') \frac{\xi}{2k_s^2} [-e^{-\alpha|z-z'|} + e^{-\beta|z-z'|}] \right. \right. \\ \left. \left. - \frac{\xi F^+(\xi)}{2k_s^2 F^-(\xi)} [e^{-\alpha(z+z')} + e^{-\beta(z+z')}] \right. \right. \\ \left. \left. + \frac{2\xi(2\xi^2 - k_s^2)}{k_s^2 F^-(\xi)} [\alpha\beta e^{-(\beta z + \alpha z')} + \xi^2 e^{-(\alpha z + \beta z')}] \right) \frac{V}{\mu} \right\} \quad (E.12)$$

$$G_{13} = \mathcal{L}_0 \left\{ \left(sgn(z - z') \frac{\xi}{2k_s^2} [e^{-\alpha|z-z'|} - e^{-\beta|z-z'|}] \right. \right. \\ \left. \left. - \frac{\xi F^+(\xi)}{2k_s^2 F^-(\xi)} [e^{-\alpha(z+z')} + e^{-\beta(z+z')}] \right. \right. \\ \left. \left. + \frac{2\xi(2\xi^2 - k_s^2)}{k_s^2 F^-(\xi)} [\xi^2 e^{-(\beta z + \alpha z')} + \alpha\beta e^{-(\alpha z + \beta z')}] \right) \frac{H}{\mu} \right\} \quad (E.13)$$

$$G_{33} = \mathcal{L}_0 \left\{ \left(-\frac{\alpha}{2k_s^2} e^{-\alpha|z-z'|} + \frac{\xi^2}{2\beta k_s^2} e^{-\beta|z-z'|} \right. \right. \\ \left. \left. - \frac{F^+(\xi)}{2k_s^2 F^-(\xi)} [\alpha e^{-\alpha(z+z')} + \frac{\xi^2}{\beta} e^{-\beta(z+z')}] \right. \right. \\ \left. \left. + \frac{2\xi^2 \alpha (2\xi^2 - k_s^2)}{k_s^2 F^-(\xi)} [e^{-(\beta z + \alpha z')} + e^{-(\alpha z + \beta z')}] \right) \frac{V}{\mu} \right\} \quad (E.14)$$

$$\Sigma_{133} = \mathcal{L}_0 \left\{ \left(\frac{\xi}{2\alpha k_s^2} [-(2\xi^2 - k_s^2) e^{-\alpha|z-z'|} + 2\alpha\beta e^{-\beta|z-z'|}] \right. \right. \\ \left. \left. + \frac{\xi F^+(\xi)}{2\alpha k_s^2 F^-(\xi)} [(2\xi^2 - k_s^2) e^{-\alpha(z+z')} + 2\alpha\beta e^{-\beta(z+z')}] \right. \right. \\ \left. \left. - \frac{2\xi\beta(2\xi^2 - k_s^2)}{k_s^2 F^-(\xi)} [(2\xi^2 - k_s^2) e^{-(\alpha z + \beta z')} + 2\xi^2 e^{-(\beta z + \alpha z')}] \right) H \right\} \quad (E.15)$$

$$\Sigma_{333} = \mathcal{L}_0 \left\{ \left(sgn(z - z') \frac{1}{2k_s^2} [(2\xi^2 - k_s^2) e^{-\alpha|z-z'|} - 2\xi^2 e^{-\beta|z-z'|}] \right. \right. \\ \left. \left. + \frac{F^+(\xi)}{2k_s^2 F^-(\xi)} [(2\xi^2 - k_s^2) e^{-\alpha(z+z')} + 2\xi^2 e^{-\beta(z+z')}] \right. \right. \\ \left. \left. - \frac{2\xi^2(2\xi^2 - k_s^2)}{k_s^2 F^-(\xi)} [(2\xi^2 - k_s^2) e^{-(\alpha z + \beta z')} + 2\alpha\beta e^{-(\beta z + \alpha z')}] \right) V \right\} \quad (E.16)$$

$$\begin{aligned}\Sigma_{131} = \mathcal{L}_1 \left\{ \left(sgn(z - z') \frac{1}{2k_s^2} [-2\xi^2 e^{-\alpha|z-z'|} + (2\xi^2 - k_s^2) e^{-\beta|z-z'|}] \right. \right. \\ \left. \left. + \frac{F^+(\xi)}{2k_s^2 F^-(\xi)} [2\xi^2 e^{-\alpha(z+z')} + (2\xi^2 - k_s^2) e^{-\beta(z+z')}] \right. \right. \\ \left. \left. - \frac{2\xi^2(2\xi^2 - k_s^2)}{k_s^2 F^-(\xi)} [2\alpha\beta e^{-(\alpha z + \beta z')} + (2\xi^2 - k_s^2) e^{-(\beta z + \alpha z')}] \right) H \right\} \quad (E.17)\end{aligned}$$

$$\begin{aligned}\Sigma_{331} = \mathcal{L}_1 \left\{ \left(\frac{\xi}{2\beta k_s^2} [2\alpha\beta e^{-\alpha|z-z'|} - (2\xi^2 - k_s^2) e^{-\beta|z-z'|}] \right. \right. \\ \left. \left. + \frac{\xi F^+(\xi)}{2\beta k_s^2 F^-(\xi)} [2\alpha\beta e^{-\alpha(z+z')} + (2\xi^2 - k_s^2) e^{-\beta(z+z')}] \right. \right. \\ \left. \left. - \frac{2\alpha\xi(2\xi^2 - k_s^2)}{k_s^2 F^-(\xi)} [2\xi^2 e^{-(\alpha z + \beta z')} + (2\xi^2 - k_s^2) e^{-(\beta z + \alpha z')}] \right) V \right\} \quad (E.18)\end{aligned}$$

$$\begin{aligned}\Sigma_{111} = \mathcal{L}_0 \left\{ \left(\frac{\xi}{2\alpha k_s^2} [(\lambda k_p^2 + 2\mu\xi^2) e^{-\alpha|z-z'|} - 2\mu\alpha\beta e^{-\beta|z-z'|}] \right. \right. \\ \left. \left. - \frac{\xi F^+(\xi)}{2\alpha k_s^2 F^-(\xi)} [(\lambda k_p^2 + 2\mu\xi^2) e^{-\alpha(z+z')} + 2\mu\alpha\beta e^{-\beta(z+z')}] \right. \right. \\ \left. \left. + \frac{2\xi(2\xi^2 - k_s^2)\beta}{k_s^2 F^-(\xi)} [(\lambda k_p^2 + 2\mu\xi^2) e^{-(\alpha z + \beta z')} + 2\mu\xi^2 e^{-(\beta z + \alpha z')}] \right) \frac{H}{\mu} \right\} \\ - \frac{2\mu}{r} G_{11} \quad (E.19)\end{aligned}$$

$$\begin{aligned}\Sigma_{311} = \mathcal{L}_0 \left\{ \left(sgn(z - z') \frac{1}{2k_s^2} [-(\lambda k_p^2 + 2\mu\xi^2) e^{-\alpha|z-z'|} + 2\mu\xi^2 e^{-\beta|z-z'|}] \right. \right. \\ \left. \left. - \frac{F^+(\xi)}{2k_s^2 F^-(\xi)} [(\lambda k_p^2 + 2\mu\xi^2) e^{-\alpha(z+z')} + 2\mu\xi^2 e^{-\beta(z+z')}] \right. \right. \\ \left. \left. + \frac{2\xi^2(2\xi^2 - k_s^2)}{k_s^2 F^-(\xi)} [(\lambda k_p^2 + 2\mu\xi^2) e^{-(\alpha z + \beta z')} + 2\mu\alpha\beta e^{-(\beta z + \alpha z')}] \right) \frac{V}{\mu} \right\} \\ - \frac{2\mu}{r} G_{31} \quad (E.20)\end{aligned}$$

Table 4.1
Evaluation of infinite integrals appearing in equation (4.44)

$$x = 1.0 \quad y = 1.0 \quad z = 1.0 \quad \beta = 2.0$$

Integral	I_1		I_2	
	Re	Im	Re	Im
Exact	-0.6727523	0.3087370	-0.5475915	0.1829786
Calculated	-0.6727520	0.3087371	-0.5475915	0.1829786

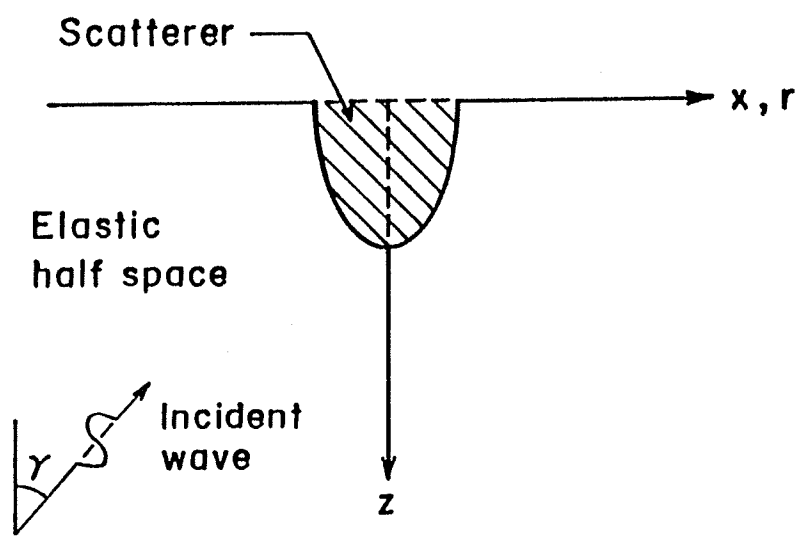


Figure 4.1 : Description of the problem

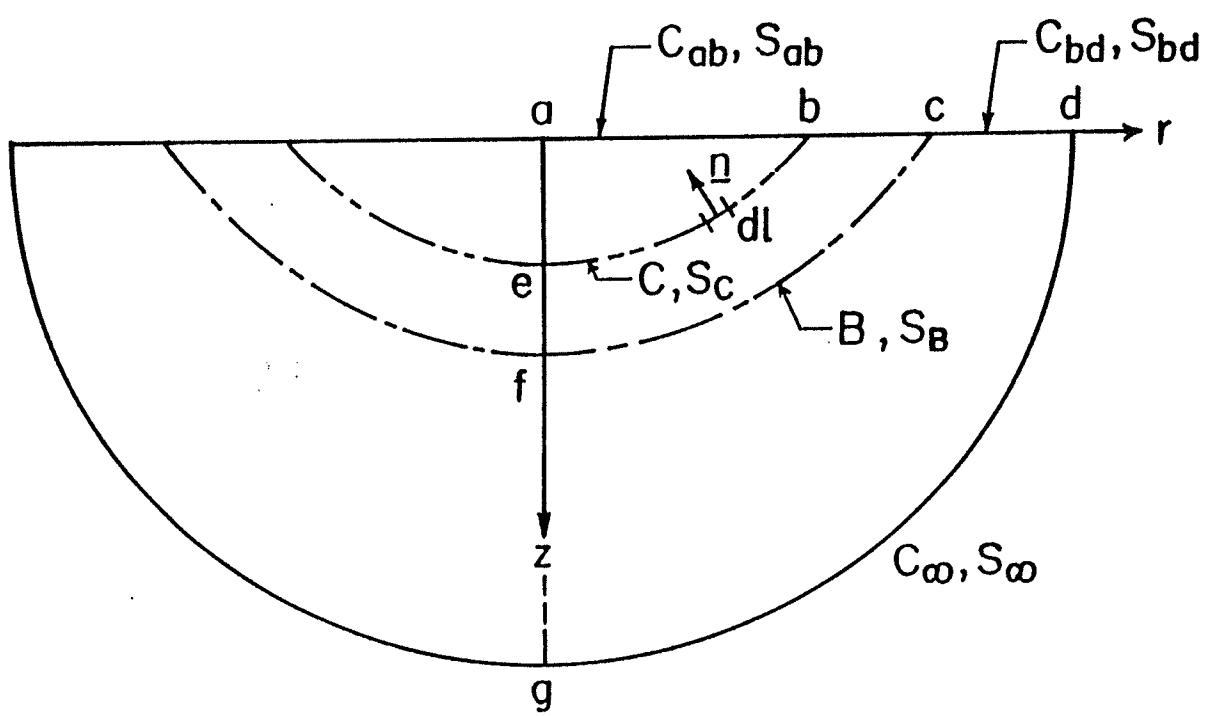


Figure 4.2 : Hybrid model

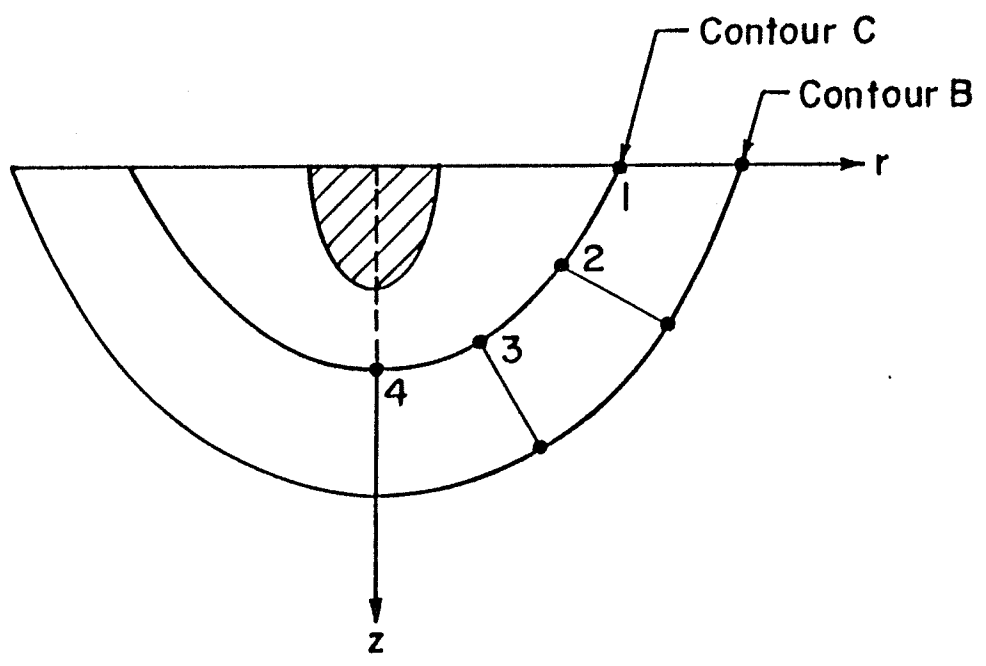


Figure 4.3 : Finite element mesh between contours C and B

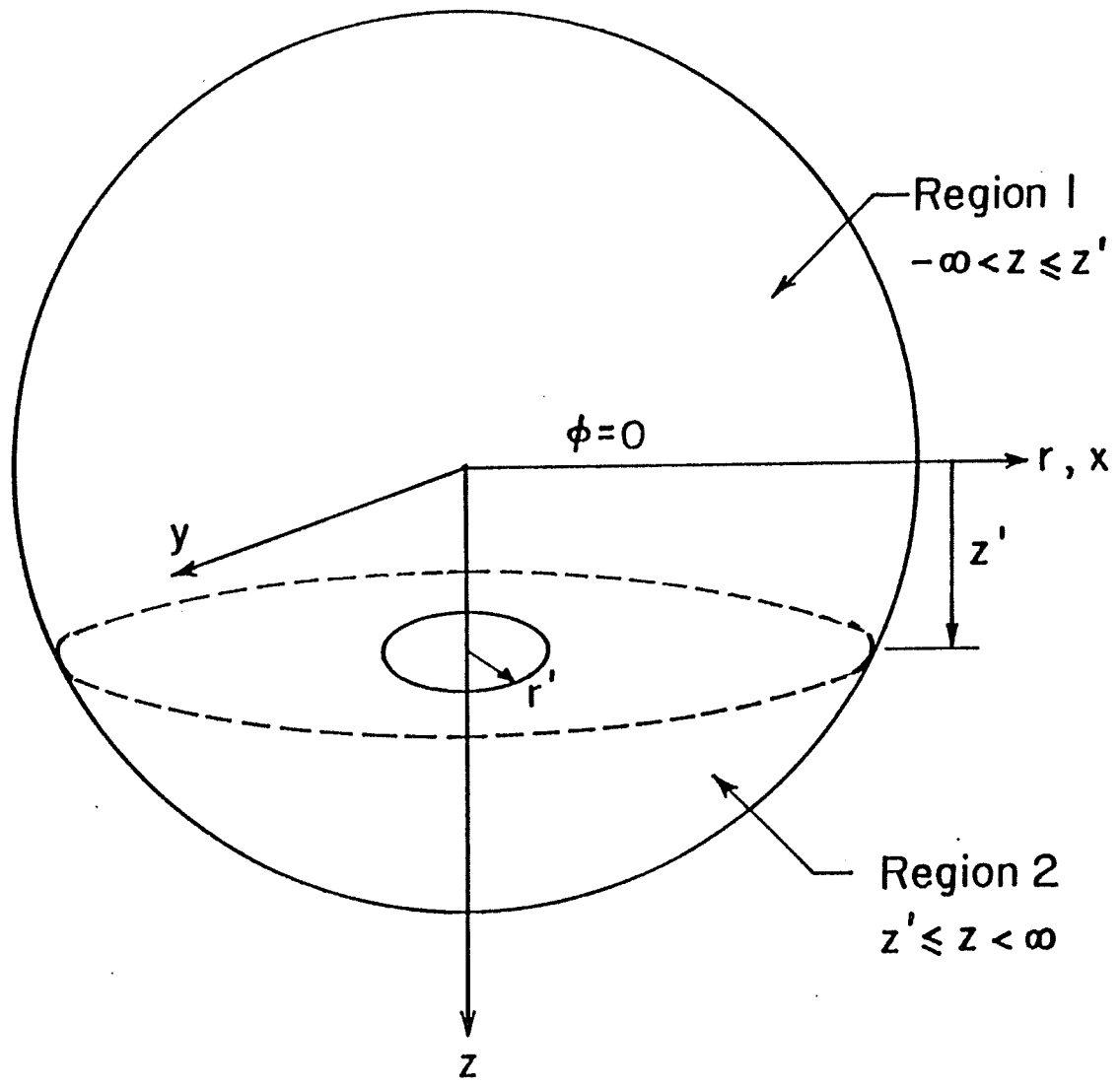


Figure 4.4 : System used in the derivation of full space Green functions

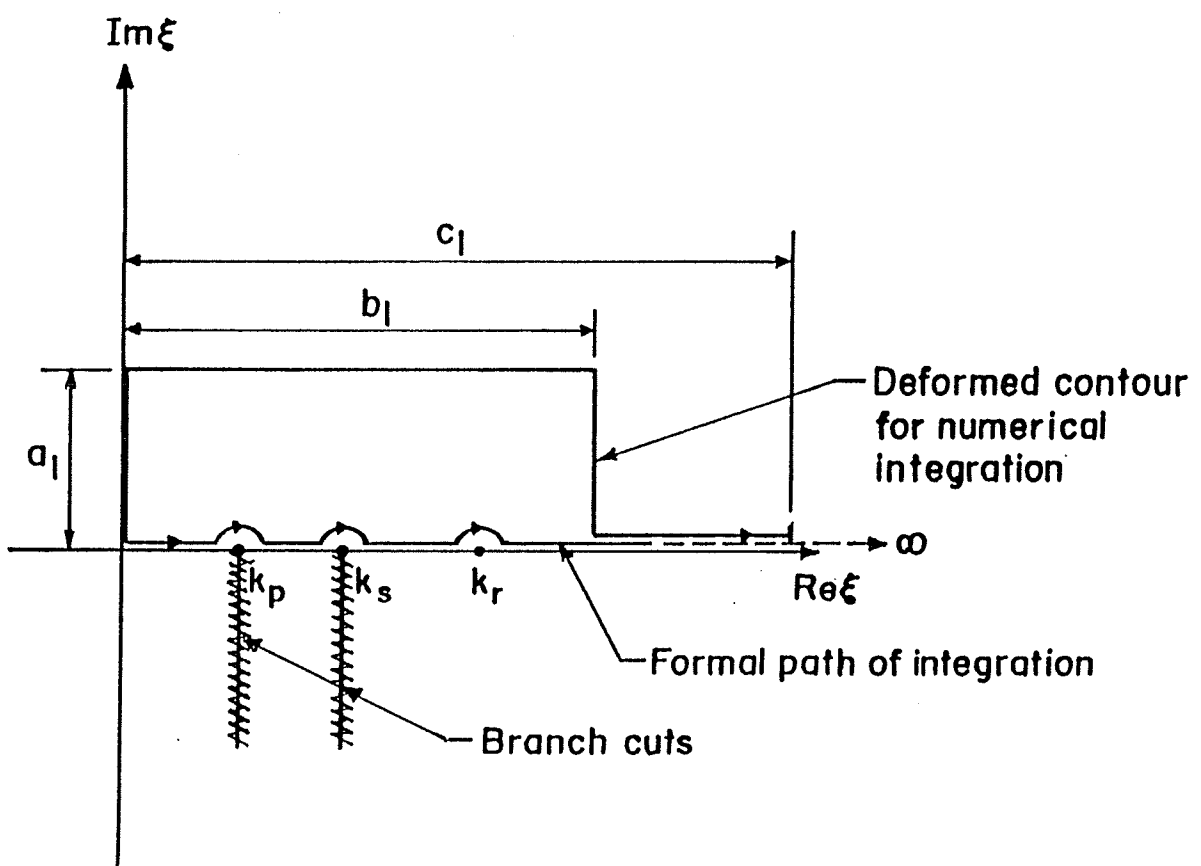
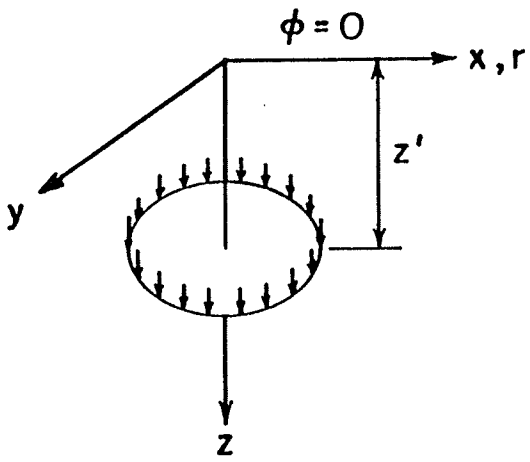
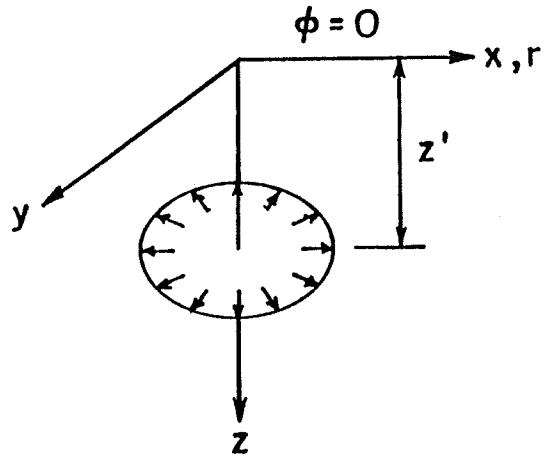


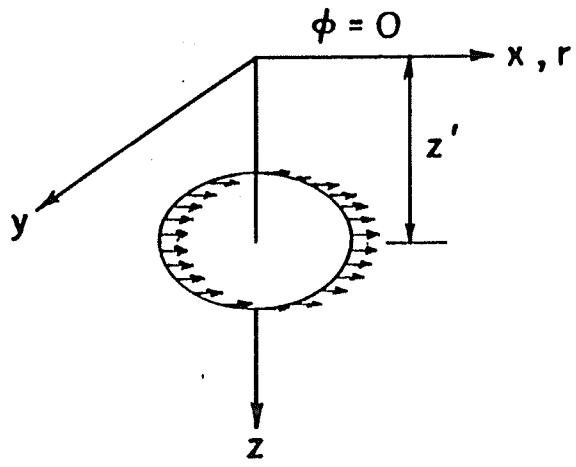
Figure 4.5 : Integration paths



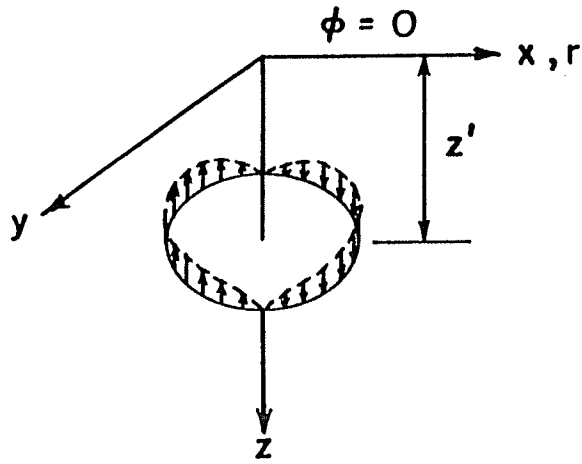
$$(a) \ m=0 \quad F_z = \frac{\delta(r-r')}{2\pi r}$$



$$(b) \ m=0 \quad F_r = \frac{\delta(r-r')}{2\pi r}$$



$$(c) \ m=1 \quad F_r = \frac{\delta(r-r')}{2\pi r} \cos \phi$$



$$(d) \ m=1 \quad F_z = \frac{\delta(r-r')}{2\pi r} \cos \phi$$

$$F_\phi = -\frac{\delta(r-r')}{2\pi r} \sin \phi$$

All rings diameter $2r'$

Figure 4.6 : Concentrated ring forces of unit magnitude

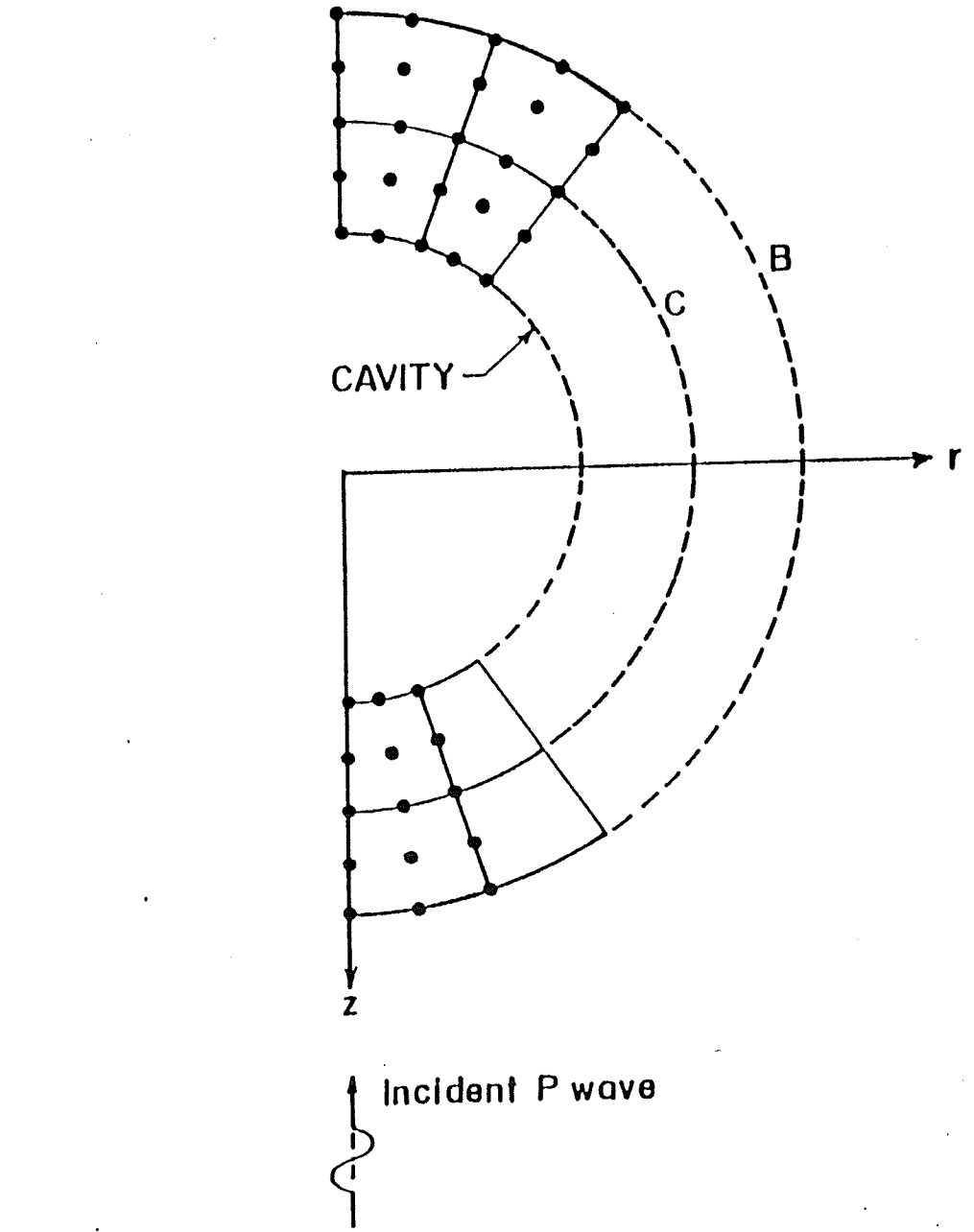


Figure 4.7 : Finite element mesh of Region R_I for a cavity in an entire space

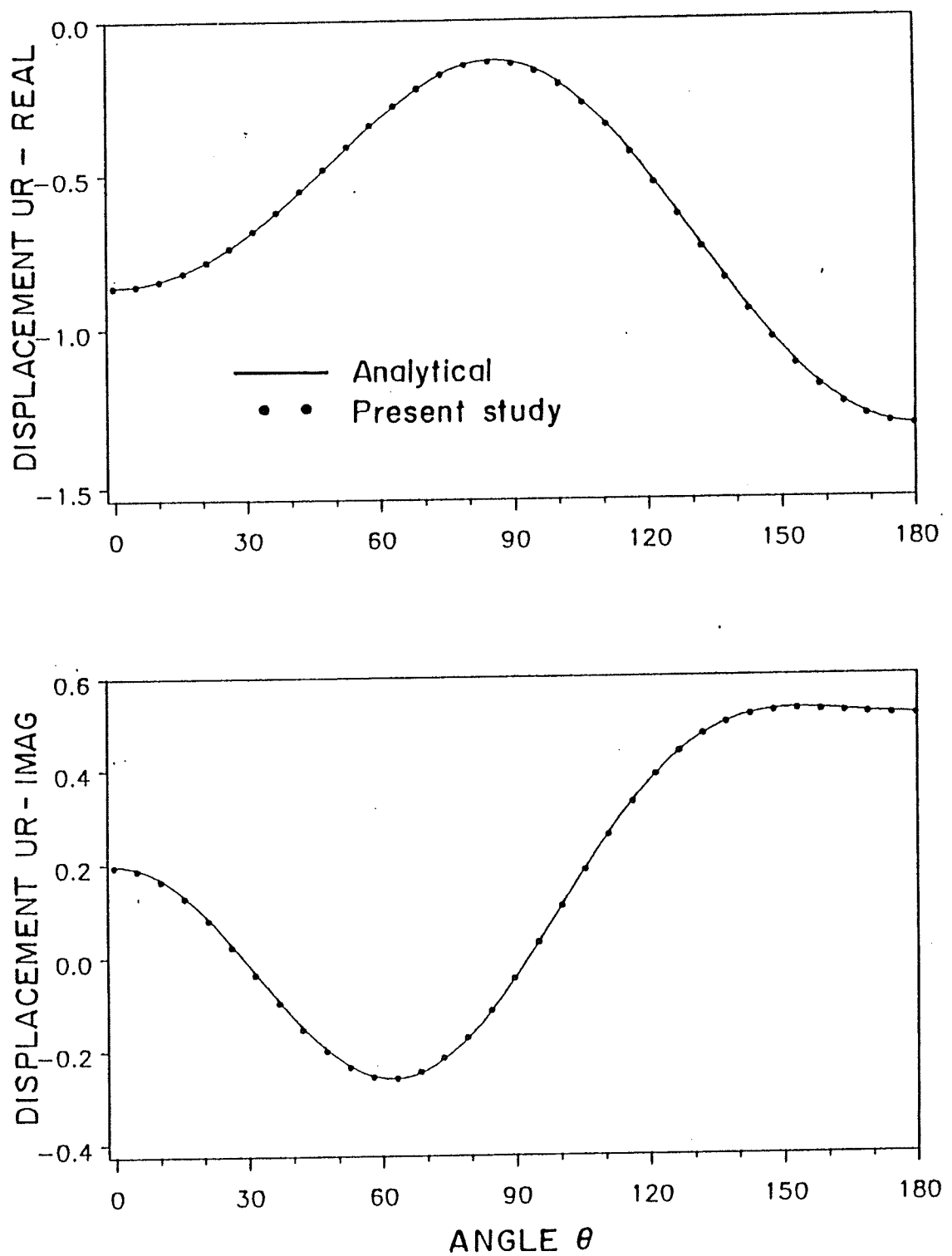


Figure 4.8 : Displacements on the surface of a spherical cavity
 $(\bar{\omega} = 0.25, N_B = 35)$

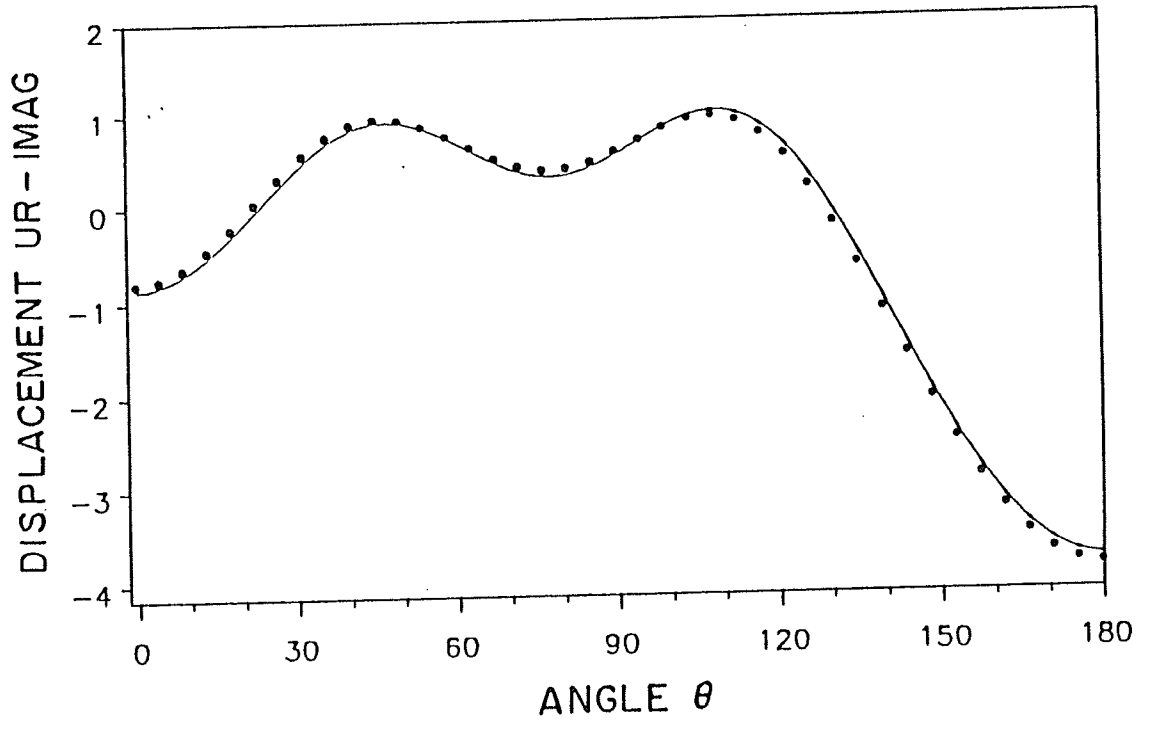
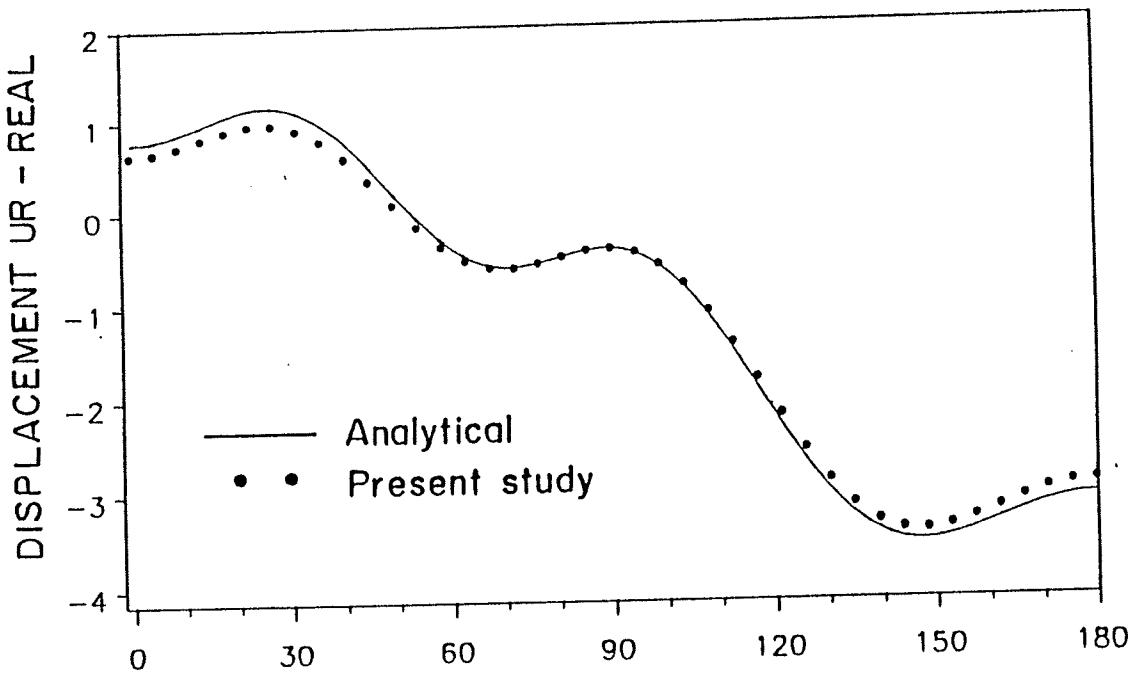


Figure 4.9 : Displacements on the surface of a spherical cavity
 $(\bar{\omega} = 0.75, N_B = 49)$

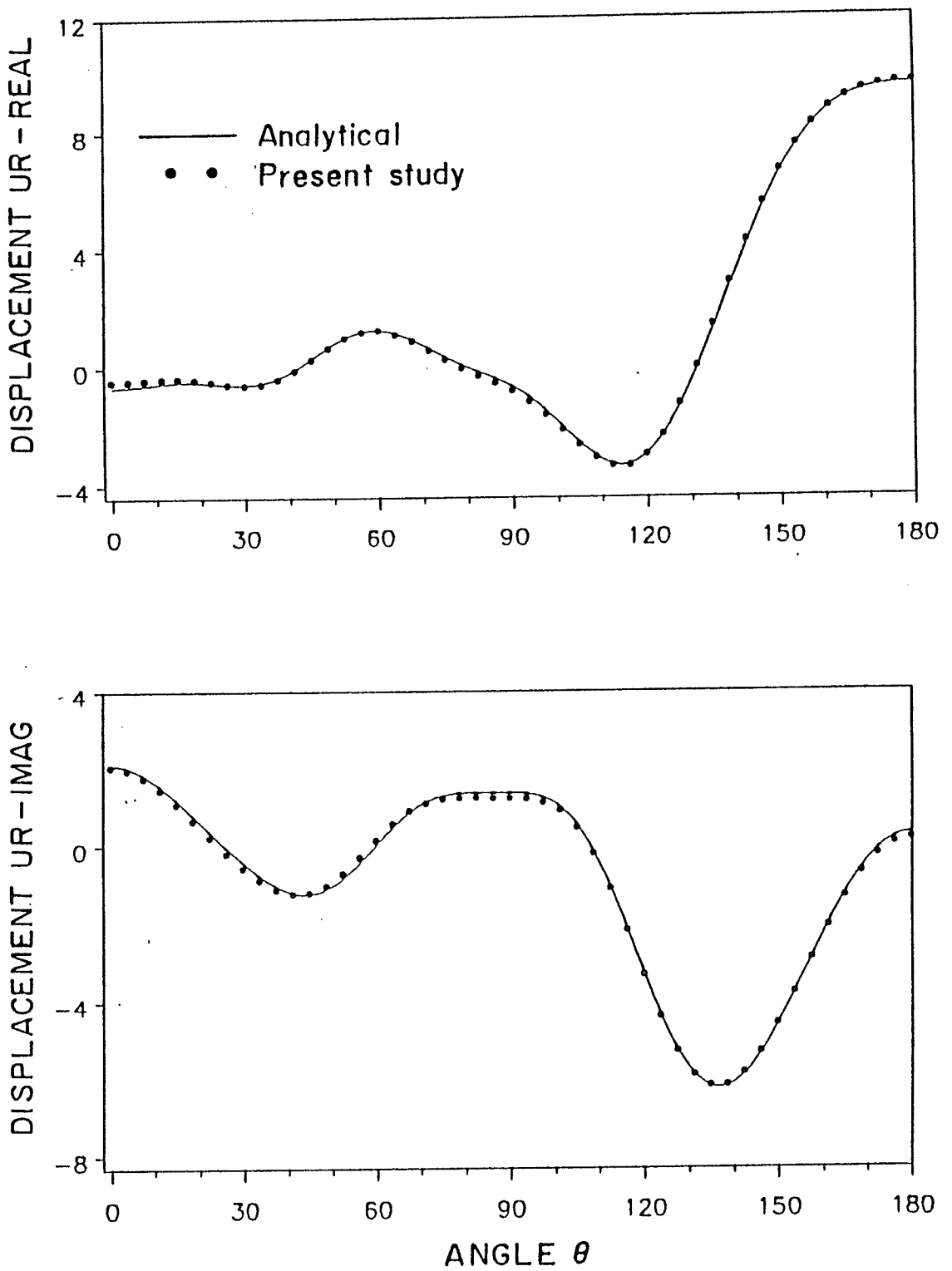


Figure 4.10 : Displacements on the surface of a spherical cavity
 $(\bar{\omega} = 1.50, N_B = 49)$

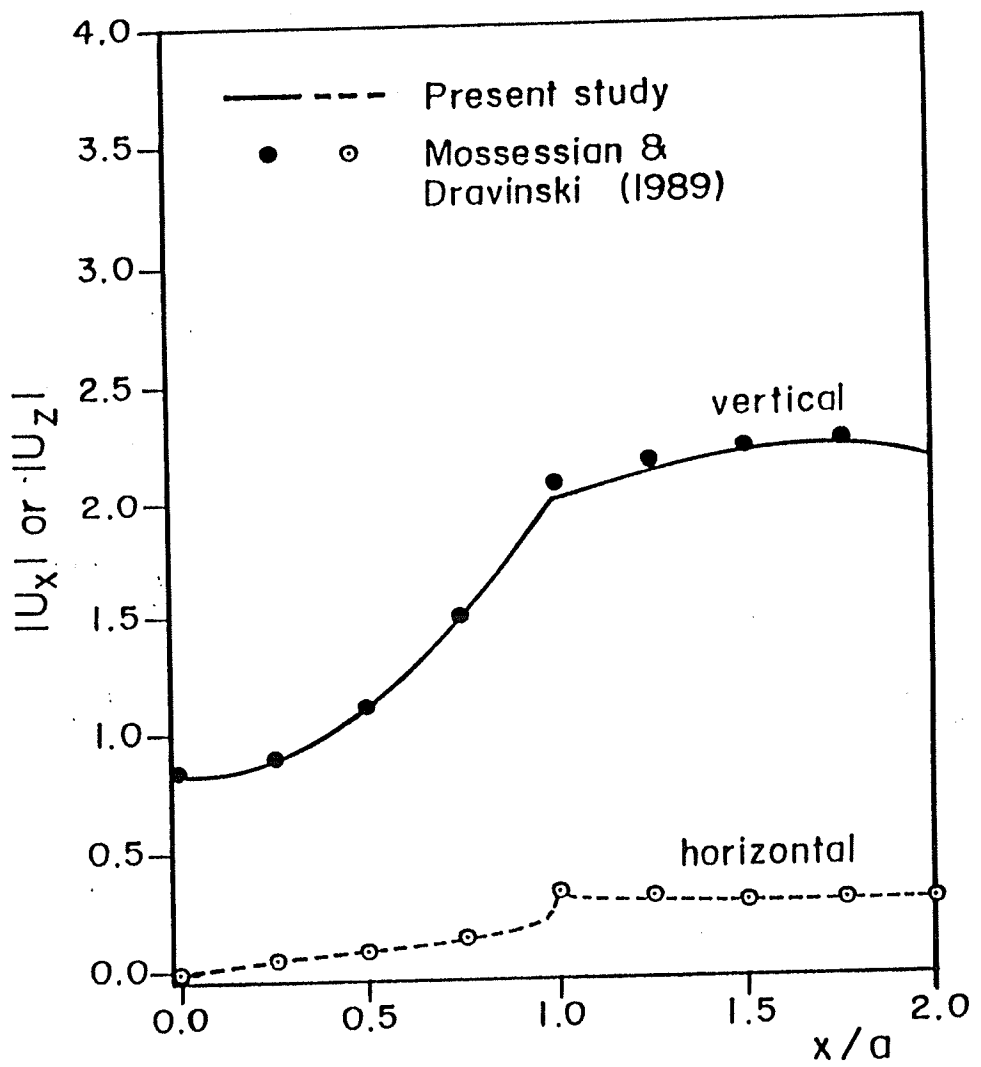


Figure 4.11 : Displacements on the surface of a hemispherical canyon
 $(\bar{\omega} = 0.25)$

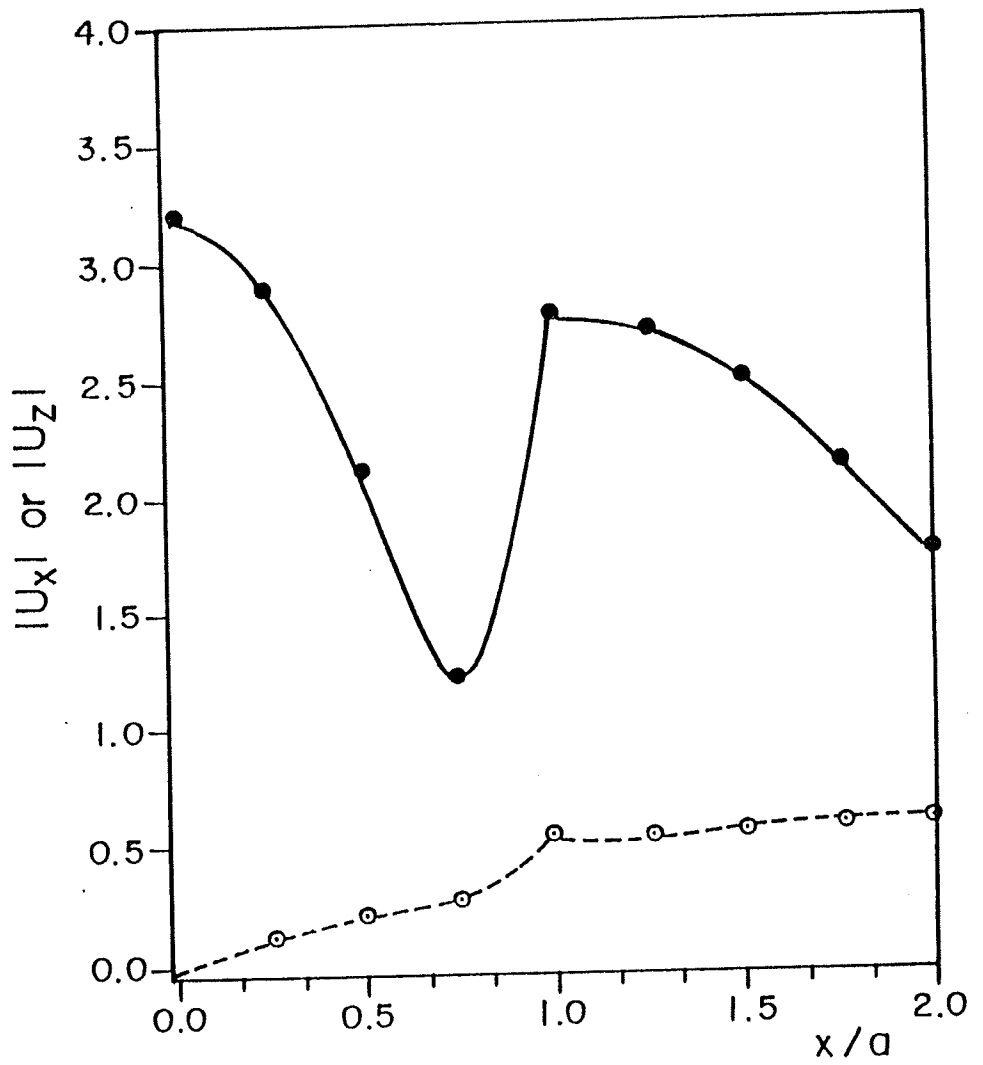


Figure 4.12 : Displacements on the surface of a hemispherical canyon
 $(\bar{\omega} = 0.50)$

5. SUMMARY AND CONCLUSIONS

Two hybrid modelling schemes have been presented to study a variety of elastic-wave scattering problems. In both schemes, a near field consisting of irregularities and a small region of the host medium is modelled by finite elements. Due to the great flexibility of finite elements, the near field region may contain inhomogeneous and nonisotropic materials. Arbitrary geometry of irregularities poses no difficulty. The far field region is modelled by wave functions in the first scheme. The resulting model is fairly simple, very economical and yields good results in low to moderate frequency range. For large frequencies, a very fine finite element model and a large number of wave functions are required.

In the second scheme, a boundary integral formulation is used to model the far field. The traction free boundary conditions on the surface of the half space are identically satisfied. The source and observation points are located on two different contours which precludes the singularities associated with the Green's functions. Accurate evaluation of Green's function is very tedious and expensive. This disadvantage is common to all formulations employing Green's functions. It must be emphasized, however, that the lack of efficient integration schemes is not to be seen as a limitation of the hybrid model itself. It only reflects the need for more research effort in this area. The advantage of the hybrid model is that the calculation of Green's functions is independent of the shape of a scatterer. This means that to analyse many different scattering geometries, the Green's functions have to be evaluated only once. This differs from the conventional boundary integral formulation on the boundary of the scatterer where Green's functions have to be calculated afresh everytime a new scatterer is encountered.

REFERENCES

- Abduljabbar, Z., Datta, S.K. and Shah, A. H. (1983): Diffraction of horizontally polarized shear waves by normal edge cracks in a plate, *J. Appl. Phys.*, 54, 461–472.
- Achenbach, J. D. (1973): *Wave Propagation in Elastic Solids*, North-Holland Publishing Company, Amsterdam.
- ASCE Civil Engineering, p. 46, March, 1990.
- Baron, M. L. and Matthews, A. T. (1961): Diffraction of a pressure wave by a cylindrical cavity in an elastic medium, *J. Appl. Mech.*, 28, 347–354.
- Barsoum, R. S. (1976): A degenerated solid element for linear fracture analysis of plate bending and general shells, *Int. J. Numer. Meth. Engng.*, 10, 551–564.
- Batoz, J. L., Bathe, K. J. and Ho, L. W. (1980): A study of three node triangular plate bending elements, *Int. J. Numer. Meth. Engng.*, 15, 1771–1812.
- Bazant, Z. P., Glazik, J. L. and Achenbach, J. D. (1976): Finite element analysis of wave diffraction by a crack, *J. Engng. Mech.*, 102, 479–496.
- Bouchon, M. (1973): Effect of topography on surface motion, *Bull. Seism. Soc. Amer.*, 63, 615–632.
- Boudin, M., Datta, S. K. and Shah, A. H. (1989): Dynamic amplification of alluvial valleys in layered medium, in *Engineering Seismology and Site Response*, edited by A. S. Cakmak and I. Herrera, 221–231, Computational Mechanics Publications, Southampton.
- Brebbia, C. A. (1978): *The Boundary Element Method for Engineers*, Pentech Press, London.
- Chow, Y. K. and Smith, I. M. (1981): Static and periodic infinite elements, *Int. J. Numer. Meth. Engng.*, 17, 503–526.
- Cole, D. M., Kosloff, D. D. and Minster, J. B. (1978): A numerical boundary integral equation method for elastodynamics, *Bull. Seism. Soc. Amer.*, 68, 1331–1357.
- Cruse, T. A. (1968): A direct formulation and numerical solution of the general transient elastodynamic problem II, *J. Math. Anal. Appl.*, 22, 341–355.
- Datta, S. K., Olsson, P. and Bostrom, A. (1988): Elastodynamic scattering from inclusions with thin interface layers, in *Wave Propagation in Structural Composites*, edited by A. K. Mal and T. C. T. Ting, 109–116, ASME, New York.
- Datta, S. K. and Shah, A. H. (1982): Scattering of SH waves by embedded cavities, *Wave Motion*, 4, 265–283.

- Datta, S. K., Shah, A. H. and Fortunko, C. M. (1982): Diffraction of medium and long wavelength SH-waves by edge cracks, *J. Appl. Phys.*, 53, 2895–2903.
- Davis, P. J. and Rabinowicz, P. (1983): *Method of Numerical Integration*, Academic Press, New York.
- Dhatt, G. (1969): Numerical analysis of thin shells by curved triangular elements based on discrete Kirchhoff hypothesis, Proc. Symp. on Application of finite element methods in Civil Engineering, 255–278, School of Engineering, Vanderbilt University, Nashville, TN.
- Dravinski, M. (1982): Scattering of SH waves by subsurface topography, *J. Engng. Mech.*, 108, 1-16.
- Dravinski, M. and Mossessian, T. K. (1987): Scattering of plane harmonic P, SV and Rayleigh waves by dipping layers of arbitrary shape, *Bull. Seism. Soc. Amer.*, 77, 212–235.
- ENR, Engineering News Record, February 22, 38–46, 1990.
- Eshraghi, H. and Dravinski, M. (1989a): Transient scattering of elastic waves by dipping layers of arbitrary shape. Part 1. Antiplane model, *Earthquake Engng. Struct. Dynam.*, 18, 397–415.
- Eshraghi, H. and Dravinski, M. (1989b): Transient scattering of elastic waves by dipping layers of arbitrary shape. Part 2. Plane strain model, *Earthquake Engng. Struct. Dynam.*, 18, 417–434.
- Eshraghi, H. and Dravinski, M. (1989c): Scattering of plane harmonic SH, SV, P and Rayleigh waves by non-axisymmetric three dimensional canyons: A wave function expansion approach, *Earthquake Engng. Struct. Dynam.*, 18, 983–998.
- Fawkes, A. F., Owen, D. R. J. and Luxmoore, A. R. (1979): An assessment of crack tip singularity models for use with isoparametric elements, *J. Engng. Frac. Mech.*, 11, 143–159.
- Hinton, E., Rock, T. and Zienkiewicz, O. C. (1976): A note on mass lumping and related processes in the finite element method, *Earthquake Engng. Struct. Dynam.*, 4, 245–249.
- Hrabok, M. M. and Hrudey, T. M. (1984): A review and catalogue of plate bending finite elements, *Comput. Struct.*, 19, 479–495.
- Hughes, T. J. R. (1987): *The Finite Element Method*, Prentice-Hall, New Jersey.
- Hughes, T. J. R., Taylor, R. L. and Kanoknukulchai, W. (1977): A simple and efficient finite element for plate bending, *Int. J. Numer. Meth. Engng.*, 11, 1529–1543.

- Hughes, T. J. R. and Cohen, M. (1978): The heterosis finite element for plate bending, *Comput. Struct.*, 9, 445–450.
- Kagami, H., Duke, C. M., Liang, G. C. and Ohta, Y. (1982): Observation of 1 to 5 second microtremors and their application to earthquake engineering. Part II. Evaluation of site effects upon seismic wave amplification due to extremely deep soil deposits, *Bull. Seism. Soc. Amer.*, 72, 987–998.
- Kagami, H., Okada, G., Shino, S., Oner, M., Dravinski, M. and Mal, A. K. (1986): Observation of 1 to 5 second microtremors and their application to earhtquake engineering. Part III. A two dimensional study of site effect in the San Franscisco valley, *Bull. Seism. Soc. Amer.*, 76, 1806–1812.
- Kausel, E., Roessel, J. M. and Waas, G. (1975): Dynamic analysis of footings on layered media, *J. Engng. Mech.*, 101, 679–693.
- Khair, K. R., Datta, S. K. and Shah, A. H. (1989): Amplification of obliquely incident seismic waves by cylindrical alluvial valleys of arbitrary cross-sectional shape. Part 1. Incident P and SV waves, *Bull. Seism. Soc. Amer.*, 79, 610–630.
- King, J.L. and Tucker, B. E. (1984): Observed variation of earthquake motion across a sediment filled valley, *Bull. Seism. Soc. Amer.* , 74, 137–151.
- Knopoff, L. (1959a): Scattering of compressional waves by spherical obstacles, *Geophysics*, 24, 30–39.
- Knopoff, L. (1959b): Scattering of shear waves by spherical obstacles, *Geophysics*, 24, 209–219.
- Lee, J. J. and Dasgupta, G. (1984): Interaction of nonlinear interiors with linear infinite domains, in *Numerical Methods for Transient and Coupled Problems*, edited by R. W. Lewis, E. Hinton, P. Bettess and B. A. Schrefler, 428–438, Pineridge Press, Swansea, U. K.
- Lee, V. W. (1984): Three dimensional diffraction of plane P, SV and SH waves by a hemispherical alluvial valley, *Soil Dynam. Earthquake Engng.*, 3, 133–144.
- Lynn, P. P. and Ingraffea, A. R. (1978): Transition elements to be used with quarter-point crack tip elements, *Int. J. Numer. Meth. Engng.*, 12, 1031–1036.
- Lysmer, L. and Kuhlemeyer, R. L. (1969): Finite dynamic model for infinite media, *J. Engng. Mech.*, 95, 859–877.
- McCoy, J. J. (1968): Effects of non-propagating plate waves on dynamical stress concentrations, *Int. J. Solids. Struc.*, 4, 355–370.
- Medina, F. and Taylor, R. L. (1983): Finite element techniques for problems of unbounded domains, *Int. J. Numer. Meth. Engng.*, 19, 1209–1226.

- Miklowitz, J. (1964): Scattering of a plane elastic compressional pulse by a cylindrical cavity, *Proc. Eleventh Int. Cong. Appl. Mech.*, Munich, 469–489.
- Miles, J. W. (1960): Motion of a rigid cylinder due to a plane elastic wave, *J. Acoust. Soc. Amer.*, Vol. 32, 1656–1659.
- Mindlin, R. D. (1951): Influence of rotatory inertia and shear on flexural motion of isotropic elastic plates, *J. Appl. Mech.*, 8, 31–38.
- Mosessian, T.K. and Dravinski, M. (1989): Scattering of elastic waves by three dimensional surface topographies, *Wave Motion*, 11, 579–592.
- Mow, C. C. (1965): Transient response of a rigid spherical inclusion in an elastic medium, *J. Appl. Mech.*, 32, 637–642.
- Mow, C. C. (1966): On the transient motion of a rigid spherical inclusion in an elastic medium and its inverse problem, *J. Appl. Mech.*, 33, 807–813.
- Norwood, F. R. and Miklowitz, J. (1967): Diffraction of transient elastic waves by a spherical cavity, *J. Appl. Mech.*, 34, 735–744.
- Pao, Y. H. and Chao, C. C. (1964): Diffraction of flexural waves by a cavity in an elastic plate, *AIAA Journal*, 2, 2004–2010.
- Pao, Y. H. and Mow, C. C. (1973): *Diffraction of Elastic Waves and Dynamic Stress Concentrations*, Crane and Russak, New York.
- Pugh, E. D. L., Hinton, E. and Zienkiewicz, O. C. (1978): A study of quadrilateral plate bending elements with reduced integration, *Int. J. Numer. Meth. Engng.*, 12, 1059–1079.
- Rajapakse, R. K. N. D. and Selvadurai, A. P. S. (1988): On the performance of Mindlin plate bending elements in modelling plate–elastic medium interaction: A comparative study, *Int. J. Numer. Meth. Engng.*, 23, 1229–1244.
- Sanchez-Sesma, F. J. and Rosenbluth, E. (1979): Ground motion at canyons of arbitrary shapes under incident SH waves, *Earthquake Engng. Struct. Dynam.*, 7, 441–450.
- Sanchez-Sesma, F. J. (1983): Diffraction of elastic waves by three dimensional surface irregularities, *Bull. Seism. Soc. Amer.*, 73, 1621–1636.
- Sezawa. K. (1927): Scattering of elastic waves and some allied problems, *Bull. Earthquake Res. Inst.*, Vol. 3, Tokyo Imperial University, p.19.
- Shah, A. H., Chin, Y. F. and Datta, S. K. (1987): Elastic wave scattering by surface breaking planar and non-planar cracks, *J. Appl. Mech.*, 54, 761–767.
- Shah, A. H., Wong, K. C. and Datta, S. K. (1982): Diffraction of plane SH-waves in a half space, *Earthquake Engng. Struc. Dynam.*, 10, 519–528.

- Shah, A. H., Wong, K. C. and Datta, S. K. (1983): Single and multiple scattering of elastic waves in two dimensions, *J. Acoust. Soc. Amer.*, 74, 1033–1044.
- Shah, A. H., Wong, K. C. and Datta, S. K. (1985): Surface displacements due to elastic wave scattering by buried planar and non-planar cracks, *Wave Motion*, 7, 319–333.
- Sih, G. C. and Loeber, J. F. (1968): Flexural wave scattering at a through crack in an elastic plate, *Engng. Fracture Mech.*, 1, 369–378.
- Sih, G. C. and Chen, E. P. (1977): Dynamic analysis of cracked plates in bending and extension, in *Mechanics of Fracture*, 3, G. C. Sih (editor), Noordhoff, Leyden.
- Smith, W. D. (1974): A non-reflecting plane boundary for wave propagation problems, *J. Comp. Phys.*, 15, 492–503.
- Thau, S. A. and Pao, Y. H. (1966): Diffractions of horizontal shear waves by a parabolic cylinder and dynamic stress concentrations, *J. Appl. Mech.*, 33, 785–792.
- Thau, S. A. and Pao, Y. H. (1967): Wave function expansions and perturbation method for diffraction of elastic waves by a parabolic cylinder, *J. Appl. Mech.*, 34, 915–920.
- Ting, L. and Miksis, M. J. (1986): Exact boundary conditions for scattering problems, *J. Acoust. Soc. Amer.*, 80, 1825–1827.
- Tong, P. (1970): New displacement hybrid finite element models for solid continua, *Int. J. Numer. Meth. Engng.*, 2, 73–83.
- Trifunac, M. D. (1971): Surface motion of semicylindrical alluvial valley for incident plane SH waves, *Bull. Seism. Soc. Amer.*, 61, 1755–1770.
- Tsao, S. J., Varadan, V. V. and Varadan, V. K. (1982): Comparison of matrix methods for elastic wave scattering problems, in *Review of Progress in Quantitative Non-destructive Evaluation*, 441–458, eds: D. O. Thompson and D. E. Chimenti, Plenum Press, New York.
- Varadan, V. V. and Varadan, V. K. (1979): Scattering matrix for elastic waves III. Applications to spheroids, *J. Acoust. Soc. Amer.*, 65, 896–905.
- Wijeyewickrema, A. C. and Keer, L. M. (1989): Transient elastic wave scattering by a rigid spherical inclusion, *J. Acoust. Soc. Amer.*, 86, 802–809.
- Wong, H. L. and Luco, J. E. (1976): Dynamic response of foundations of arbitrary shape, *Earthquake Engng. Struct. Dynam.*, 9, 579–587.
- Wong, H. L. and Trifunac, M. D. (1974): Scattering of plane SH waves by a semi-elliptical canyon, *Earthquake Engng. Struct. Dynam.*, 3, 157–169.
- Xu, P. C. and Mal, A. K. (1985): An adaptive integration scheme for irregularly oscillatory functions, *Wave Motion*, 7, 235–243.

- Xu, P. C. and Mal, A. K. (1987): Calculation of the inplane Green's functions for a layered viscoelastic solid, *Bull. Seism. Soc. Amer.*, 77, 1823–1837.
- Ying, C. F. and Truell, R. (1956): Scattering of a plane longitudinal wave by a spherical obstacle in an isotropically elastic solid, *J. Appl. Phys.*, 27, 1086–1097.
- Zienkiewicz, O. C. (1977): *Finite Element Method*, McGraw–Hill, London.